BSPM16050-080-3

ARA07C Cruise Report

2016 Korea-Russia-Germany East Siberian Sea Research Program

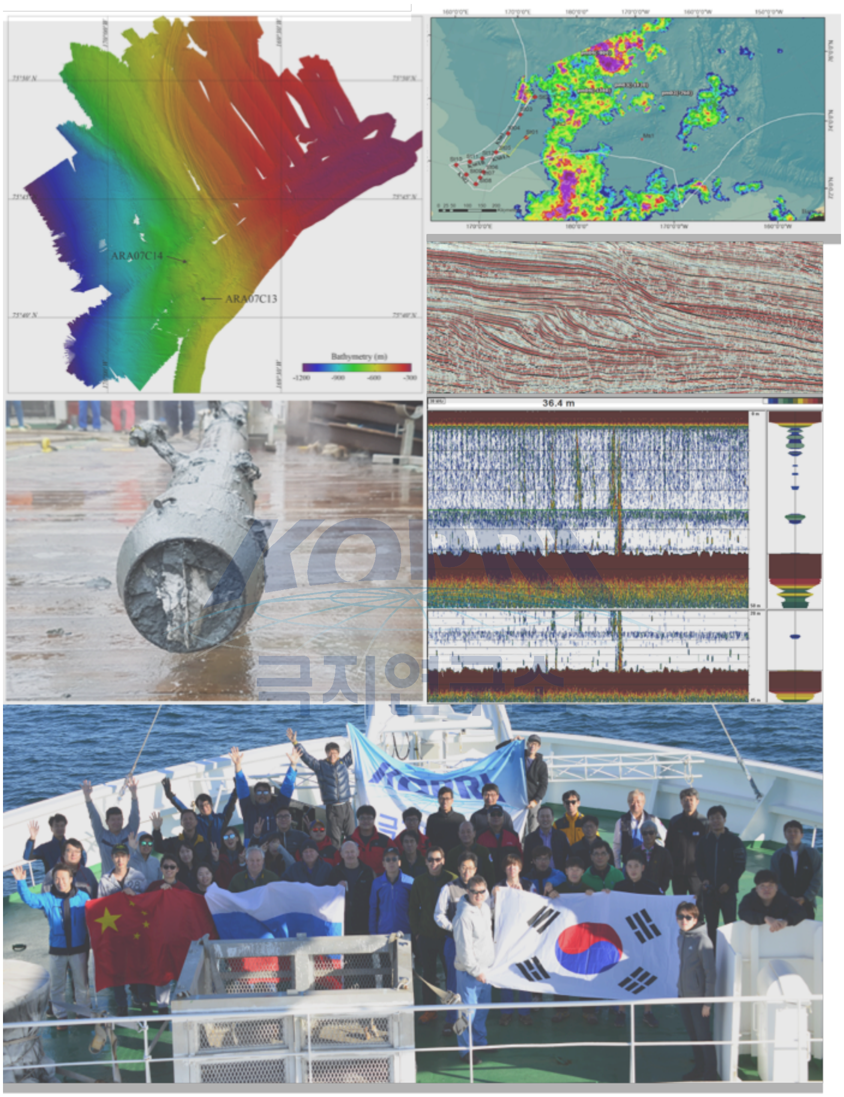

Barrow, USA-East Siberian Sea-Nome, USA
August 25 – September 10, 2016

Y.K. Jin and Onboard ship scientific party

KOPRI
Korea Polar Research Institute

ALFRED-WEGENER-INSTITUT
HELMHOLTZ-ZENTRUM FÜR POLAR-
UND MEERESFORSCHUNG

Contact Information

Young Keun Jin

Division of Polar Earth-System Sciences

Korea Polar Research Institute, KIOST

26 Songdomirae-ro, Yeonsu-gu, Incheon 21990, Korea

Tel : +82 32-760-5403

Email : ykjin@kopri.re.kr

Citation

Y.K. Jin and Onboard Ship Scientific Party, 2017. ARA07C Cruise Report: 2016 Korea-Russia-Germany East Siberian Sea Research Program, Korea Polar Research Institute

ARAO7C Cruise report

Contents

ARAO7C Cruise report

Summary

Y.K. Jin

2016 IBRV Araon Arctic Cruise Leg-2, Expedition ARA07C was a highly multidisciplinary undertaking carried out in the East Siberian Sea (ESS) on the IBRV Araon from August 25 to September 10, 2016 (Figure S1). The program was conducted as a collaboration between the Korea Polar Research Institute (KOPRI), P.P. Shirshov Institute of Oceanology (IORAS), and Alfred Wegener Institute (AWI). Multiple research experiments were carried out to investigate seafloor processes and methane release related to the degrading sub-sea permafrost, gas hydrate, and seismostratigraphy in the upper slope and shelf area of the ESS. In addition, physical and chemical oceanography measurements in the water column were undertaken with linked atmospheric studies from the vessel. The expedition focused on two main research areas: the upper slope and shelf areas in the ESS from August 27 to September 4 and the western slope of the Chukchi Plateau from September 6 to 8.

The multi-channel seismic data were acquired on the continental shelf and the upper slope of the ESS, totaling 3 lines with ~660 line-kilometers and ~13400 shot gathers from August 30 to September 12, 2016 (see Chapter 2 for more details). The multichannel seismic data will be processed post-expedition at KOPRI. The seismic data obtained in the 2016 Araon cruise will allow: 1) detailed velocity analyses to investigate the permafrost signature on the shelf area and identify zones of high-velocity sediments which would be indicative of the presence of ice along the seismic lines, 2) detailed deep geological structures and fluid expulsion features related to methane emission and gas hydrate in the shelf and slope area, and 3) detailed investigations of the seismostratigraphy of the upper several kilometers of sediments in the study area.

To better understand the shallow subsurface structure of the East Siberian shelf and slope, a high-resolution sparker seismic survey was carried out during the ARA07C cruise. 16 channel-digital streamer (Geometrics GeoEEL) was towed at a depth of about 1 meter. The sparker electrode source was operated with energy of 5,000 Joules.

A total of 190 L-km high resolution sparker seismic data was collected along three lines (Figure S.1). The main frequencies of sparker source ranged from 100 Hz to 1,000 Hz. Brute stack and single-trace gather were generated at the end of each line. Band pass filter of 30-60-600-650 Hz and AGC with a window length of 16 msec were applied to the outputs. More detailed processing procedures will be conducted in KIGAM.

Continuous sub-bottom profiler (SBP) and multibeam (MB) data were collected along all ship tracks for detailed imaging of bottom morphology and shallow subsurface sediment structures, as well as for verifying core-site location (see Chapter 4 for details). During this expedition, more than 4,100 line-kilometers of SBP data and 3,300 line-kilometers of MB data (with backscatter information) were recorded.

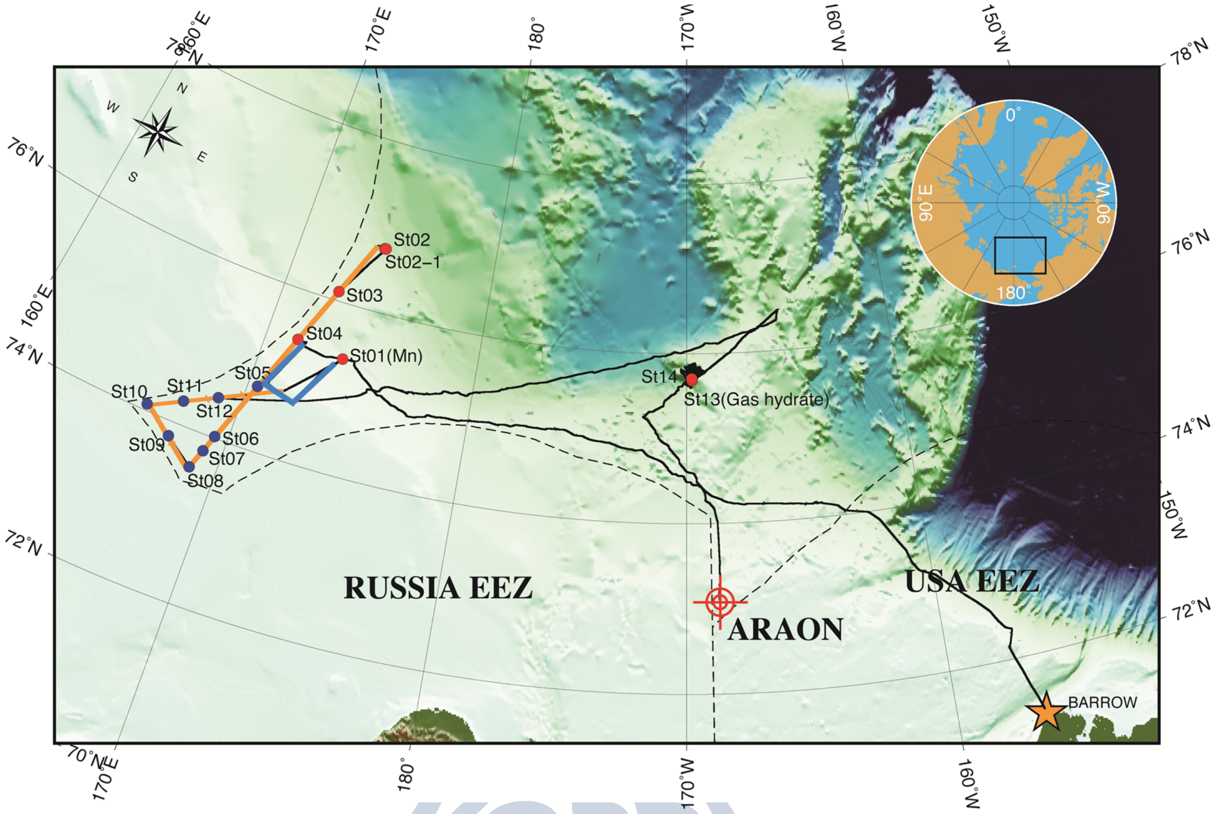

Figure S.1. Overview map of the ship track and stations of expedition ARA07C. The expedition was split into two main research areas in the East Siberian Sea: the middle/outer shelf and slope areas August 27 to September 4 and the western slope of the Chukchi Plateau from September 6 to 8, 2016. Ship track, SBP, and multibeam bathymetry (black line), multichannel seismic survey (orange line), and sampling stations (solid dot). Blue dots indicate stations where very high dissolved methane anomalies were measured in the water column.

These data are an essential part of the study of the sub-seafloor sediment dynamics in areas underlain by subsea permafrost, gas hydrate, fluid flow activities (gas seepage etc.) and at critical boundaries, especially at the shelf edge region. Newly collected MB and backscatter data offers us an opportunity to explore new plough marks of iceberg generated during past glacial periods.

Sediment sampling using gravity coring and box-coring was performed to find evidence of methane migration from sub-surface to the water column, gas hydrate occurrence, gas hydrate-related fluid flow and microbial activities in the ESS shelf and slope. In total, 7 gravity and 8 box cores were taken (Figure S.1) during the expedition. Among the cores, 2 gravity and 1 box corings were undertaken to sample gas hydrate at the mound structures on the upper slope of the western Chukchi Plateau. We first retrieved gas hydrate at about 3 m in sub-bottom depth in the East Siberian Sea. Most sediment analyses on the recovered cores will be performed post- expedition at various labs in KOPRI, and laboratories of other University-based collaborators in Korea. Onboard, sub-samples were taken from all gravity and box cores. On selected cores from the East Siberian study region, pore-waters were extracted using rhizones, after logging of physical properties and taking phots by IR-Trax onboard. Mineralogical and geochemical studies including isotopic analysis will be done as post-expedition work by research collaborators.

Highlights from sediment work in this expedition include the collection of manganese nodules at the shallow water of about 200 m on the upper continental slope and the first sampling of gas-hydrates on the topographic mound at about 500 m water depth on the western slope of the Chukchi Plateau. Considering that areas of low sedimentation rate as deep-sea abyssal plains are favorable for accumulation of nodules, it was very interesting that manganese nodules were found at such a shallow water depth. SBP shows seismic characteristics of gas chimney-like structure under the gas hydrate mound. Multi-channel seismic survey is highly requested to study the deeper structure of the mound and investigate migration paths and the origin of gas hydrate. Biomarker and microbial studies will also be conducted in Korea.

Heat flow measurements were conducted at 5 stations to study the geothermal condition of the East Siberian shelf and slope. During the expedition, we collected in-situ geothermal gradient, and thermal conductivity and shear stress of retrieved cores using brand new instruments to offer the benefit of time efficiency, when comparing with those used in the ARA04C and ARA05C expeditions (Jin et al, 2013, Jin and Scientific Party, 2015).

Water column studies were undertaken water sampling and Conductivity-Temperature-Depth (CTD) profiling at 13 stations to investigate the physical and chemical properties of seawater (Figure S1). These station-measurements were complemented by continuous water-properties and atmospheric measurements when the Araon was underway. Seawater samples will be analyzed for DIC/TA, nutrients, DOC, and POC post- expedition at KOPRI. Accurate measurements of the pH of seawater, and the underway continuous stream of measurements of seawater and atmospheric pCO_2, CH_4, and N_2O, required a variety of seawater/air physical properties to be considered in the calculation.

In order to understand how much and how fast methane emitted from the Arctic Ocean passes through the water column and goes out to the atmosphere, we conducted underway measurements of dissolved CH4 at the sea surface throughout the expedition period and seawater sampling to measure CH4 in the water column at 12 CTD sites. Atmospheric observations on IBRV Araon include basic meteorological parameters (e.g., air temperature, humidity, pressure and wind), radiative fluxes (e.g., net shortwave and longwave radiations), and greenhouse gases (e.g., carbon dioxide, methane and water vapor). During this expedition, radiosonde deployments were conducted twice a day (00:00 and 12:00 UTC) for observing the atmospheric vertical profile along the cruise track. Further details on the water column study and atmospheric observations are given in Chapter 7 and Chapter 8.

On-board test of Arctic safe voyage planning system under development at KRISO (Korea Research Institute of Ships and Ocean Engineering) was conducted during this cruise. The purpose of this test is to develop a safe Arctic voyage planning system. Specifically, the test will be used for the following goals: 1) development of a sea ice prediction system with accurate and high-resolution in Arctic sea, 2) development of a voyage planning technology in NSR for safe navigation, 3) construction of a co-work system between Arctic nations and international technology standardization through the establishment of safe navigation guidelines and leading action (see Chapter 8 for details).

Table S.1. Summary of data and samples taken in Expedition ARA07C

Survey/Sampling/Measurement	Amount
Sub-bottom profiler (SBP)	4148 L-km
Multi-beam bathymetry (MB)	3330 L-km
Multi-channel seismic (MCS)	665 L-km
Sparker seismic (SS)	181 L-km
CTD casting	13 sites
Heat flow measurement	5 sites
Box core	8 sites
Gravity core	7 sites

References

Jin, Y.K., Riedel M, and Ship scientific party of ARA04C, 2013, ARA04C Cruise Report, Korea Polar Research Institute, 171 pages.

Jin, Y.K., and Scientific Party, 2015, ARA05C Cruise Report: 2014 Korea-Canada-USA Beaufort Sea Research, Korea Polar Research Institute, BSPE15061-028-4, 121 pages.

Chapter 1. Background

F. Niessen, B. Baranov, and Y.K. Jin

1.1. Regional Geological Setting of the East Siberian Shelf and Continental Margin

1.1.1. Introduction

The East Siberian Sea (ESS) is one of the widest shelf seas in the world and it is believed to cover the largest area of sub-sea permafrost in the Arctic. Recently, it has become a focus of major environmental concern, because atmospheric venting of CH-4 from the East Siberian Shelf adds a significant proportion to methane release from the Arctic tundra. If related to thawing of sub-sea permafrost these methane fluxes can provide an important positive feedback to climate warming (Shakhova et al. 2016). Understanding the presence and stability of sub-sea permafrost and sedimentary gas requires knowledge of the geophysical and geological boundary conditions including the tectonic and sedimentological evolution of the shelf and continental slope, as well as the history of glaciations since permafrost does not form under ice sheets.

In contrast to their adjacent shelf areas, the Laptev and the Chukchi seas, the ESS is one of the least explored areas in the Arctic Ocean. In particular, this is true for the geology and glacial history of the outer shelf areas and the continental slopes linking to the Makarov Basin and the Mendeleev Ridge, including the Arlis Plateau, the Kutcherov Terrace and the Chukchi Abyssal Plain. One reason is that large areas of the shallow ESS are within the Exclusive Economic Zone (EEZ) of Russia, wherein research activity requires permission. Another reason is the sea-ice, which, despite reduction in summer coverage during the last decade, is still cumbering naval-based research in the area northwest and northeast of Wrangel Island and the New Siberian Archipelago, respectively, even during summer months.

1.1.2. The older tectonic and sedimentary history

One of the first geophysical/geological expeditions, which included seismic profiling and sediment coring at the East Siberian continental margin, was carried out by RV Polarstern in 2008 (Jokat 2009). The area under investigation also included two lines across the Chukchi continental margin and a section of the East Siberian Shelf up to 73° 30' N and around 170° E, which is outside the EEZ of Russia (between Wrangel Island and the New Siberian Archipelago). Hegewald and Jokat (2013a) used the results of multi-channel seismic (MCS) data, correlated with well-hole stratigraphy, to interpret the tectonic history and sedimentary evolution between the Mendeleev Ridge and the Chukchi region. It has been concluded that the Chukchi Abyssal Plane have already evolved in Jurassic to Early Cretaceous times contemporaneous with the opening of the Canada Basin. The Mendeleev Ridge formed in the Early Tertiary after the opening of the Amerasian Basin. A widely recognizable unconformity at the top of the Oligocene was interpreted as a result of the opening of the Fram Strait, which is associated with a lowering in water level and a change in the ventilation system of the Arctic

Ocean from the North Atlantic. Another distinct regional reflector marking the top of the Miocene was interpreted in relation with the opening of the Bering Strait and subsequent rising influence of water masses entering the Arctic Ocean from the Pacific. In a second paper on these seismic data (Jokat 2009), relative sea-level variations since the late Eocene were interpreted in the region (Hegewald and Jokat 2013b). The authors identified numerous progradational sequences in the upper 4 km of sediments, which indicates the cyclic northward growth of both the Chukchi and East-Siberian shelves during Cenosoic times with sea levels several times up to 300 m below and 100 m above modern times, respectively. In both publications by Hegewald and Jokat (2013), the area eastward of the Mendeleev Ridge (Chukchi region) is interpreted down to the acoustic basement, whereas the ESS and the adjacent continental margin strata older than the uppermost Oligocene remain have not been interpreted in seismic profiles. On the other hand, one of the MCS profiles (AWI-20080040) across the East Siberian outer shelf and continental slope clearly shows a stratigraphy of weakly ocean-ward dipping and prograding marine sediments of Miocene, Pliocene and Pleistocene age with no or only small and local tectonic overprint. These sediments are likely to be mostly of terrestrial origin transported to the Arctic Ocean by large Siberian Rivers (Stein 2009).

1.1.3. The glacial evolution

For the East Siberian continental margin, the seismic data obtained in 2008 by RV Polarstern including additional bathymetric data recorded by RV Araon in 2012 are also interpreted in terms of the glacial history of the area (Niessen et al. 2013). In MCS data, the uppermost sediments down to 400 m provide clear evidence of a sharp change in facies from progradational sequences, truncated in shallow water, to the deposition of glacial fans, wedges and moraines on the continental slope (Niessen et al. 2013). Although poorly resolved in MCP data, these glacial landforms are clearly visible in high-resolution sub-bottom profiles along the same track lines (Niessen et al. 2013). Together with bathymetric evidence for Mega-Scale-Glacial-Lineations, known as a key-indicator for fast-flowing grounded ice streams in the geological record (Spagnolo et al. 2014), these findings leave no doubt that the ESS had a typical glaciated continental margin during the youngest part of its history. The orientation of the lineations on a larger scale, the relatively deep water, in which they are found (1200 m), and indicators for ice-flow directions point to the presence of thick ice sheets othn the ESS in the past. This interpretation is consistent with conclusions drawn from glacial landforms found on the Chukchi Borderland, that the entire western Arctic Ocean area has undergone major glaciations with a complex flow pattern including sources of thick ice coming from the American continent, the Chukchi Borderland and the East Siberian Shelf (Dove et al. 2014, Jakobsson et al. 2014, Jakobsson et al. 2016). A major lack of information about the glacial history exists on the East Siberian Shelf. Here, the MCP data have insufficient resolution in the top 100 m, any sub-bottom data available is insufficient in penetration (mostly only 30 m) and the few cores available are very short (Jokat 2009, Stein et al. submitted 2016). In the MSC lines there is a hint for glacial erosion and till deposits near the sea floor (Hegewald and Jokat 2013b). So far it is not explored when exactly an ice sheet covered the ESS last and how far south this ice has extended.

1.1.4. The chronology of glacial events

The publication by Niessen et al. (2013) and Dove et al. (2014) did not offer an age model for the glaciations in the western Arctic. Meanwhile however, cores recovered on top of, or adjacent to, glacial landforms during several RV Araon expeditions between 2011 and 2015 were correlated to a core retrieved from the Chukchi Abyssal Plain in 2008, which has a well-constrained age model down to MIS 7 (Stein et al. 2010, Niessen et al. 2015a, Schreck et al. 2015). A comprehensive publication on the chronology of sediments along the East-Siberian and Chukchi continental margins is in preparation. The conclusions drawn from this work are that the youngest ice sheet was of small local size and grounded on the Chukchi Borderland during MIS 2, the Last Glacial Maximum (LGM). Any other glacial landforms identified further west on the East Siberian margin were formed earlier, during MIS 3 (upper continental slope), MIS 4 and intra MIS 5 (Kutcherov Terrace, Arlis Plateau, Mendeleev Ridge) with ice being thicker, and extended further into the Arctic Ocean, the older the glaciations are (Niessen et al. 2015a). No sediment core penetrated deep enough to constrain a glaciation in the area during MIS 6. There are relicts of older glaciations visible in seismic data, but they remain undated until longer cores become available directly adjacent to glacial landforms. The chronology above contradicts a recent interpretation by Jakobsson et al. (2016), which suggested that the last grounding of ice on the Arlis Plateau from an East Siberian ice sheet have occurred during MIS 6. One long core retrieved during the RV Araon expedition ARA06C in 2015 from the Chukchi Abyssal Plain give hints that major glaciations in the western Arctic have occurred during MIS 12 and possibly MIS 16 (Nam 20xx). According to sub-bottom acoustic data, the latter have possibly formed the onset of Quaternary glaciations in the area.

The youngest glacial overprint in the area is documented by a belt of iceberg ploughmarks ranging from present water depths of about 350 m to about 60 m. These landforms were first described and dated in a paper by Hill and Driscoll (2010) along the Chukchi margin at about 180° W, where they were covered by 6 to 8 m thick younger sediments between 60 and 100 m water depth. Radiocarbon dating of sediments directly overlying the plough marks revealed ages between about 12,500 and 13,800 cal. yrs. BP, indicating the event of iceberg-discharge occurred during the Younger Dryas. Based on mineralogy of the ice-rafted debris, the icebergs appear to be sourced from the northwestern Alaskan margin (Hill and Driscoll 2010). Similar plough marks were identified on the Chukchi Borderland at 168° W (Kang et al. 2012) in a depth range of 350 to 100 m. Sediment cores from 168° W confirm the age model suggested for plough marks at 180° W (Stein et al. under review). These plough marks extend west at least to 167° E on the slope of the ESS as indicated in echo-sounding data published in the Russian literature (Gusev et al. 2012). It is interesting to note that along all ship-track lines with hydro-acoustic data (RV Polarstern 2008, RV Araon 2011 to 2015) icebergs have ploughed older sediments strongly thereby destroying any previous stratification and also masking deeper acoustic penetration of sub-bottom profiler. If the published age model applies to all of these plough marks, this suggests that armadas of icebergs drifted along the Chukchi and East Siberian continental slope during, or at the end of, the Younger Dryas. In conclusion, several Pleistocene glaciations with kilometer-thick ice sheets must have occurred on the shelf area of the ESS. In general, the former shelf-based ice sheets in the western Arctic were larger during the middle Pleistocene and then became successively smaller during the younger glacial times with the smallest coverage during the LGM apparently not covering the East Siberian shelf. The youngest intensive grounding event of icebergs possibly occurred during termination of MIS 2 along the edge of the East Siberian continental shelf and did not derive from the collapse of a local ice sheet. For the area under investigation (ESS), however, this was not fully explored for both the timing of the event and the source of icebergs.

1.1.5. The puzzle of subsea permafrost

According to the present knowledge of the glacial history of the western Arctic Ocean, it is likely that during the LGM with a sea level approximately 120 m below present (Stanford et al. 2011), the entire shelf area of the ESS was exposed to very cold air temperatures so that thick permafrost should have formed. Indeed, in water depths shallower than 80 m, sub-bottom profiles in the ESS (Jokat 2009) recorded from the shelf edge to a latitude of 74°30' N in 60 m water depth exhibited acoustic facies, suggesting that at least relicts of submarine permafrost are present. Discontinuous acoustically transparent zones (? permafrost) mask sub-bottom strata beneath an unfrozen 10m thick top sediment layer (Niessen et al. 2015b) often associated with structures indicative of upward migrating gas. In certain places, unfrozen sediment-filled depressions (? taliks) were visible to about 20 m below the seafloor, which may be related to former thermokarst and/or channels filled with unfrozen deposits. These facies were somewhat similar to what has been published in high-resolution sub-bottom profiles from the Laptev-Sea (Recant et al. 2015). There, a basal reflector marks the top of an acoustically transparent unit interpreted as frozen sediments. These transparent unit cuts through stratified unfrozen sediments discontinuously, clearly indicating it is of post-depositional origin. A similar pattern is observed in sub-bottom profiles of the ESS. However, clear diagnostic acoustic features like "permafrost overhangs" observed in the Laptev Sea (Rekant et al. 2015) were not visible in profiles from the ESS. Moreover, a 300 to 600 m thick seismic sequence beneath the sea floor of the Laptev Sea with highly reflective and distinct sub-parallel pattern and interpreted as subsea permafrost (Hinz et al. 1998) was only vaguely seen in a seismic line (AWI-20080040) shot across the shelf of the ESS by RV Polarstern in 2008. Other than in the Laptev Sea, in the outer ESS, frozen sediments were not cored yet. Also, so far landforms indicative for permafrost (e.g. pingos, as they were found in the Chukchi Sea, Jin and Riedel 2013) were not observed in the ESS during the RVs Polarstern and Araon expeditions. Thus, at least for the outer area of the shelf, the presence and state of subsea permafrost in the ESS remains yet unknown and the interpretation of the two lines of available acoustic data remains speculative until more data becomes available during the Araon expedition ARA07B.

1.1.6. The Holocene ice cover and the problem of methane release from sediments

One 2.2 m long core was recovered during the RV Polarstern expedition in 2008 from the ESS shelf at 60 m water depth and revealed a basal age of 10,300 calendar years (Stein et al. in review). It did not penetrate to the base of the top unfrozen sediment unit. Together with results from a second shelf-sediment core from the Chukchi Sea, Stein et al. (under review) present the first biomarker-based (“IP25“) sea-ice records from the area. These new biomarker data are interpreted in terms of Holocene changes in sea-ice cover in relation to changes in primary production and Pacific-water inflow. There is indication for a minimum sea ice extent during the Early Holocene (10,000-8,000 cal. yrs. BP) when the global sea level rose from -40 m to -20 m compared to today (Stanford et al. 2011) and large parts of the ESS were already flooded. This is followed by a Mid-Holocene high-amplitude variability in sea ice, primary production and Pacific-water inflow and significantly increased sea-ice extent during the last about 4,500 calendar years. Main factors controlling the millennial changes in sea ice (and surface-water productivity) were changes in surface water and heat flow from the Pacific into the Arctic Ocean as well as the long-term decrease in summer insolation. Influence of Pacific water on nutrient input and productivity was much larger at the Chukchi Sea compared to the ESS (Stein et al. under review).

The development during the Holocene and, in particular, the rapid decrease of sea ice in the Arctic Ocean over the last decades (Johannessen et al., 2004, Serreze et al., 2007; Stroeve et al., 2007, 2012) raises the question how this has been influencing the subsea permafrost. The latter is expected to hold large amounts of methane in sediments as gas hydrates and free gas possibly vulnerable to be released to the water column and eventually to the atmosphere. Sea ice is of particular importance in this context because it serves as a natural physical barrier that restricts CH-4 emissions from the ESS during the ice-covered period (Shakova et al. 2016). A Swedish-Russian-US expedition in the ESS in 2014, SWERUS-C3, had a specific focus on the climate-cryosphere-carbon interactions, which included hydro-acoustic mapping of gas seeps and analysis of methane in the water column and sediments (Jakobsson et al. 2015, Mayer et al. 2015). So far most of the preliminary results of this expedition have been published in conference abstracts only. The main results and conclusions are that in the western Arctic Ocean, 34 gas seeps were mapped mostly in the Harald Canyon (Mayer et al. 2015), where the highest upward methane fluxes were also found in the sediments (157 mmol/m^2, Miller et al. 2015). Elsewhere on the slope of the ESS, fluxes were lower to negligible, which contradicts previous assumptions of high flux rates along the ESS (Miller et al. 2015). This is consistent with numerical simulations to assess the potential of gas hydrate dissociation and methane release from the East Siberian slope over the next 100 years, which shows to be relatively slow. Even if released to the atmosphere, amounts would be minimal compared to present day atmospheric methane inputs from other sources (Stranne et al. 2015). The investigation of the dynamics of methane release from the sediments of the ESS turned out to be complicated, since in areas where bubble flares were identified by acoustic echosounder imaging, recovered sediment cores provided evidence for only slightly elevated porewater methane concentrations 10 cm below the sediment surface relative to sides without flares (Bruchert et al. 2015). Porewater concentrations of CH-4 were more than a factor 300 below the gas saturation limit at sea-surface pressure. This suggests that advective methane seepage is a spatially limited phenomenon that is difficult to capture with naval-based core sampling methods (Bruchert et al. 2015). The problem is underlined by results from multi-year measurements of methane in the water column from Arctic Ocean shallow seas including the EES. The concentration of dissolved CH-4 measured in the surface waters in all of the investigated areas were supersaturated relative to the atmosphere, and anomalously high concentrations of up to 5,000-12,000% of super-saturation was found in the East Siberian Shelf, which may be in context of high concentrations and seasonal amplitudes of atmospheric methane found in NOAA/CMDL data in particular in high northern latitudes (Kosmach et al. 2015). This demonstrates the complexity in understanding of the dynamics of gas stored and released from the ESS and raises the question how important the outer shelf area of the ESS is within this context.

1.2. Sedimentary Cover, Permafrost and Methane Emission in the East Siberian Shelf.

Formation of the sedimentary cover on shelf of the East Siberian Sea is closely connected with eustatic oscillation of the sea level in Late Cenozoic time (Patyk-Kara, Dryushchitz, 2009). During Late Cenozoic, sea level of the Arctic seas dropped down several times up to the inner shelf. These oscillations started with broad regression on the boundary between Miocene and Pliocene, which appeared on the whole northern shelf of Eurasia. The traces of intensive regression in the end of middle Neo-Pleistocene ice age (186-127 ka) were stored on inner shelf of the Chukchi Sea, where the deepest coast line is now located at a depth of 135 m (Hopkins, 1976). Regression of the early Valday time reached -20 to -30 m; during the LGM, the sea levels dropped to 100 m and even more. As a result, shelf was drained on a distance of hundred kilometers. It is suggested that in the second half of Pliocene and in LGM valleys, some large rivers in flowing into the East Siberian Sea were extended on more than 1000 km in comparison to their recent lengths. Some rivers merged with the shelf area, forming large valleys with width of 80 to 90 km and large continuous valleys came to exist near the eastern boundary of the East Siberian shelf.

This time period is characterized by very quick changes of environment, during which in a very short period of time a huge territory of the shelf of the Eastern Arctic was draining. Therefore, Late Cenozoic sedimentary cover and morphology of the modern shelf was mainly formed by activity of rivers and lakes (regressive stage). Morphology of the inner and middle shelf was being smoothed and new coast lines appeared during the following transgression stage.

In the beginning of Late Cenozoic, the permafrost started to develop in glacial continental environments (Patyk-Kara, Dryushchitz, 2009). Presence of the permafrost has defined the formation and reservation of submarine accumulation of gas hydrates. As far as processes of permafrost and gas hydrates accumulation started before Holocene, these formations have a relict origin.

Study of the thawing of permafrost, lakes formation in the thermokarst, shore erosion, inflow of organic matter by Siberian rivers on shelf and dissociation of the gas hydrates in the submarine permafrost has shown increase of methane emission value that can accelerate global warming (Christensen et al., 2004; Friborg et al., 2003; Shakhova et al., 2009a,b; Walter et al., 2006;2007). Data obtained in shelf of Eastern Arctic Seas (EAS) show high-level concentration of methane especially on the shelf of Laptev Sea in comparison with latitudinal average (Shakhova et al., 2005, 2007, 2009). Based on these data, the hypothesis of great increase of methane content in atmosphere ("methane bomb") due to thawing of permafrost and gas hydrates dissociation was suggested [Shakhova et al., 2010]. This hypothesis is widely discussed in scientific literature and media, but is not well supported by modeling and paleoclimate studies (Anisimov, 2007; Anisimov et al., in press).

Another hypothesis suggests that on shelf of the EAS, methane is derived not from permafrost but from deep layers wherein methane flux intensity cannot change so quickly in the last century (Dmitrenko et al., 2011). Increase of methane flux in the atmosphere, if any could be connected with higher biogenic activity in sub-surface sediment layer due to increasing of organic matter in inflow of the river and rise of temperature of the bottom water. According to oceanographic data, subbottom temperatures from the middle of 80s up until recently increased at 2.1ºC during the summer time.

1.3. Submarine Landslides and Consequent Tsunami in the Arctic Ocean

Cruise RV Araon ARA07C was devoted to the study of geological processes related to subsea permafrost and gas hydrate destabilization, including their influence on slope failure and other geohazards in the Arctic Ocean. The study area of ARA07C cruise was located on shelf of the Eastern Siberian Sea and on western slope of the Chukchi Plateau (Figure 1.1). Processes of the slope failure in this area and broader region including eastern Barents Sea, Kara, Laptev and Chukchi Seas were not study until now. On the other hand, investigations of this question carried out in Norwegian-Greenland Sea region revealed a number of landslides and showed that both unloading earthquakes and hydrate failure were key factors causing several mega-landslides off of Norway during early Holocene deglaciation.

1.3.1. Submarine landslides

In the Arctic region, the main part of landslides was founded and discovered in the Norwegian-Greenland basin in connection with the prospecting investigations for oil and gas. Several landslides were studied on Beaufort Sea slope, however information on landslides on slopes of the eastern Barents, Kara, Laptev, East Siberian and Chukchi Seas are lacking (Figure 1.1)

In the description of the landslide location we will use the term «landslide territory». This term was introduced by Hampton et al., (1996) for environments where landslides are widely distributed due to unique combination of sedimentation parameters and physiography. Such environments include (1) *fjord*, (2) *active river delta on the continental margin*, (3) *submarine canyon-fan system*, (4) *the open continental slopes*, (5) *oceanic volcanic islands and ridges*. All these environments can be distinguished in the Arctic Ocean and landslides have been found in each of them.

Fjords. Submarine landslides are often occurred in fjords represented by iceberg eroded valleys flooded by sea. In Arctic region landslides were found in fjords of the Norway and Svalbard (Figure 1.1). Their studies showed that these landslides have small sides but can generate significant tsunami waves (Hampton et al., 1996; Yamada et al., 2012).

Active river delta on the continental margin. The sediments can accumulate during the transit from river mouth to the continental margin. These accumulated sediments may cause a failure in the formation of landslides, which significantly modify permanent relief of this shallow areas (*Hampton et al., 1996*). Such type of landslide in the Arctic region occurs on southern slope of the Canadian Basin, Mackenzie fan, Beaufort Sea (Figure 1.1). Height of its headwall is 80 m at depth of 115 m, the landslide scar continues at least up to 700 m bsl and the landslide of such dimension might generate a tsunami (Mosher, 2009). The main trigger mechanism of this slope failure is thought to be seismicity among high sedimentation rates, variations in permafrost thickness and existence of significant amount of gas and gas hydrates (Mosher, 2009; Paull et al. 2007). Analysis of the sedimentary cover on slope suggests that this area is now stable (Hill et al., 1982). Increase of the pore pressure due to gas hydrates disintegration or strong earthquake will be the triggers for further slope failure.

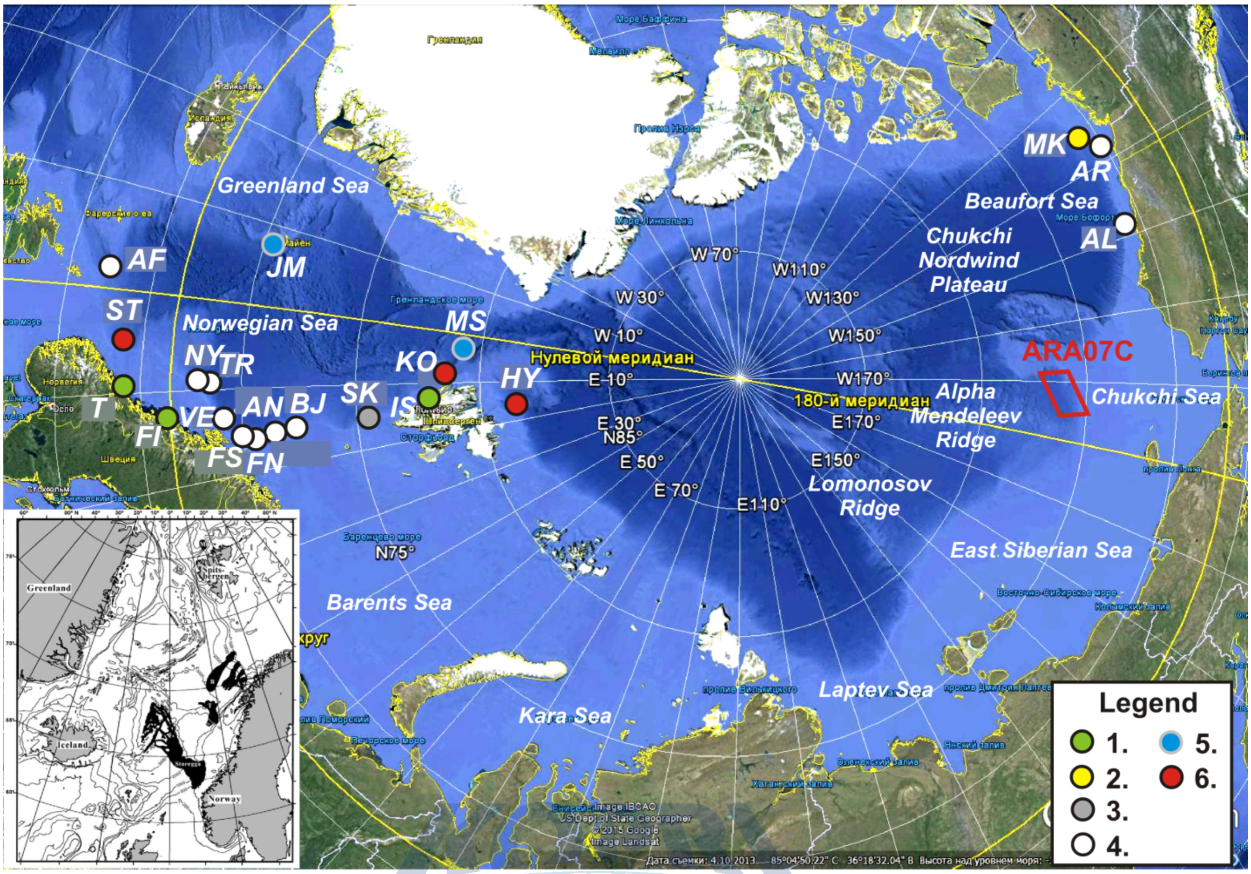

Figure 1.1. Location of the submarine landslides in the Arctic Ocean. In Google map the landslides have been shown without scale. Inset gives imagination about sizes of the landslides marked by black on Norwegian slope (*Haflidason et al., 2004*).

Legend

1. *Fjords*: ***FI*** - Finneidfjord (Canals et al., 2004, Vanneste et al., 2012), ***TR*** – Trondheimsfjorden (Lyså et al., 2008), ***IS*** - Isfjorden (Forwick, Vorren, 2012).
2. *Active river delta on the continental margin:* ***MK*** – Mackenzie delta (Mosher, 2009).
3. *Submarine canyon-fan system*: ***SK*** – Storfjorden and Kveithola (Lucchi et al., 2012).
4. *The open continental slope*: ***ST*** – Storegga, ***TR*** –Traenadjupet, ***AF*** –Afen, ***NY*** –Nyk, ***BJ*** - Bjørnøyrenna, ***FBs*** – Fugløy Bank south, ***FBn*** – Fugløy Bank north, ***AN*** – Andøya, (Haflidason et al., 2004; Canals et al., 2004), ***VE*** – Vesterålen (Rise et al., 2012), ***AL*** – Alaskan Beaufort Sea slope (Gr07antz, Dinter, 1980), ***AR*** – Araon Slide (Jin et al., 2013).
5. *Oceanic islands and ridges:* ***MS*** – Molloy Slide (Freire et al., 2014); ***JM*** – Jan Mayen Slide (Laberg et al., 2014).
6. Landslides that have generated tsunamis according to field observations (Storegga Slide - ***SR***) or numerical modeling (Hinlopen-Yermak slide – ***HY***) (Vanneste et al., 2010) and Kongsfjord trough (future slope failure) – ***KO*** (Bernd et al., 2009).

Red box indicates study area of ARA07C cruise.

<u>Submarine canyon-fan system.</u> Submarine canyons exist overall on the continental slope and serve as transport channels forming giant submarine fan near their mouths. Twelve separate landslides were distinguished on the continental slope to the north from Svalbard. The slide scars have amphitheatre shape and were located in the middle and upper slope on the fans in the mouths of Storfjorden and Kveithola Throughs (Figure 1.1) (Lucci et al., 2012). Landslide

headwalls were located on depths of 600-800 m and had a height of 15-40 m. The biggest landslide originated at several time intervals and had an area of 1120 km^2.

Open continental slope. Continental slopes are the areas through which the sediment mass moves from land to sea basin. High continental slope reaches few kilometers and inclination can be up to several degrees. Potential opportunity of slope failure and landslide generation can appear on slope during a change in sea level. The main part of landslides in the Arctic region is located in this environment (Figure 1.1). They have different dimensions and their size/volume change from 40 km^2/0,2 km^3 up to 90000 km^2/3000 км^3 for Afen and Storegga Slides, respectively.

The Storegga Slide was studied in much detail and can serve as a representative example of landslides in environment of open continental slope (Haflidason et al., 2004). Slope failure and Storegga landslide generation occurred at the end of LGM or immediately after deglaciation (i.e. about 8000 years ago). Destabilization, due to loading of ice-rafted material, appeared before sediments slamping. The pore pressure has been increasing and effective shear in underlaying mud was reduced. Seismic shock and destabilization of the gas hydrates might trigger mechanism for this event. A similar sequence of events may be typical for all landslides formed in high latitudes exposed to glaciers.

Oceanic volcanic islands and ridges. Two landslides were discovered in the central Norwegian-Greenland Sea, namely on Jan Mayen Rdge and Molloy Ridge (Figure 1.1). Jan Mayen Ridge is a microcontinent and the landslide is located on its western side. The slide scar has an amphitheatre shape with a width of 60 km. The landslide was probably formed in two time intervals and its total volume of mass transported deposits was equal to 60 km^3 (Laberg et al., 2014).

The second landslide was mapped in the deepest part of Arctic region – Molloy Hope is located to the west from continental slope of the Svalbard Island (Figure 1.1). Geophysical surveys revealed a slide scar, which indicates larger-scale mass wasting. The material was transported from axial valley of the Molloy Ridge to the Molloy Hole and its volume was 65 km^3. Unique feature of this landslide is that its run-out distance was very small (<5 km) compared with high difference in depth (>2,000 m) between its head and tail parts. Earthquake connected to sea-floor spreading on the Molloy Ridge was probably the trigger of this landslide along with gas-hydrate destabilization, which may also have played a role in the ensuing slide event (Freire et al., 2014).

1.3.2. Tsunami

Recent data offer evidence that landslides together with earthquakes may also generate a tsunami. Landslide tsunamis in contrast with earthquake tsunamis have usually a local distribution but the same magnitude and may be very destructive to the nearest shore (Tappin, 2010). Historic data on landslide tsunami in Arctic Ocean is insufficient and all information comes from investigations of paleotsunami and numerical modeling of slope failure and landslide generation.

Paleotsunamis of the Arctic Ocean were studied on shores of Norway (Bondevik et al., 1997), Faroe Islands (Grauert et al., 2001), Scotland (Dawson et al., 1993) and Shetland Islands (Bondevik et al., 2003). It was found that run-up reached 3-12 m, more than 10 m and 3-6 m on shores of Norway, Faroe Islands and Scotland, respectively (Figure 1.2). Maximal run-up of 20 m was recorded on Shetland Islands located between Norway and Scotland. Age of tsunami deposits is 7300 y.e. and corresponds to the age of Storegga Slide when 3500 km^3 of sediments have moved downslope offshore Norway (Bondevik et al., 1997; Haflidason et al., 2004).

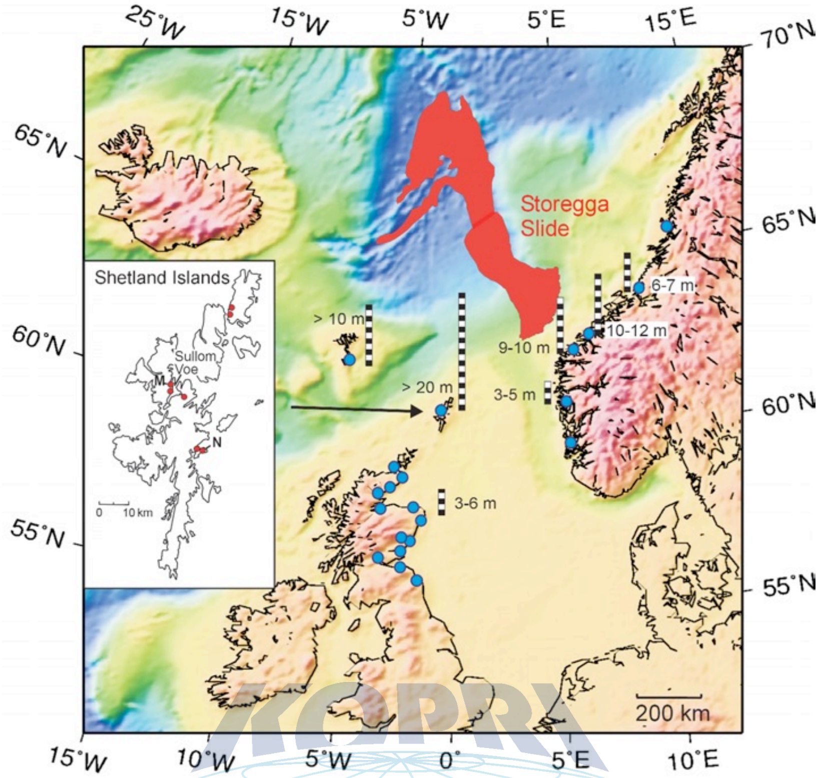

Figure 1.2. Storegga Slide on the Norwegian slope and locations of the areas where tsunami deposits of this landslide were found (circles filled by blue). Digits indicate the height of tsunami deposits relative to recent sea level. Maximal runup was found on the Shetland Islands where red filled points indicate location of tsunami deposits (inset) (Dawson et al., 1993; Bondevik et al., 1997a; Grauert et al., 2001; Bondevik et al., 2003).

Tsunamis generated by submarine landslides were modeling for two areas in the Arctic Ocean. First area corresponds to known landslide and second ones to area where slope failure may be occurred in a future. First area is the Hinloppen-Yermak slide (Figure 1.2) that according to numerical modeling might generate abnormally high tsunami due to big volume and high velocity of movement of the deposits. In one of the scenario, the run-up on Svalbard shore located 20 km from tsunami source was 40 m (Vanneste et al., 2010).

Second region is located on fan of the Kongsfjord trough off western coast of the Svalbard Island. This fan compare with other fans was not failure during last deglaciation. Recently, increas of water temperature, destabilization of the gas hydrates and increase of pore pressure can cause a slope failure. Numerical modeling suggesting that a landslide with headwall of 100 m height and 130 km of length shows that in this case, the landslide will generate a tsunami with run-up of 5 m on Svalbard, 4-5 m on Norway and Iceland shores and about 3 m on shores of the Farer Islands (Berndt et al., 2009).

High probability of slope failure and tsunami generation in Mackenzie active river delta is also suggested. This tsunami may have significant danger for flat shores of the Beaufort Sea on which oil and gas are explored (Mosher, 2009).

References

Anisimov, O. A. (2007). Potential feedback of thawing permafrost to the global climate system through methane emission. *Environmental Research Letters*, *2*(4), 45016. http://doi.org/10.1088/1748-9326/2/4/045016

Anisimov O.A., Borsenkova I.I., Lavrov S.A. Recent dynamics of the submarine permafrost and methane emission in shelf of Eastern Arctic seas in contents of past and future climate changes, in press. (in Russian).

Berndt, C., Brune, S., Nisbet, E., Zschau, J., & Sobolev, S. V. (2009). Tsunami modeling of a submarine landslide in the Fram Strait. *Geochemistry, Geophysics, Geosystems*, *10*(4). http://doi.org/10.1029/2008GC002292

Bondevik, S., Svendsen, J. I., Johnsen, G., Mangerud, J., & Kaland, P. E. (1997). The Storegga tsunami along the Norwegian coast, its age and run up. *Boreas*, *26*(April), 29–53. http://doi.org/10.1111/j.1502-3885.1997.tb00649.x

Bondevik, S., Mangerud, J., Dawson, S., Dawson, A., & Lohne, Ø. (2003). Record-breaking height for 8000-year-old tsunami in the North Atlantic. *Eos, Transactions American Geophysical Union*, *84*(31), 289. http://doi.org/10.1029/2003EO310001

Canals, M., Lastras, G., Urgeles, R., Casamor, J. L., Mienert, J., Cattaneo, A., … Bryn, P. (2004). Slope failure dynamics and impacts from seafloor and shallow sub-seafloor geophysical data: Case studies from the COSTA project. *Marine Geology*, *213*(1–4), 9–72. http://doi.org/10.1016/j.margeo.2004.10.001

Christensen, T. R. (2004). Thawing sub-arctic permafrost: Effects on vegetation and methane emissions. *Geophysical Research Letters*, *31*(4), L04501. http://doi.org/10.1029/2003GL018680

Dawson, A. G., Long, D., Smith, D. E., Shi, S., & Foster, I. D. L. (1994). Tsunamis in the Norwegian Sea and North Sea caused by the Storegga submarine landslides. *Tsunamis of the World,* 31–42.

Dmitrenko, I. A., Kirillov, S. A., Tremblay, L. B., Kassens, H., Anisimov, O. A., Lavrov, S. A., Razumov, S. O., & Grigoriev, M. N. (2011). Recent changes in shelf hydrography in the Siberian Arctic: Potential for subsea permafrost instability. *Journal of Geophysical Research*, *116*(C10), C10027. http://doi.org/10.1029/2011JC007218

Freire, F., Gyllencreutz, R., Jafri, R. U., & Jakobsson, M. (2014). Acoustic evidence of a submarine slide in the deepest part of the Arctic, the Molloy Hole. *Geo-Marine Letters*, *34*(4), 315–325. http://doi.org/10.1007/s00367-014-0371-5

Friborg, T. (2003). Siberian wetlands: Where a sink is a source. *Geophysical Research Letters*, *30*(21), 2129. http://doi.org/10.1029/2003GL017797

Forwick M., Vorren T.O. (2012). Submarine Mass Wasting in Isfjorden, Spitsbergen // In: Y. Yamada et al. (eds.), Submarine Mass Movements and Their Consequences, *Advances in Natural and Technological Hazards Research 31*, DOI 10.1007/978-94-007-2162-3_15, © Springer Science+Business Media B.V., P. 711-722.

Grauert, M., Björck, S., & Bondevik, S. (2001). Storegga tsunami deposits in a costal lake on Suðuroy, the Faroe Islands. *Boreas*, *30*, 263–271.

Haflidason, H., Sejrup, H. P., Nygård, A., Mienert, J., Bryn, P., Lien, R., Forsberg, C., Berg, K., & Masson, D. (2004). The Storegga Slide: Architecture, geometry and slide development. *Marine Geology*, *213*(1–4), 201–234. http://doi.org/10.1016/j.margeo.2004.10.007

Hampton, M. A., Lee, H. J., & Locat, J. (1996). Submarine landslides. *Reviews of Geophysics*, *34*(1), 33–59. http://doi.org/10.1029/95RG03287

Hill, P. R., Moran, K. M., & Blasco, S. M. (1982). Creep deformation of slope sediments in the Canadian Beaufort Sea. *Geo-Marine Letters*, *2*(3–4), 163–170. http://doi.org/10.1007/BF02462758

Hopkins D.M. History of the sea level changes in the Beringiya for the last 250000 years. Beringiya in Cenozoic, Vladivostok, 1974, p. 9-27.

Jakobsson, M, Polyak L., Edwards M., Kleman J., and Coakley, B. (2008). Glacial geomorphology of the Central Arctic Ocean: the Chukchi Borderland and the Lomonosov Ridge, Earth Surf. Process. Landforms 33, 526–545

Jokat, W. (2009) The Expedition of the Research Vessel "Polarstern" to the Arctic in 2008 (ARK-XXIII/3), *Reports on Polar and Marine Research*, 226p

Jin, Y.K., Riedel M., Shipboard scientific party, (2013). ARA04C Cruise Report, Korea Polar Research Institute, 174 pages.

Kristoffersen Y. and Mikkelsen N. (2003) Scientific drilling in the Arctic Ocean and the site survey challenge: Tectonic, paleoceanographic and climatic evolution of the Polar Basin JEODI Workshop, Copenhagen, Denmark

Laberg, J. S., Kawamura, K., Amundsen, H., Baeten, N., Forwick, M., Rydningen, T. A., & Vorren, T. O. (2014). A submarine landslide complex affecting the Jan Mayen Ridge, Norwegian–Greenland Sea: slide-scar morphology and processes of sediment evacuation. *Geo-Marine Letters*, *34*(1), 51–58. http://doi.org/10.1007/s00367-013-0345-z

Lucchi R. G., Pedrosa M. T., Camerlenghi A. (2012). Recent Submarine Landslides on the Continental Slope of Storfjorden and Kveithola Trough-Mouth Fans (North West Barents Sea) // In: Y. Yamada et al. (eds.), Submarine Mass Movements and Their Consequences, Advances in Natural and Technological Hazards Research 31, DOI 10.1007/978-94-007-2162-3_15, © Springer Science+Business Media B.V., P. 735-745.

Lyså, A., Hansen, L., Christensen, O., L`Heureux, J.-S., Longva, O., Olsen, H. A., & Sveian, H. (2008). Landscape evolution and slide processes in a glacioisostatic rebound area; a combined marine and terrestrial approach. *Marine Geology*, *248*(1–2), 53–73. http://doi.org/10.1016/j.margeo.2007.10.008

Mosher, D. C. (2009). International year of planet earth 7. Oceans, submarine land-slides and consequent tsunamis in Canada. *Geoscience Canada*, *36*(4), 179–190.

Patyk-Kara N.G., Dryushchitz V.A. Dynamics character of the sediments in Arctic shelf in Late Cenozoic. *Geology of Earth polar areas.* 2009, V.2, p.101-104.

Paull, C. K., Ussler, W., Dallimore, S. R., et al (2007). Origin of pingo-like features on the Beaufort Sea shelf and their possible relationship to decomposing methane gas hydrates. *Geophysical Research Letters*, *34*(1). http://doi.org/10.1029/2006GL027977

Rise, L., Chand, S., Haflidason, H., et al (2012). Investigations of Slides at the Upper Continental Slope Off Vesterålen, North Norway. In *Submarine Mass Movements and Their Consequences* (pp. 167–176). Dordrecht: Springer Netherlands. http://doi.org/10.1007/978-94-007-2162-3_15

Shakhova, N., & Semiletov, I. (2007). Methane release and coastal environment in the East Siberian Arctic shelf. *Journal of Marine Systems*, *66*(1–4), 227–243. http://doi.org/10.1016/j.jmarsys.2006.06.006

Shakhova, N., Semiletov, I., & Panteleev, G. (2005). The distribution of methane on the Siberian Arctic shelves: Implications for the marine methane cycle. *Geophysical Research Letters*, *32*(9), 1–4. http://doi.org/10.1029/2005GL022751

Shakhova N. E., Sergienko V.I., Semiletov I. P. (2009). Input of the East Siberian shelf in recent cycle of methane. *Letters of the Russian Academy of Sciences*, *6*, 507-518 (in Russian).

Shakhova, N., Semiletov, I., Salyuk, A., Yusupov, V., Kosmach, D., & Gustafsson, O. (2010). Extensive Methane Venting to the Atmosphere from Sediments of the East Siberian Arctic Shelf. *Science*, *327*(5970), 1246–1250. http://doi.org/10.1126/science.1182221

Tappin, D. R. (2010). Mass Transport Events and Their Tsunami Hazard. In *Submarine Mass Movements and Their Consequences* (Vol. 28, pp. 667–684). Dordrecht: Springer Netherlands. http://doi.org/10.1007/978-90-481-3071-9_54

Vanneste, M., Harbitz, C. B., De Blasio, et al. (2011). Hinlopen-Yermak landslide, Arctic Ocean; geomorphology, landslide dynamics, and tsunami simulations. *Mass-Transport Deposits in Deepwater Settings*, *96*(1060–071X, 1060–071X), 509–527.

Vanneste M., L'Heureux J.-S., Baeten N., et al., (2012). Landslides and Their Dynamics in Coastal and Deepwater Environments, Norway // In: Y. Yamada et al. (eds.), Submarine Mass Movements and Their Consequences, Advances in Natural and Technological Hazards Research 31, DOI 10.1007/978-94-007-2162-3_15, © Springer Science+Business Media B.V., P. 29 – 42.

Walter, K. M., Edwards, M. E., Grosse, G., Zimov, S. A., & Chapin, F. S. (2007). Thermokarst Lakes as a Source of Atmospheric CH4 During the Last Deglaciation. *Science*, *318*(5850), 633–636. http://doi.org/10.1126/science.1142924

Walter, K. M., Zimov, S. A., Chanton, J. P., Verbyla, D., & Chapin, F. S. (2006). Methane bubbling from Siberian thaw lakes as a positive feedback to climate warming. *Nature*, *443*(7107), 71–75. http://doi.org/10.1038/nature05040

Yamada, Y., Kawamura, K., Ikehara, K., et al. (Eds.). (2012). *Submarine Mass Movements and Their Consequences*. Dordrecht: Springer Netherlands. http://doi.org/10.1007/978-94-007-2162-3

Chapter 2. Multichannel Seismic Survey

S.-G. Kang, J.K. Hong, M. Lee, Y.J. Choi, and I.H. Seo

2.1. Introduction

A multi-channel seismic (MCS) survey was conducted on the continental shelf of the East Siberian Sea, Arctic Ocean, from 30 August to 2 September 2016 during the R/V Araon expedition ARA07C. The main objective of this survey was to investigate sedimentary stratigraphy, distribution of permafrost and gas chimney structures in the East Siberian shelf area. We obtained seismic data on 3 lines and the total survey length was about 665 line-km with 13,309 shots.

2.2. Methods

2.2.1. Multichannel seismic system on the Araon

The multi-channel seismic system on the Araon consisted of an airgun array, a streamer, two compressors, and survey control systems (Figure 2.1). The airgun array has eight airguns (Sercel G-Gun II) and a float that maintains the source depth as 6 meters in the water (Figure 2.2, 2.3 and 2.4a). Airguns release compressed air at the same time into the water and create an acoustic wave that is used as the source wave for the multi-channel seismic survey. Our research vessel possesses onboard an airgun array system which has four different volumes: two 250 cu.in, two 200 cu.in, two 90 cu.in and two 60 cu.in. The total volume of the source is 1,200 cu.in (~19.7 liter). In this survey, we employed only 2 airguns (each 250 cu.in) to obtain higher resolution seismic images for the shallow depth area. The total volume of the source was 500 in^3. A 1.5-kilometer solid-type streamer (Sercel Sentinel) consists of ten sections which record reflected waves and other signals like direct wave, refracted wave and background noise using hydrophones in the streamer. The group interval and channel number of the streamer were 12.5 meter and 120 channels, respectively. Total length of the streamer was 1.76 km when we include a tail buoy, two fluid sections and a lead-in cable. Six cable levelers (birds) were attached onto the streamer at every 150-meter or 300-meter so that the streamer depth was stabilized in the water (Figure 2.4b).

Seismic Compressor generates compressed air and provides high-pressured air into airguns. The compressor system of the Araon consisted of two compressors: one compressor was utilized for normal operations and the other was for stand-by. The working pressure was maintained at 150-bar (~2030 psi) during seismic-data survey. A seismic control system installed in the main dry lab consisted of a navigation control system, an airgun controller, a bird controller, a recording system, a quality control system and a navigation editing system (Figure 2.5).

The navigation system (EIVA NaviPac) controls position along the seismic lines and the event type, shooting interval, event start/stop with the gun controller and recording system. The airgun controller (RTS-Real Time Systems Bigshot), receives the event signal from the

NaviPac and sends trigger signals to airguns. The Bigshot system displays the shooting-timing, quality and wave shape of all airguns. The bird controller defines streamer depth and displays the location, heading and all stations of the individual birds. The recording system, Baby Seal from Sercel, records all seismic data and copies all data to the final storage system. The quality control system (Sercel e-SQC pro) displays the realtime data such as shot gather and near trace gather. The navigation editing system (EIVA NaviEdit) transforms the NaviPac survey files to standard navigation files such as UKOOA P1/90 or other forms.

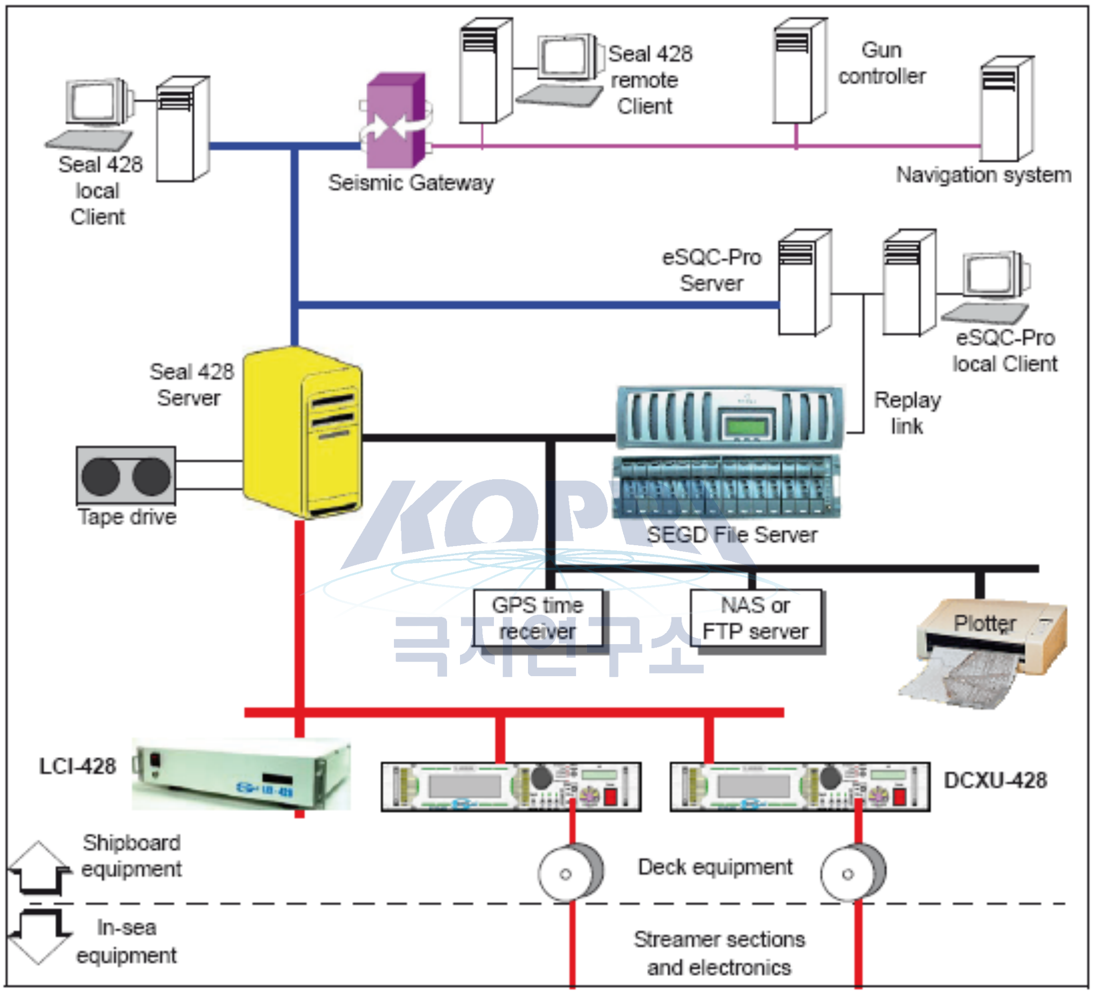

Figure 2.1. Schematic diagram of the multi-channel seismic system on the Araon.

Figure 2.2. Airguns attached to the airgun array.

Figure 2.3. Deployment of the airgun array.

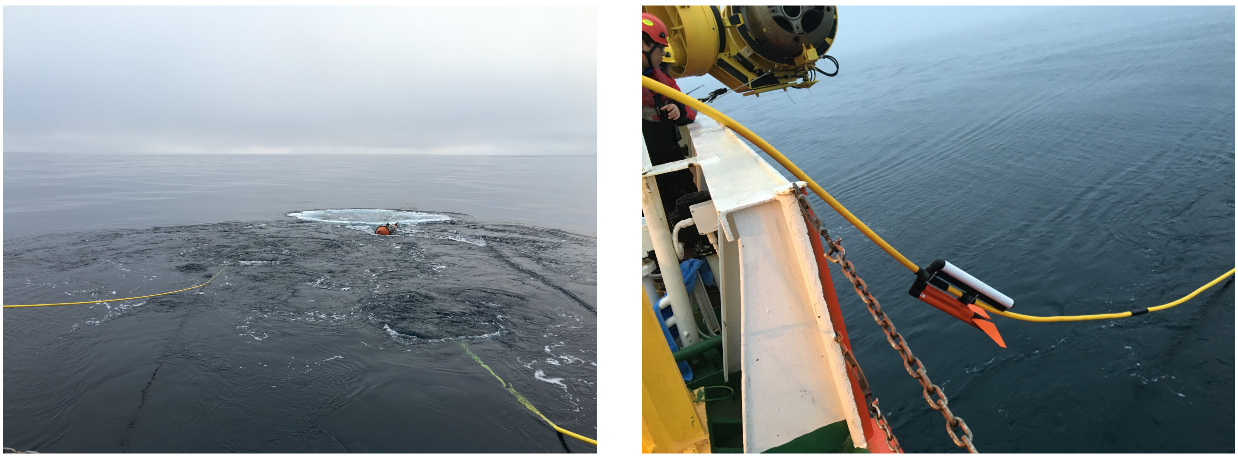

Figure 2.4. (left) Airgun array is launched into the sea. A float (red color tube) maintains the source depth as 6 meter in the water, (right) Launching the streamer with the cable leveler (bird).

Figure 2.5. The seismic survey control system in the Main Dry Lab. Navigation, airgun controller, bird controller, recording system and quality control system are shown.

2.2.2. Acquisition parameter

Table 2.1 shows the acquisition parameters of the multichannel seismic survey during Expedition ARA07C. The shooting interval was 50.0 m for most survey lines. Considering a group interval of 12.5 meter and 120 channels, a fifteen-fold common-mid-point gather was achieved. Working pressure was about 120 bars. The source depth was 6 meter and the streamer depth was set at the same value as the source depth. However, these depths can slightly vary weather conditions, currents, and ship speed. Record length and sampling rate were set as 10.0 seconds and 1 millisecond, respectively. The recorded data-file format was SEG-D. Figure 2.6 shows field configurations of this seismic survey.

Table 2.1. Seismic acquisition parameters.

Shot Interval	50.0 m
Channel Number	120 ch
Group Interval	12.5 m
Source Depth	6 m
Streamer Depth	6 m
Fold of Coverage	15 folds
Work Pressure	120 bar
Recording Length	10.0 sec
Sample Rate	1 ms
Tape Format	SEG-D

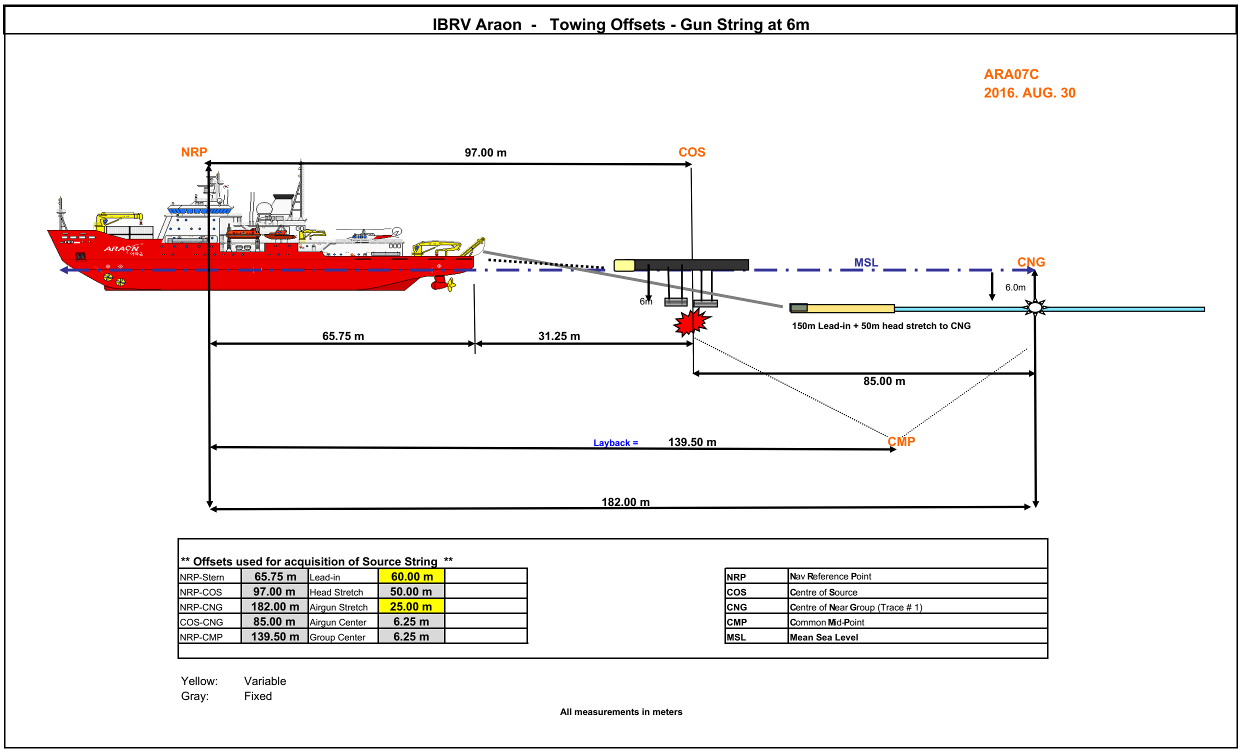

Figure 2.6. Field acquisition parameters and layouts.

2.3. Results

2.3.1. Data acquisition

The multi-channel seismic data collected during the ARA07C expedition consisted of 3 survey lines, 665 L-km and 13,309 shot gathers (Figure 2.7) from 30 August to 2 September. During this survey, we used two 250 cu.in airgun array to generate the source of seismic survey. All guns fired well and working pressure was stably maintained as 120 bar for the entire survey time. Total volume of the airgun array kept 500 cu.in and acquired data show nice shot gathers with clear reflections. Our survey was stopped because of sea ice conditions during the last survey line. We were not able to keep the planned survey line in order to avoid the sea ice in the northern part of Line 3. We covered 87 percent of planed survey lines without any technical problems.

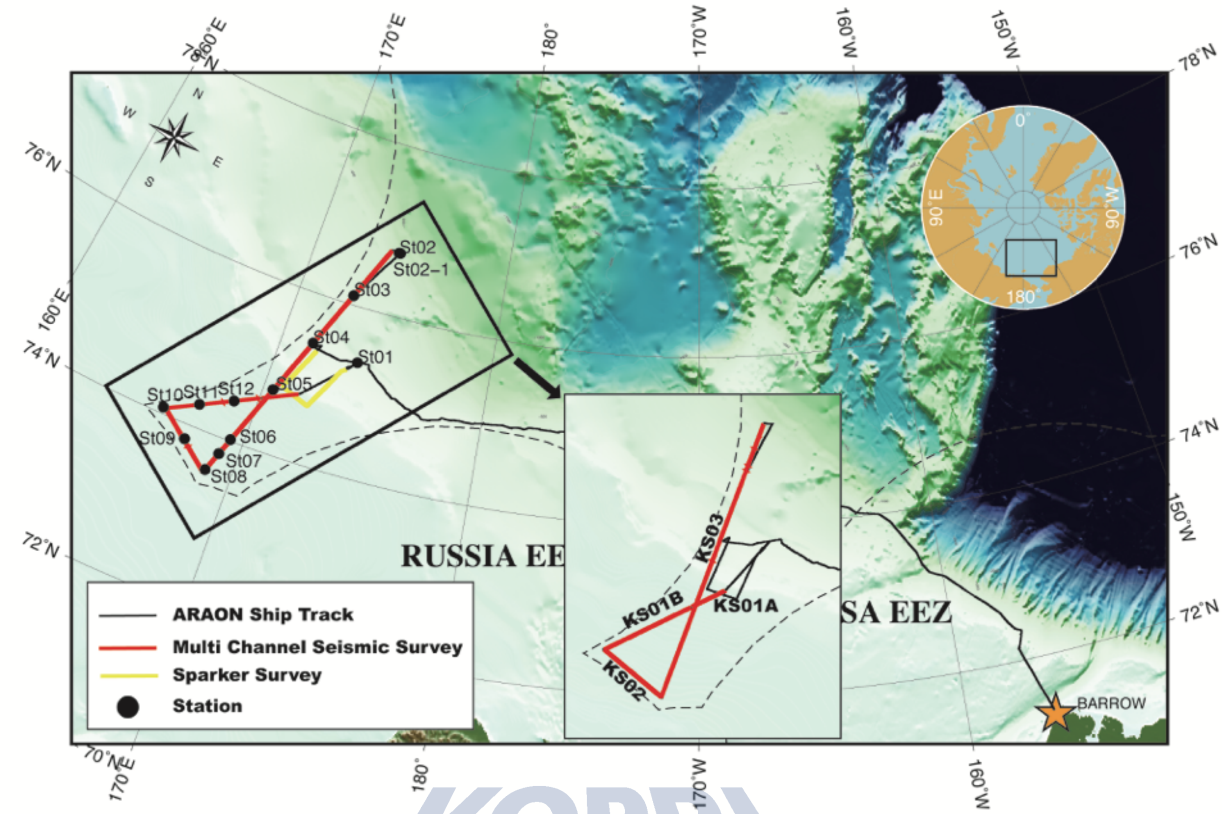

Figure 2.7. Track chart of the seismic survey of Expedition ARA07C.

2.3.2. Data processing and analysis

Some portions of the acquired seismic data were processed onboard to generate a stack image with the seismic data processing software (GEDCO VISTA 10.0). The seismic data processing sequence consisted of SEG-D file reading, band-pass filtering, recording delay correction, geometry setting, velocity analysis, normal moveout (NMO) correction, and common mid-point (CMP) stacking. Due to very shallow water depth of around 50 m over the majority of the continental shelf in the study area, the direct wave and refracted waves overlapped with primary reflection signals.

The seismic profile ARA07C-KS03 crosses the shelf edge and shows geological structures and chaotic stratigraphy (Figure 2.8 and 2.9). In this seismic stack image, we can check the sedimentary sequences and stratigraphy beneath the seafloor, but specialized processing techniques, such as SRME or tau-p transform, are required to remove several multiple and noise components. In addition, gas chimney structures from the deeper part of the section are clearly defined. For more accurate and detail seismic sequence interpretation, specialized processing sequences such as multiple attenuation, deconvolution, and migration are required after this cruise.

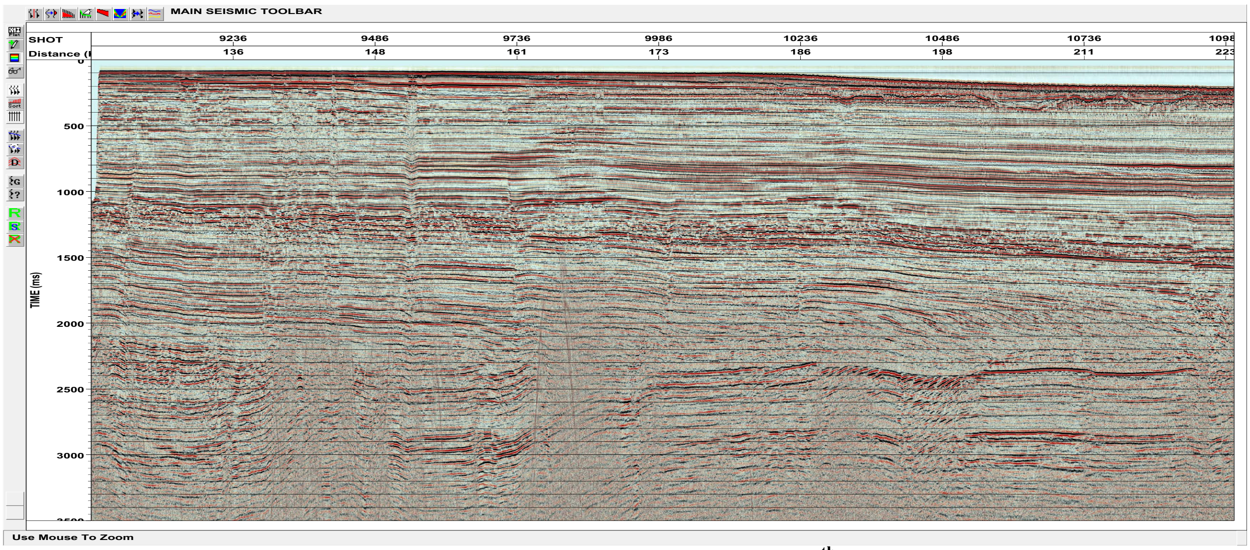

Figure 2.8. A stack section of ARA07C-KS03-A (9001-11000th shot point number).

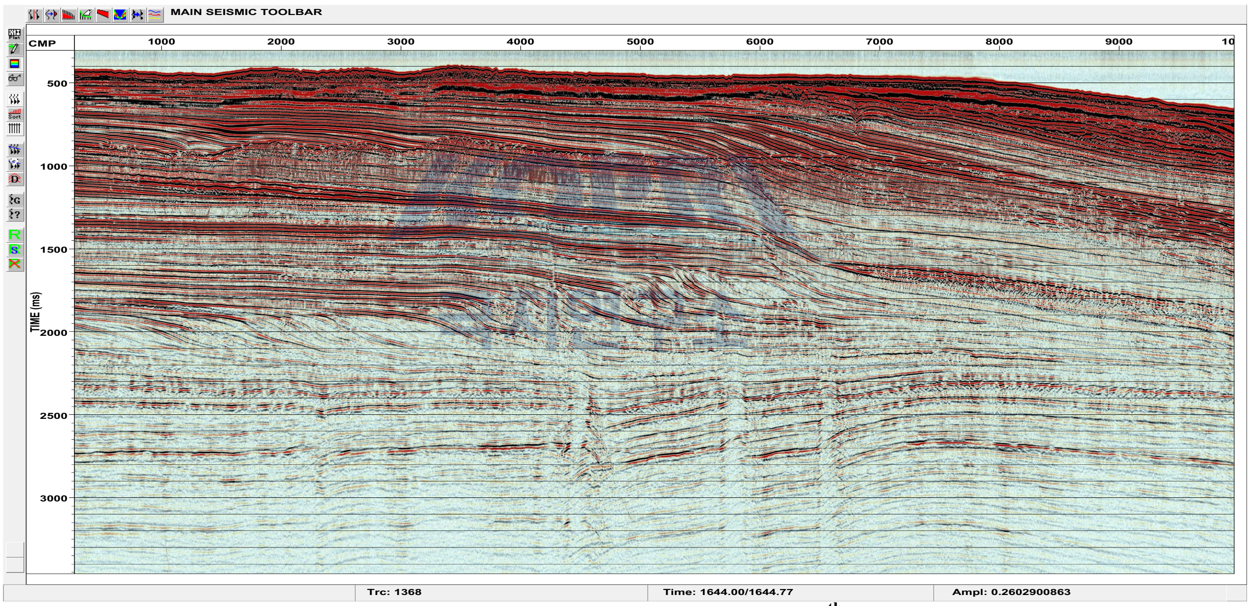

Figure 2.9. A stack section of ARA07C-KS03-A (13001-14310th shot point number).

2.4. Summary

Multi-channel seismic data were acquired on the East Siberian shelf. 3 seismic lines with 665 line-km and 13,309 shot gathers were collected from 30 August to 2 September 2016. All seismic equipment operated in good condition without any problem so that we acquired good-quality seismic data.

Chapter 3. Multi-Beam and Sub-Bottom Profile Surveys

H.J. Kim, and S.-G. Kang

3.1. Introduction

Swath bathymetry and high-resolution reflection data (~3.5KHz) were collected during the ARA07C cruise. Sea floating ice flows were not densely distributed and wind and waves were mild and calm. Because of the relatively good sea conditions, we were able to acquire geophysical data with high signal-to-noise ratio. When the ship was ramming to find a thick multi-year ice flow for an ice station, however, very noisy data were acquired due to the interference to the transducers by crashed ice.

From August to September, 2016, KOPRI conducted an oceanographic survey in the East Siberian Sea and Chukchi Sea, Arctic Ocean. During the Expedition ARA07C, we collected Multi-Beam and SBP data.

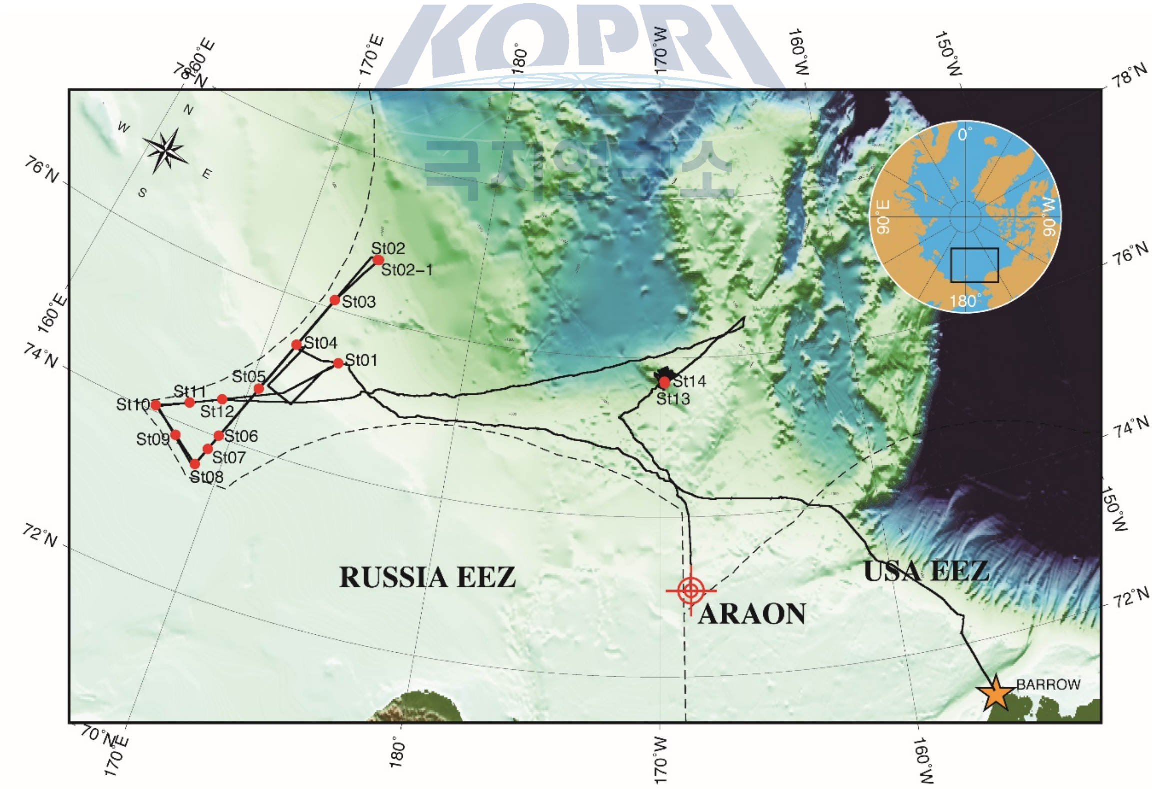

Figure 3.1. Map showing all tracks of the Expedition ARA07C. Total length of the line is more than 2240 nautical miles. MB and SBP data were recorded when the vessel moved along survey lines.

3.2. System Description

3.2.1. Multi-beam echo sounder

The Multi-Beam system consists of a hull-mounted transmitter and receiver transducer, transceiver unit, and operator station (Figure 3.2).

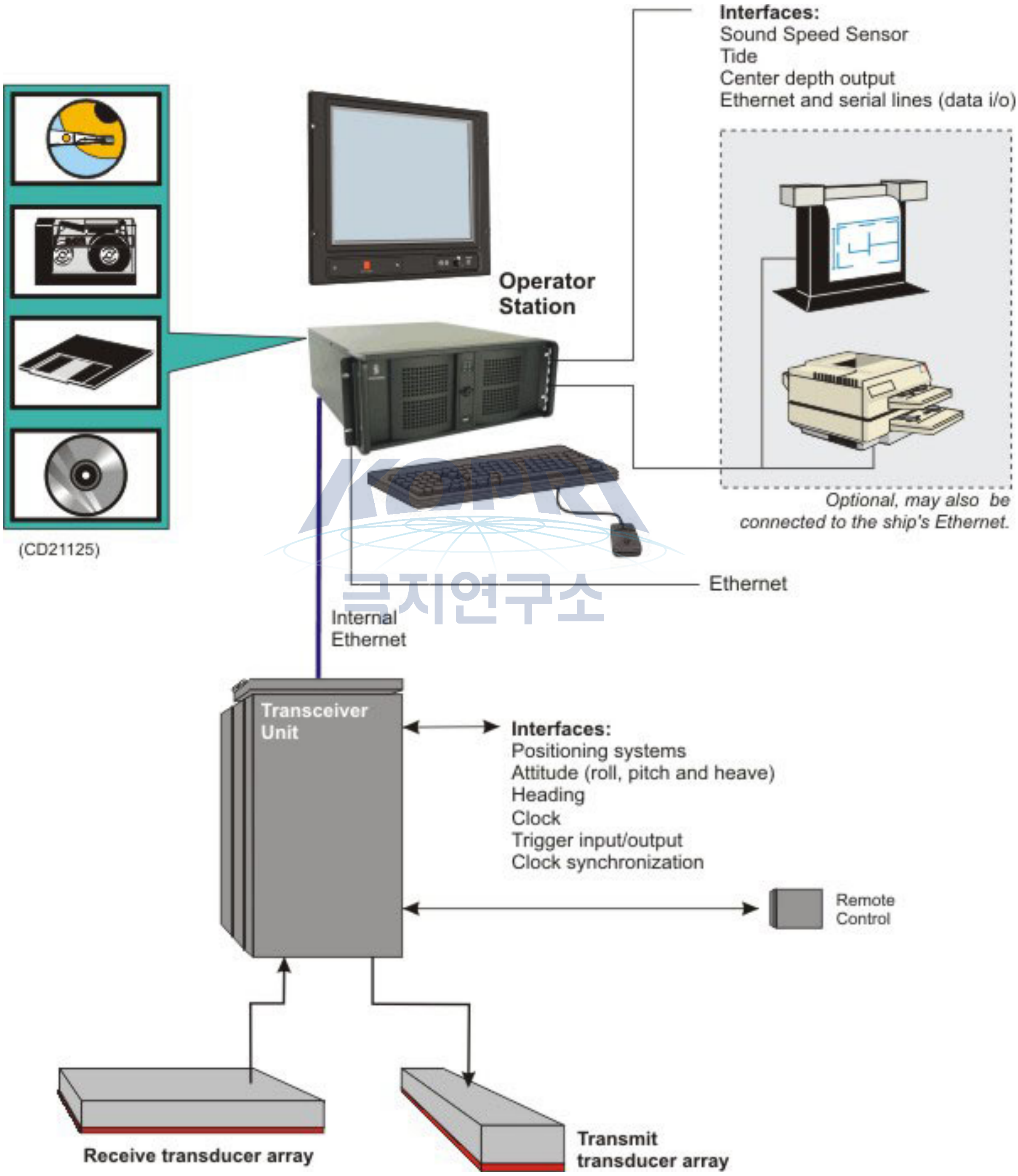

Figure 3.2. System diagram of EM122 Multi-Beam system.

EM122 has a wide beam angle (-60 ~ 60 degrees) and a capability of measuring into the deep ocean. The technical specifications of EM122 are listed at Table 3.1.

Table 3.1. Technical specifications of EM122.

Operating frequency		12 kHz
Depth range		20 – 11000 m
Swath width		6 × Depth, to approx 30 km
Pulse forms		CW and FM chirp
No. of beams		288
Swath profiles per ping		1 or 2
Motion compensation	**Yaw**	± 10 degrees
	Pitch	± 10 degrees
	Roll	± 15 degrees
Sounding pattern		Equi-distant on bottom/equiangular
Depth resolution of soundings		1 cm
High resolution mode		High Density processing
Sidelobe suppression		-25 dB
Modular design, beamwidth		0.5 to 4 degrees

3.2.2. Sub-bottom profiler

The SBP120 Sub-bottom profiler installed on the ARAON is an optional extension to the EM122 Multi-Beam Echo Sounder. Figure 3.3 shows the SBP system diagram.

The receiving transducer hydrophone array used by the EM122 Multi-Beam system is a broadband system; by adding a separate low frequency transmitting transducer and electronic cabinets and operator stations, the EM122 can be extended to include the sub-bottom profiling capability, as provided by the SBP120. System beamwidth is 12 degrees with 24 transducers, equivalent to a footprint of 20 m in 100 m water depth (or 20% of waterdepth).

The frequency range of the SBP120 is 2.5 to 7 kHz. The SBP120 beam is electronically stabilized for roll and pitch. It can also be steered to take into account bottom slope. The ping rate is synchronized to that of the Multi-Beam Echo Sounder transmitter if both are running simultaneously.

The data produced by SBP120 is logged in the Topas .raw format and can be converted to SEG-Y format that allows post-processing by standard seismic processing software packages.

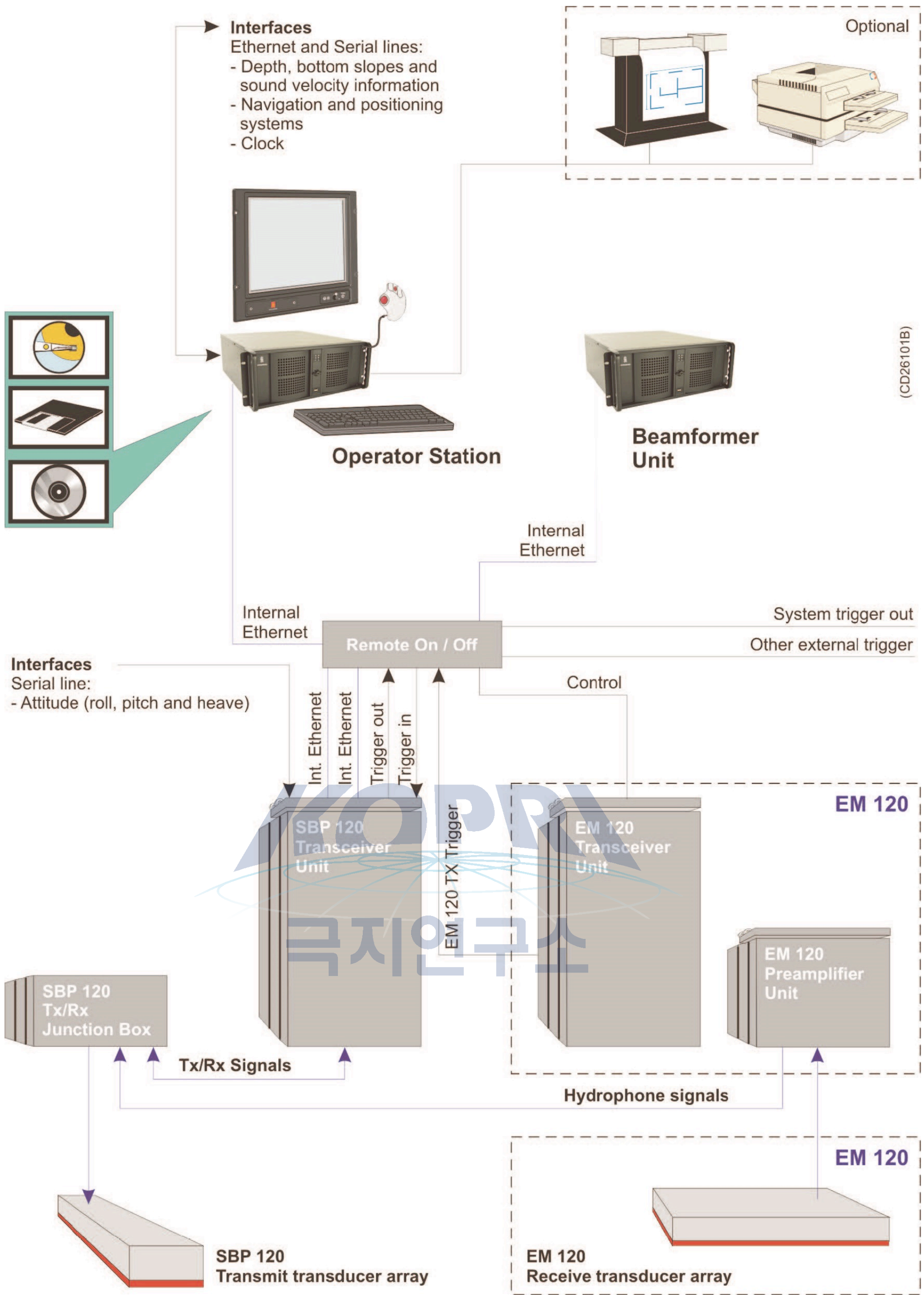

Figure 3.3. SBP120 system units and interfaces.

3.3. Results

During the expedition ARA07C, we collected Multi-Beam (1800 nautical mile) and SBP (2240 nautical mile) data. We conducted a line survey after we found an interesting structure in SBP and Multi-Beam screens. The structure is interpreted as a gas-flow structure from SBP data. Also, bathymetry data were collected in this target area. This area has a total of 4 mounds (width 200m, height 10m). We conducted sediment coring at two stations in this area. Sediment coring results are explained in chapter 5.

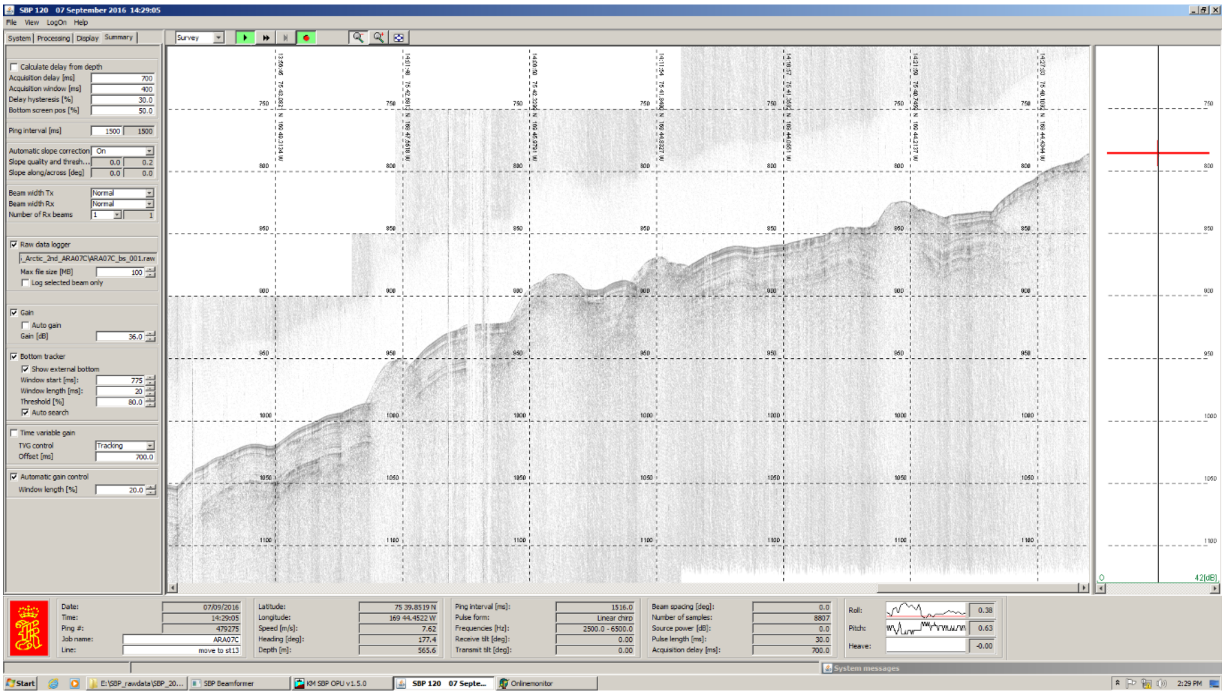

Figure 3.4. SBP image around st13 and st14 with identified gas-flow structure.

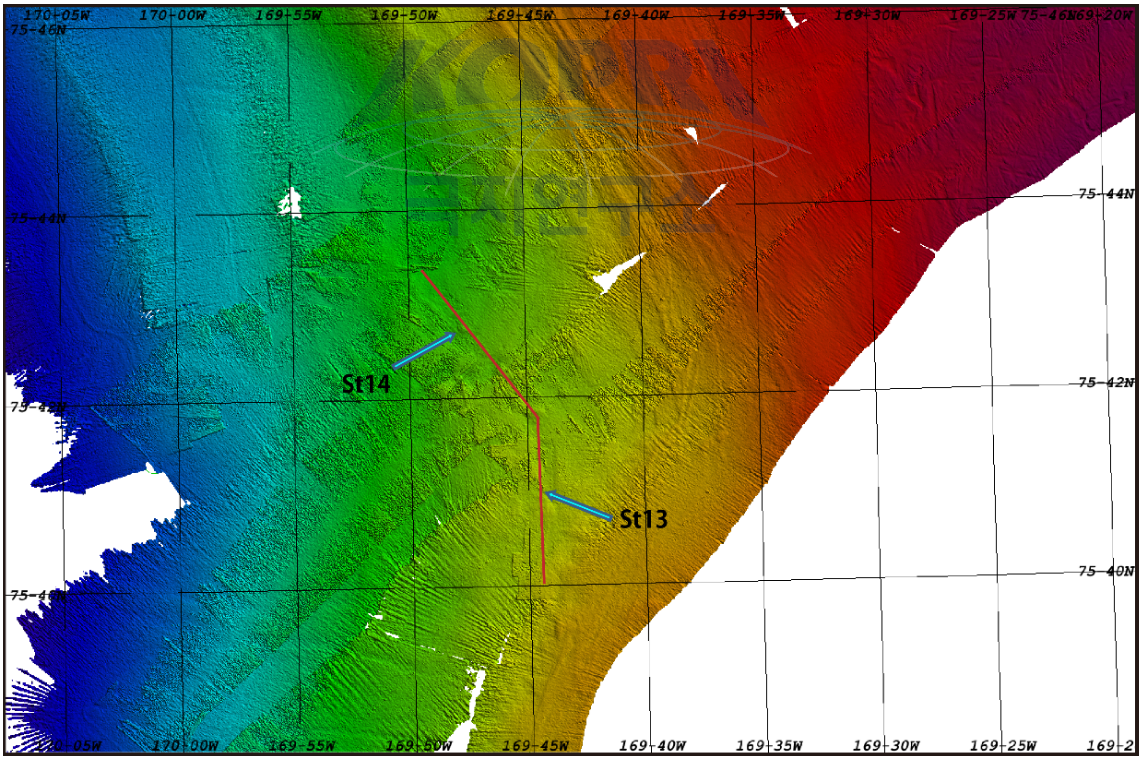

Figure 3.5. Bathymetry around st13 and st14.

Chapter 4. Sparker Multi-Channel Seismic Survey

M.-H. Kang, J.-G. Choi and S. Chae

4.1. Introduction

To better understand the shallow subsurface structure of the East Siberian Shelf in the Arctic Ocean, multi-channel 2D high-resolution seismic survey was carried out during the ARA07C cruise using one digital streamer and single sparker source. IBRV Araon towed a 16 channels Geometrics GeoEEL digital streamer at a water depth of approximately 1 m. The streamer was towed at an offset of 2.3 m to starboard of the vessel centerline. The sparker electrode source with an energy of 5,000 Joules was towed with 2.3 m offset to port of the ship's center line. Source and the front-end of the streamer offset (30 m) was measured at the start of the survey and applied for the rest of the survey. For accurate positioning of streamer and source, AD Navigation's DC201B GPS/GLONASS receiver was installed near the stern of vessel where streamer and source were towed from. Sparker seismic survey can obtain higher resolution subsurface images than air-gun seismic survey because the main frequencies of sparker source range from 100 Hz to 1,000 Hz (cf. the main frequencies of marine air-gun source are 5 Hz - 100 Hz). During the ARA07C cruise, a total of 180 L-km high resolution sparker seismic data was collected with three sequence lines (Figure 4.1).

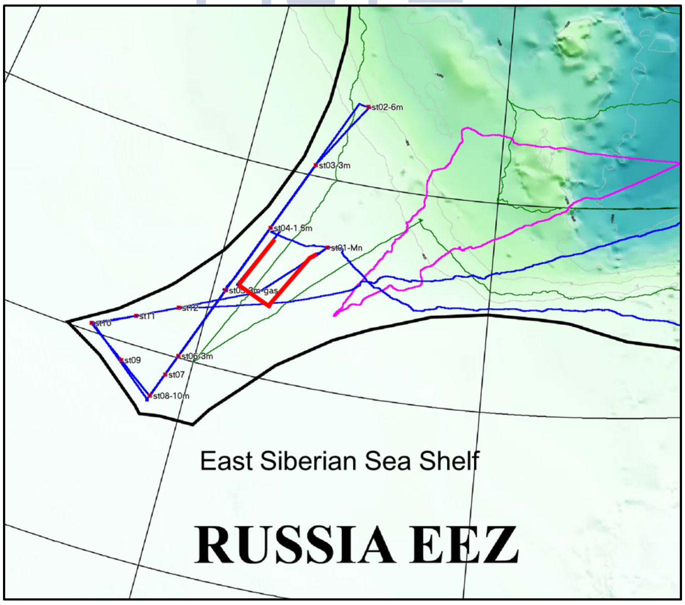

Figure 4.1. Sparker seismic tracks acquired in ARA07C cruise. Red and blue lines represent sparker seismic and ship's tracks of ARA07C cruise, respectively.

4.2. Sparker Seismic System and Operation

The sparker seismic system used during the ARA07 cruise consisted of a sparker generator with an electrode source, a portable digital multi-channel seismic recording system with solid type 16 channels digital streamer, and AD Navigation's DC201B GPS/GLONASS receiver for positioning of streamer and source (Figure 4.2). SIG L5 sparker source with an electrode model EDL 1020 was used during the survey. The electrode model EDL 1020, which can generate up to 6,000 Joules of energy, was towed 50 m behind the stern of the vessel with an offset of 2.3 m to port. Geometrics CNT-2 marine controller and GeoEEL streamer were used for recording of seismic data. Solid type GeoEEL streamer consisted of 16 channels with 3.125 group interval. A 16 channels GeoEEL streamer was towed with an offset of 2.3 m to starboard (Figure 4.3). The measured inline offset between the sparker electrode source and the front-end of the streamer was 30 m. The CNT-2 marine controller provided tools for setup of GeoEEL streamer and various quality controls such as shot, noise, and frequency monitoring views during the data acquisition (Figure 4.4).

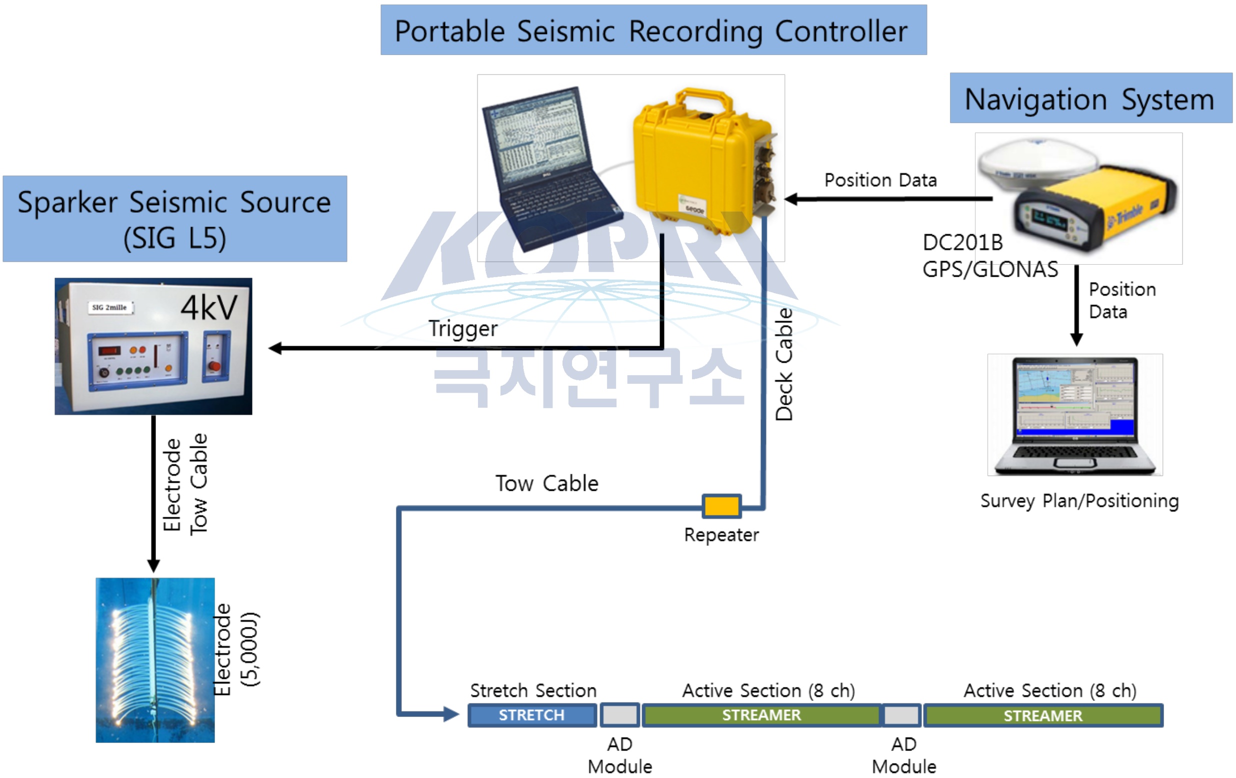

Figure 4.2. Configuration of sparker high-resolution seismic system used in ARA07C cruise.

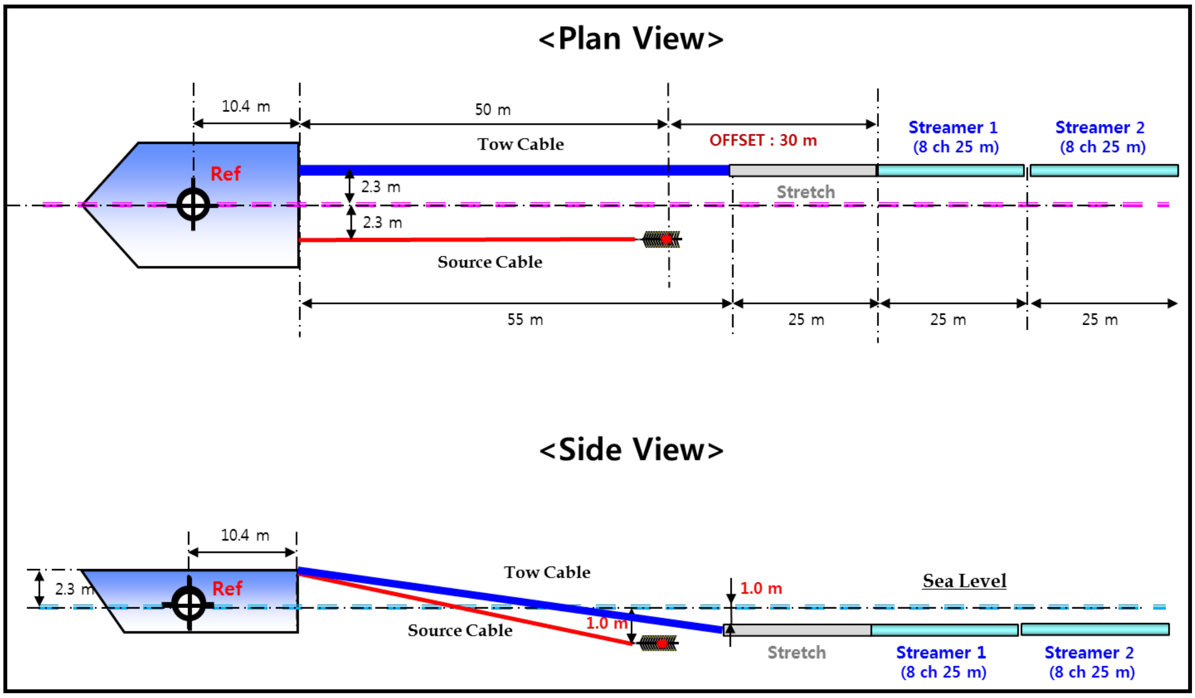

Figure 4.3. General layout and towing diagram of streamer and sparker electrode source used in the sparker seismic survey during ARA07C cruise.

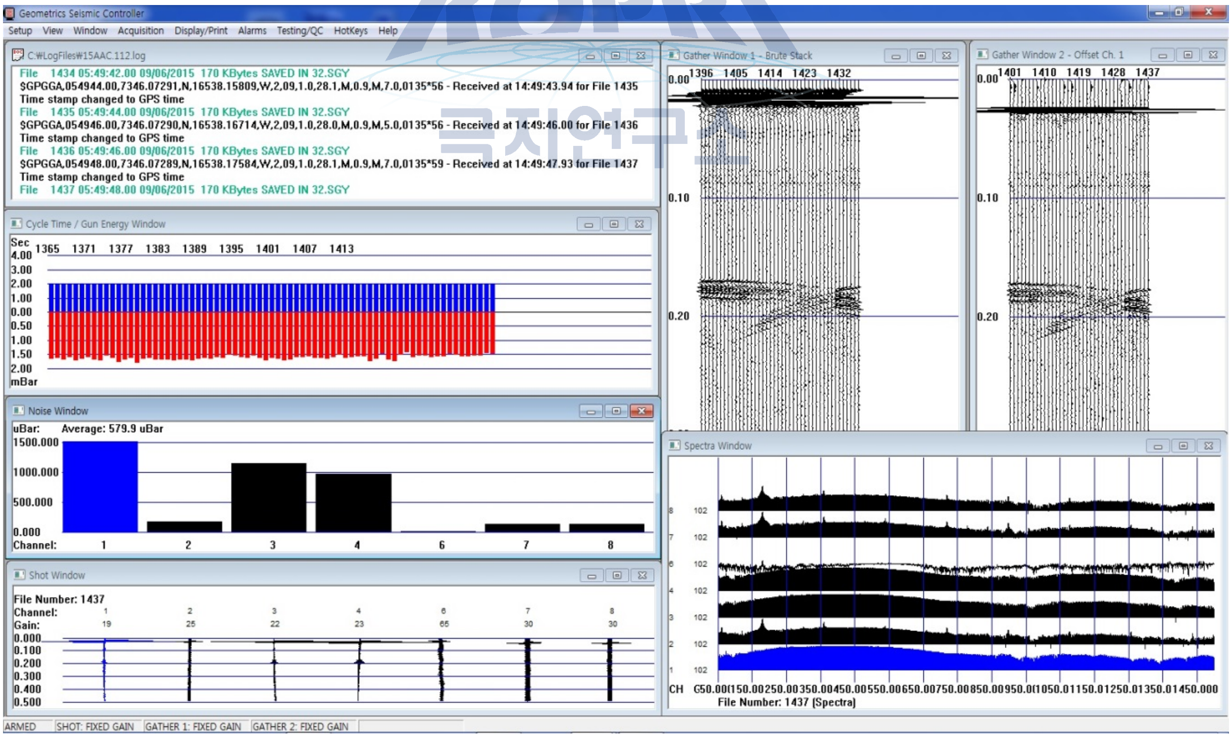

Figure 4.4. Geometrics CNT-2 seismic recording controller provides QC tools including brute stack and single-trace gather during acquisition.

The acquired seismic data were stored in HDD media with SEG-D format, and single trace gather and brute stack were also generated in SEG-Y format during acquisition. Positioning data were recorded in the header of SEG-Y with arc second unit. The sample interval and recording length were 0.125 ms and 1.0 sec, respectively. During the seismic survey, the ship's speed was maintained at 4.5-5.0 knots and the shot interval was 3.0 s. The acquisition parameters used in this cruise are summarized in Table 4.1.

Table 4.1. Acquisition parameters for 2D high resolution sparker seismic survey.

General Information	
Vessel(s):	IBRV ARAON
Job number:	ARA07C
Location:	East Siberian Sea Shelf, Arctic Ocean
Type of Survey: (2D or 3D)	2D
Area, or total kms:	180 L-km
Streamer Parameters	
Type of streamer	Geometrics GeoEEL Solid
Number of streamers	1
Streamer separation	N/A
Streamer length (each nominal)	25 m
No. of channels (per streamer)	16
Group interval	3.125 m
Offset (Centre source to near trace)	30 m
Streamer depth	~1 m
Recording Parameters	
Instrument type	Geometrics CNT-2
Record length	1 s
Sample rate	0.125 ms
Recording filter: Hi-cut	N/A
Recording filter: Lo-cut	30 Hz
Tape format	SEG-D
Source Parameters	
Source type	SIG L5 Sparker / ELP 1250
Number of sources	1
Source separation	N/A
Volume per source	5,000 Joules
Source depth	1 m
Shot point interval per shot	3 sec (time shooting)

4.3. Results

During the cruise a total of ~180 L-km 2D high-resolution sparker seismic reflection data were collected through three sequence lines (Table 4.2.). Raw seismic data will be processed in KIGAM with general processing procedures. Brute stack and single-trace gather were generated at the end of each line in SEG-Y format. Band pass filter of 30-60-600-650 Hz and AGC with a window length of 16 ms were applied to the outputs (Figure 4.5).

Table 4.2. Summary of Sparker seismic data acquisition during ARA07C cruise.

Prefix	Name	Seq	Dir	Sample Rate (ms)	Recording Length	FSP	LSP	Sparker Energy	Distance (km)
16AAC	101	001	205°	0.125 ms	1.0 s	1001	9976	5000J	60
16AAC	102	002	110°	0.125 ms	1.0 s	1080	6219	5000J	40
16AAC	103	003	027°	0.125 ms	1.0 s	1006	10273	5000J	80

Figure 4.5. Brute stack of 16AAC-101 line. Some paleo-channel features are observed, but strong water-bottom multiples are dominant especially in shallow part.

Chapter 5. Sediment Coring

J.-H. Kim, C.M. You, Y. M. Lee, D.-H. Lee, B. Lee., H. Moon, and Y.-G. Kim

5.1. Introduction

Continental shelf/slope settings are highly productive areas and represent ca. 80% of the total carbon accumulation in the ocean. Although Arctic Ocean is only 1% of the total Earth ocean volume, discrete high porosity and permeable lithologies possibly lead to extensive methane (CH_4) venting from the sedimentary environment (Collett, 2009), making the Arctic Ocean a key region for CH_4 cycle study and research on the role of CH_4 in the global climate change. Past studies on climate change in the Arctic tended to assume that land interface is the predominant CH_4 source to the atmosphere (Frey and Smith, 2005). However, with the Arctic region (e.g. East Siberia Sea) indicating active CH_4 venting from sediment to water column (Shakhova et al., 2010), there is a need to evaluate the contribution of Arctic Ocean sediment CH_4 flux to the water column.

It is essential to know the chemical zones with the redox zone to know the carbon cycle, including the methane cycle. Redox zones in natural systems are dictated by metabolic reactions, which are controlled by a myriad of biogeochemical processes. Canfield and Thamdrup (2009) propose a revised the scheme for classifying metabolic zones in marine sediments to be based on the depth distribution of common electron acceptors and the associated chemical zonations, namely oxic, nitrogenous, manganous, ferruginous, sulfidic and methanogenic (Figure 5.1). In the natural marine systems, many biogeochemical and inorganic geochemical reactions have been documented with these chemical zones (Figure 5.1).

In the marine sediment column, sulfate from overlying seawater or from the re-oxidation of sulfides is a key electron acceptor in the upper tens of meters in the sedimentary environment, involves two chemical reactions, namely, particular organic carbon sulfate reduction (POCSR) and anaerobic oxidation of methane (AOM). AOM in marine sediments occur around the sulfate-methane transition zone (SMTZ) is an effective microbial filter that prevents methane from leaking into the water column and potentially the atmosphere (Barnes and Goldberg, 1976; Heeschen et al., 2005; Reeburgh, 2007; Regnier et al., 2011), which is critical to assessing the role of deep-subseafloor methane on the carbon cycle. However, to date, it has been rarely illustrated the pore fluid/gas chemistry, and biogeochemistry from water column to sediment column of the Arctic Sea area for understanding the carbon cycle. During ARA07C Expedition, based on geological, geochemical and biogeochemical data from sediments, seawater, pore fluid and gas, we aimed to uncover 1) the behavior and source of pore fluid and gas properties, 2) the microbial distribution and ecology with metabolic pathway, and 3) the microbial roles controlling CH_4, within the sediment column in the Arctic Sea area.

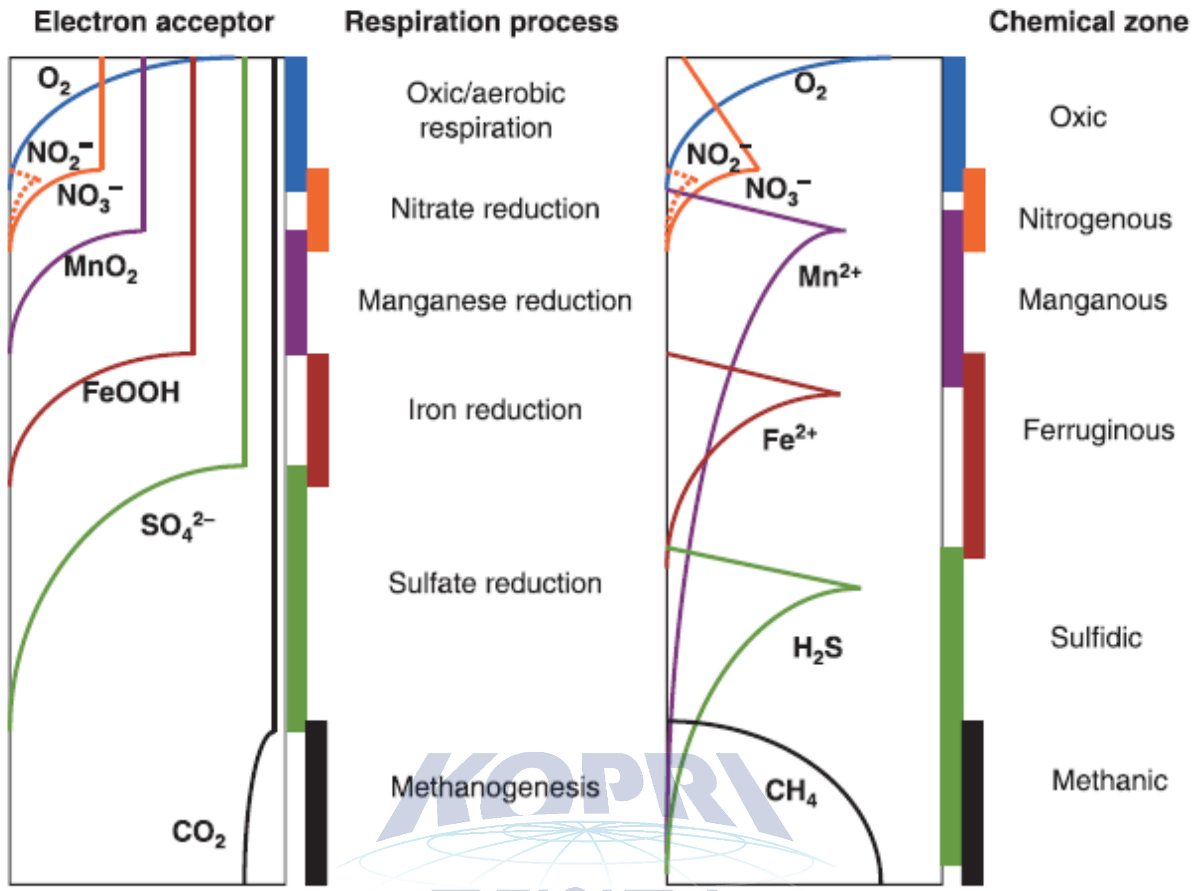

Figure 5.1. Schematic diagram showing the distribution of common electron acceptors, respiration process, and chemical zone with depth in the natural environment system (from Canfield and Thamdrup, 2009).

Together with geochemical approaches to reveal methane source, pathway, and microbial facies, we also tried to know the geophysical properties, i.e., thermal and mechanical state, of shallow sediments during the expedition. Subsea permafrost thawing due to long-term ocean warming and flooding since the Last Glacial Maximum is considered to have promoted significant release of methane from sediments to sea water in the Arctic shelf (Paull et al., 2011; Ruppel, 2014). In the East Siberian shelf, except for models, distribution of subsea permafrost, as well as its effect on soil strength, are still poorly known (e.g., Romanovskii and Hubberten, 2001). During the expedition, we collected in-situ geothermal gradient, and thermal conductivity and shear stress of retrieved cores using brand new instruments to offer the benefit of time efficiency, when comparing with those used in the ARA04C and ARA05C expeditions (Jin et al, 2015, Jin and Dallimore, 2016).

5.2. Methods

5.2.1. Coring

Two types of core, gravity corer (GC) and box corer (BC), were used to collect marine sediment during this expedition (Figure 5.2). Seven GCs and eight BCs were sampled and their information was summarized in Table 5.1. The location map of coring sites is illustrated in Figure 5.3.

(A) (B)

Figure 5.2. Sediment coring by A) gravity corer (GC) and B) box corer.

At all core sites a CTD was performed before GC/BC coring. At Site ARA07C BC01, trawling and dredge were performed after BC coring in order to find the manganese nodules. GC cores were split into two parts with 1-1.5 m section lengths onboard. Half of the core was used for working (sampling) and the other was stored as archived core (Figure 5.4). Core photos were taken by IR-Trax using the archived core. Magnetic susceptibility (MS) was also measured by this instrument. Sediment subsamples for the mineralogy, geochemistry, biogeochemistry, and microbiology were collected at the working core with approximately 10 cm intervals. Authigenic carbonates were collected by handpicking from the working core. Sediments samples were also collected from BC for biogeochemistry, microorganism and mineral research for post-cruise analyses.

Table 5.1. Summarized the information of core sites from ARA07C Expedition.

	Station No	Lat. (°)	Long. (°)	Water Depth(m)	Core Type	Remark
ARA07C BC01	1	75.3563 N	173.7641 E	185	BC	Trawling and dredge
ARA07C BC02	2	76.7476 N	174.2610 E	700	BC	
ARA07C GC02		76.7476 N	174.2610 E	700	GC	
ARA07C GC02-1		76.7463 N	174.3212 E	700	GC	
ARA07C BC03	3	76.1074 N	172.6549 E	270	BC	
ARA07C GC03		76.1074 N	172.6549 E	270	GC	
ARA07C BC04	4	75.4232 N	171.4952 E	150	BC	
ARA07C BC05	5	74.7441 N	170.4551 E	60	BC	
ARA07C GC05		74.7441 N	170.4551 E	60	GC	
ARA07C BC06	6	74.0192 N	169.4483 E	45	BC	
ARA07C BC07	7	73.8151 N	169.1941 E	45	BC	
ARA07C GC07		73.8151 N	169.1941 E	45	GC	
ARA07C BC13	13	75.6800 N	169.7365 W	610	BC	Gas hydrae/ authigenic carbonate found
ARA07C GC13		75.6800 N	169.7365 W	610	GC	
ARA07C GC14	14	75.7034 N	169.7592 W	653	GC	authigenic carbonate found

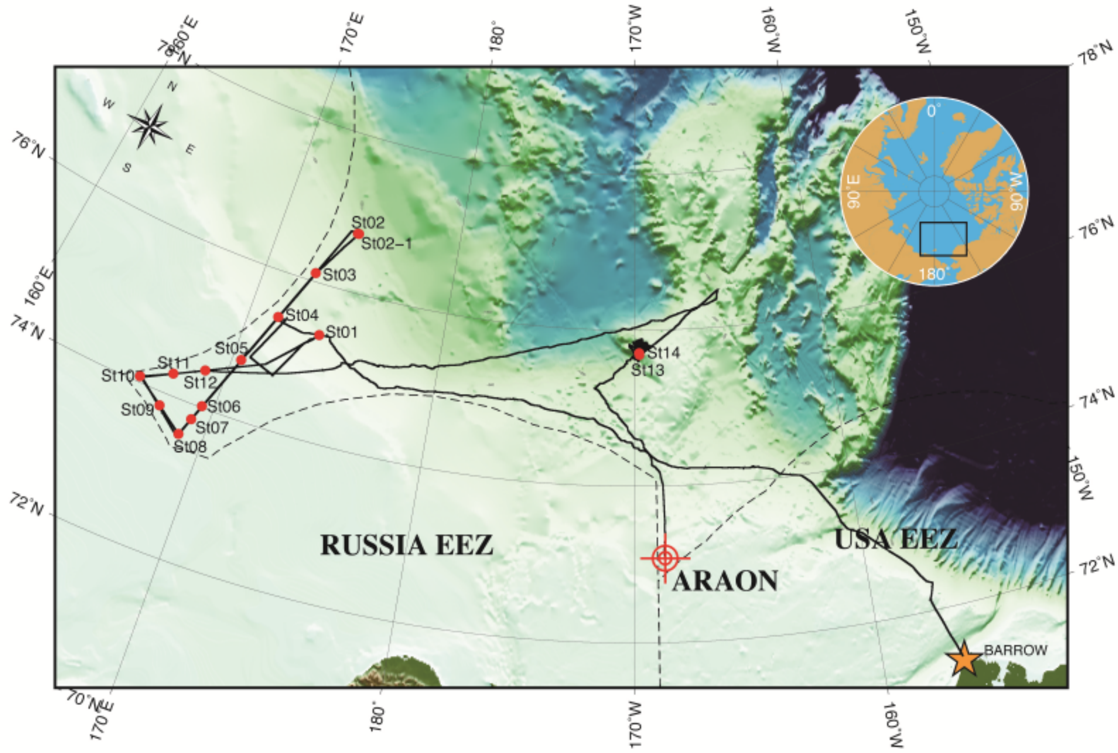

Figure 5.3. Location map of core sites.

(A) (B)

Figure 5.4. Sediment sampling at A) GC and B) box core.

5.2.2. Pore fluid chemistry

Pore fluid in the core was extracted by Rhizone (Figure 5.5). The sampling interval of pore fluid was every 20-30 cm at gravity core while it was 2 cm at box core. Seawater was also collected by Niskin bottles attached to the CTD at each core site. Since pore fluid was extracted very slowly by Rhizone; extraction was performed about 8~10 h at room temperature. Extracted pore fluid was collected in 25 ml acid-prewashed syringes and filtered by in-line 0.2 -μm disposable polytetrafluoroethylene filter. Pore-fluid aliquots were transferred into HClprewashed high density polyethylene (HDPE) bottles (~3-5 ml) for shipboard analyses, and for major and minor ions (~3-5 ml) and dissolved organic matter (DOM; ~2-4 ml) to be carried out post cruise. Additional subsamples were collected in 2 ml septum screw-lid glass vials for characterization of the δD and $\delta^{18}O$, and of $\delta^{13}C$ during the post cruise.

(A) (B)

Figure 5.5. Extraction of pore fluid from A) gravity core (GC) and B) box core by Rhizone.

Samples for major and minor ions were acidified with 20 μl ultrapure grade HNO_3 and samples for DIC were treated with 50 μl $HgCl_2$ at room temperature. Pore fluid samples were routinely analyzed for refractive index with Fisher hand-held portable refractometer immediately after pore fluid extraction. The refractive index was converted to salinity based on repeated analyses of International Association of Physical Sciences of the Oceans (IAPSO) standard seawater. Salinity has been determined by Reflectometer, and chlorinity (Cl^-) and alkalinity have been analyzed by titration using $AgNO_3$ and 0.1N HCl, respectively, on board. The reproducibility of alkalinity and Cl^- titrations was monitored through repeated analysis of IAPSO standard seawater, and was < 2% and < 0.5%, respectively. Pore fluid samples for shipboard analyses, major and minor ions and isotope compositions were stored at about 4 ^{o}C in a refrigerator while DOM samples were stored in the freezer.

5.2.3. Gas chemistry

Bulk sediments (3 mL) were sampled from the open core taken every ~1.5 m interval for analysis of dissolved gas (headspace gas, HS) using the headspace-technique with a 5 mL cut-off plastic syringe. The sediments were extruded into 20 mL headspace glass vials filled with 2 mL of saturated NaCl solution, and then the vials were immediately capped with rubber septa and sealed with aluminum crimp caps. We have prepared two HS samples; one is for the gas composition and the other is for the gas isotope ($\delta^{13}C_{CH4}$, δD_{CH4}, $\delta^{13}C_{CO2}$, etc).

Voids within the core liner, which formed from gas expansion during core retrieval, were sampled immediately upon recovery using a syringe attached to a hollow stainless-steel tool that punctures the core liner. The gas samples, denoted as VG, were then transferred to 50 mL glass vials that had been pre-filled with saturated NaCl solution.

Small pieces of solid gas hydrate were placed into 60 mL syringes, where they were allowed to dissociate (BG). The BG was preserved followed the aforementioned protocols for VG samples.

5.2.4. Biomarkers

ARA07C Expedition had partially performed for the sampling of biomarker analysis along the continental shelf/slope of the East Siberia Sea to reveal geological and geochemical characterizations associated with CH_4 generation. To demonstrate the geochemical signature associated with methane-related microbial communities in these sediments, we used the BC and GC sediments. Especially, molecular signatures, such as microbial lipid have been used as proxy to identify specific microorganisms involved in the CH_4 cycle to reveal microbial ecological relationships and their metabolic potential in the context of the specific environments created by active CH_4 venting.

The core sediments were collected from our study sites during the expedition from August 2016 to September 2016 (Table 5.2). In particular, the presence of gas hydrate was partially observed at the hydrate-bearing intervals (bottom layer; ca. 247 cm) in the ARA07C GC13. When split, the divided core partially exhibited a crack-like structure created through degassing and a strong sulfide odor in the core sediments (ARA07CGC13 and GC14). The sediment BC samples were collected every 1 cm and GC samples of our study sites were collected every 10-15 cm interval. All sediment samples were kept frozen at -20 °C before organic geochemical analysis. Furthermore, the ARA07C Expedition discovered authentic carbonate samples in the ARA07C GC13 and GC4. These carbonates were sampled at two sites and kept frozen at -20 °C. To understand the variation of methane-related microbial communities in the sedimentary environment, specific organic compounds (hydrocarbon, alcohol and fatty acids) including their carbon isotopic values ($\delta^{13}C$) will be analyzed by the Hanyang University, Korea.

5.2.5. Microorganism

Sediments samples from GC and BC were collected in 2 cm to 15 cm intervals. The samples were preserved at -80°C for microbial community analysis and for cultivation of methangenic or methanotrophic archaea and sulfate-reducing bacteria. These samples (~0.3g) were preserved at -80°C in 20% glycerol. To isolate the methane cycle-related bacteria and archaea, ~0.3g of gas hydrate-bearing sediments were suspended in 2 ml of 0.85% NaCl, inoculated in MM media, and cultivated at 4°C. To investigate the impact of the temperature on the methane production and oxidation, 1.5 ml of sediment samples from the surface, sulfate-reduction zone, and gas hydrate of ARA07C 13C with 50 ml of 0.2 μm-membrane filtered sea water were suspended in 50 ml serum bottles in triplicate and cultivated at 4 and 10°C, respectively. For gas analysis of these samples, 1 mL gas from headspace of each serum bottles were ejected and stored in 2 mL serum bottle at 4°C.

Table 5. 2. List of samples collected from the ARA07C Expedition using GC and BC.

Core ID	Core Type	Sample No.	Depth (cm)
ARA07C BC_ST-01	BC	ARA07C-BC01-01	1
		ARA07C-BC01-02	3
		ARA07C-BC01-03	5
		ARA07C-BC01-04	7
		ARA07C-BC01-05	9

		ARA07C-BC01-06	11
		ARA07C-BC01-07	13
		ARA07C-BC01-08	15
		ARA07C-BC01-09	17
		ARA07C-BC01-10	19
		ARA07C-BC01-11	21
		ARA07C-BC01-12	23
		ARA07C-BC01-13	25
ARA07C BC_ST-02B	BC	ARA07C-BC-St02-01	0
		ARA07C-BC-St02-02	2
		ARA07C-BC-St02-03	4
		ARA07C-BC-St02-04	6
		ARA07C-BC-St02-05	8
		ARA07C-BC-St02-06	10
		ARA07C-BC-St02-07	12
		ARA07C-BC-St02-08	14
		ARA07C-BC-St02-09	16
		ARA07C-BC-St02-10	18
		ARA07C-BC-St02-11	20
		ARA07C-BC-St02-12	22
		ARA07C-BC-St02-13	24
		ARA07C-BC-St02-14	26
		ARA07C-BC-St02-15	28
		ARA07C-BC-St02-16	30
		ARA07C-BC-St02-17	32
		ARA07C-BC-St02-18	34
ARA07C BC_ST-03	BC	ARA07C-BC-St03-01	0
		ARA07C-BC-St03-02	2
		ARA07C-BC-St03-03	4
		ARA07C-BC-St03-04	6
		ARA07C-BC-St03-05	8
		ARA07C-BC-St03-06	10
		ARA07C-BC-St03-07	12
		ARA07C-BC-St03-08	14
		ARA07C-BC-St03-09	16
		ARA07C-BC-St03-10	18
		ARA07C-BC-St03-11	20
		ARA07C-BC-St03-12	22
		ARA07C-BC-St03-13	24

		ARA07C-BC-St03-14	26
		ARA07C-BC-St03-15	28
		ARA07C-BC-St03-16	30
		ARA07C-BC-St03-17	32
		ARA07C-BC-St04-01	0
		ARA07C-BC-St04-02	2
		ARA07C-BC-St04-03	4
		ARA07C-BC-St04-04	6
		ARA07C-BC-St04-05	8
ARA07C BC_ST-04	BC	ARA07C-BC-St04-06	10
		ARA07C-BC-St04-07	12
		ARA07C-BC-St04-08	14
		ARA07C-BC-St04-09	16
		ARA07C-BC-St04-10	18
		ARA07C-BC-St04-11	20
		ARA07C-BC-St04-12	22
		ARA07C-BC-St05-01	0
		ARA07C-BC-St05-02	2
		ARA07C-BC-St05-03	4
		ARA07C-BC-St05-04	6
		ARA07C-BC-St05-05	8
		ARA07C-BC-St05-06	10
ARA07C BC_ST-05	BC	ARA07C-BC-St05-07	12
		ARA07C-BC-St05-08	14
		ARA07C-BC-St05-09	16
		ARA07C-BC-St05-10	18
		ARA07C-BC-St05-11	20
		ARA07C-BC-St05-12	22
		ARA07C-BC-St05-13	24
		ARA07C-BC-St07-01	0
		ARA07C-BC-St07-02	2
		ARA07C-BC-St07-03	4
		ARA07C-BC-St07-04	6
ARA07C BC_ST-07	BC	ARA07C-BC-St07-05	8
		ARA07C-BC-St07-06	10
		ARA07C-BC-St07-07	12
		ARA07C-BC-St07-08	14
		ARA07C-BC-St07-09	16
		ARA07C-BC-St07-10	18

		ARA07C-BC-St07-11	20
		ARA07C-BC-St07-12	22
		ARA07C-BC-St07-13	24
		ARA07C-BC-St07-14	26
		ARA07C-BC-St07-15	28
		ARA07C-BC-St07-16	30
		ARA07C-BC-St07-17	32
ARA07C BC_ST-13	BC	ARA07C-BC-St13-01	0
		ARA07C-BC-St13-02	2
		ARA07C-BC-St13-03	4
		ARA07C-BC-St13-04	6
		ARA07C-BC-St13-05	8
		ARA07C-BC-St13-06	10
		ARA07C-BC-St13-07	12
		ARA07C-BC-St13-08	14
		ARA07C-BC-St13-09	16
		ARA07C-BC-St13-10	18
		ARA07C-BC-St13-11	20
		ARA07C-BC-St13-12	22
		ARA07C-BC-St13-13	24
		ARA07C-BC-St13-14	26
		ARA07C-BC-St13-15	28
		ARA07C-BC-St13-16	30
ARA07C GC_ST-02B	GC	ARA07C GC_ST-02B_1_1	3
		ARA07C GC_ST-02B_1_2	13
		ARA07C GC_ST-02B_1_3	23
		ARA07C GC_ST-02B_1_4	28
		ARA07C GC_ST-02B_1_5	33
		ARA07C GC_ST-02B_1_6	43
		ARA07C GC_ST-02B_1_7	53
		ARA07C GC_ST-02B_2_8	65
		ARA07C GC_ST-02B_2_9	72
		ARA07C GC_ST-02B_2_10	82
		ARA07C GC_ST-02B_2_11	92
		ARA07C GC_ST-02B_2_12	102
		ARA07C GC_ST-02B_2_13	112
		ARA07C GC_ST-02B_2_14	122
		ARA07C GC_ST-02B_2_15	132
		ARA07C GC_ST-02B_2_16	142

		ARA07C GC_ST-02B_2_17	152
		ARA07C GC_ST-02B_2_18	162
		ARA07C GC_ST-02B_2_19	172
		ARA07C GC_ST-02B_2_20	182
		ARA07C GC_ST-02B_2_21	192
		ARA07C GC_ST-02B_2_22	202
		ARA07C GC_ST-02B_3_23	211
		ARA07C GC_ST-02B_3_24	221
		ARA07C GC_ST-02B_3_25	231
		ARA07C GC_ST-02B_3_26	241
		ARA07C GC_ST-02B_3_27	251
		ARA07C GC_ST-02B_3_28	261
		ARA07C GC_ST-02B_3_29	271
		ARA07C GC_ST-02B_3_30	281
		ARA07C GC_ST-02B_3_31	291
		ARA07C GC_ST-02B_3_32	301
		ARA07C GC_ST-02B_3_33	311
		ARA07C GC_ST-02B_3_34	321
		ARA07C GC_ST-02B_3_35	336
ARA07C GC_ST-03	GC	ARA07C GC_ST-03_1_1	6
		ARA07C GC_ST-03_1_2	16
		ARA07C GC_ST-03_1_3	26
		ARA07C GC_ST-03_1_4	29
		ARA07C GC_ST-03_1_5	36
		ARA07C GC_ST-03_1_6	41
		ARA07C GC_ST-03_1_7	56
		ARA07C GC_ST-03_1_8	66
		ARA07C GC_ST-03_1_9	76
		ARA07C GC_ST-03_1_10	86
		ARA07C GC_ST-03_2_11	93
		ARA07C GC_ST-03_2_12	108
		ARA07C GC_ST-03_2_13	121
		ARA07C GC_ST-03_2_14	131
		ARA07C GC_ST-03_2_15	139
		ARA07C GC_ST-03_2_16	151
		ARA07C GC_ST-03_2_17	161
		ARA07C GC_ST-03_2_18	168
		ARA07C GC_ST-03_2_19	181
		ARA07C GC_ST-03_2_20	191

		ARA07C GC_ST-03_2_21	199
		ARA07C GC_ST-03_2_22	211
		ARA07C GC_ST-03_2_23	221
		ARA07C GC_ST-03_2_24	231
		ARA07C GC_ST-03_3_25	244
		ARA07C GC_ST-03_3_26	251
		ARA07C GC_ST-03_3_27	261
		ARA07C GC_ST-03_3_28	271
		ARA07C GC_ST-03_3_29	279
		ARA07C GC_ST-03_3_30	291
		ARA07C GC_ST-03_3_31	301
		ARA07C GC_ST-03_3_32	311
		ARA07C GC_ST-03_3_33	323
		ARA07C GC_ST-03_3_34	331
		ARA07C GC_ST-03_3_35	341
		ARA07C GC_ST-03_3_36	351
		ARA07C GC_ST-03_3_37	359
		ARA07C GC_ST-03_3_38	371
ARA07C GC_ST-05	GC	ARA07C GC_ST-05_1_1	2.5
		ARA07C GC_ST-05_1_2	7.5
		ARA07C GC_ST-05_1_3	17.5
		ARA07C GC_ST-05_1_4	27.5
		ARA07C GC_ST-05_1_5	37.5
		ARA07C GC_ST-05_1_6	47.5
		ARA07C GC_ST-05_1_7	57.5
		ARA07C GC_ST-05_1_8	67.5
		ARA07C GC_ST-05_1_9	77.5
		ARA07C GC_ST-05_1_10	92.5
		ARA07C GC_ST-05_1_11	102.5
		ARA07C GC_ST-05_1_12	112.5
		ARA07C GC_ST-05_1_13	122.5
		ARA07C GC_ST-05_1_14	132.5
ARA07C GC_ST-07	GC	ARA07C GC_ST-07_1_1	3.5
		ARA07C GC_ST-07_1_2	13.5
		ARA07C GC_ST-07_1_3	28.5
		ARA07C GC_ST-07_1_4	38.5
		ARA07C GC_ST-07_1_5	48.5
		ARA07C GC_ST-07_1_6	58.5
		ARA07C GC_ST-07_1_7	68.5

		ARA07C GC_ST-07_1_8	78.5
		ARA07C GC_ST-07_1_9	88.5
		ARA07C GC_ST-07_1_10	98.5
		ARA07C GC_ST-07_1_11	108.5
		ARA07C GC_ST-07_1_12	118.5
		ARA07C GC_ST-07_1_13	128.5
ARA07C GC_ST-13	GC	ARA07C GC_ST-13_1_1	0
		ARA07C GC_ST-13_1_2	5
		ARA07C GC_ST-13_1_3	12
		ARA07C GC_ST-13_1_4	17
		ARA07C GC_ST-13_1_5	27
		ARA07C GC_ST-13_1_6	32
		ARA07C GC_ST-13_1_7	42
		ARA07C GC_ST-13_1_8	47
		ARA07C GC_ST-13_1_9	57
		ARA07C GC_ST-13_1_10	62
		ARA07C GC_ST-13_1_11	72
		ARA07C GC_ST-13_1_12	77
		ARA07C GC_ST-13_1_13	87
		ARA07C GC_ST-13_1_14	92
		ARA07C GC_ST-13_1_15	102
		ARA07C GC_ST-13_1_16	110
		ARA07C GC_ST-13_2_17	118
		ARA07C GC_ST-13_2_18	124
		ARA07C GC_ST-13_2_19	132
		ARA07C GC_ST-13_2_20	147
		ARA07C GC_ST-13_2_21	152
		ARA07C GC_ST-13_2_22	162
		ARA07C GC_ST-13_2_23	172
		ARA07C GC_ST-13_2_24	182
		ARA07C GC_ST-13_2_25	192
		ARA07C GC_ST-13_2_26	207
		ARA07C GC_ST-13_2_27	212
		ARA07C GC_ST-13_2_28	222
		ARA07C GC_ST-13_2_29	227
		ARA07C GC_ST-14_1_1	1
		ARA07C GC_ST-14_1_2	11
		ARA07C GC_ST-14_1_3	21
ARA07C GC_ST-14	GC	ARA07C GC_ST-14_1_4	41

	ARA07C GC_ST-14_1_5	61
	ARA07C GC_ST-14_1_6	71
	ARA07C GC_ST-14_1_7	81
	ARA07C GC_ST-14_1_8	101
	ARA07C GC_ST-14_1_9	109
	ARA07C GC_ST-14_1_10	121
	ARA07C GC_ST-14_1_11	131
	ARA07C GC_ST-14_1_12	141
	ARA07C GC_ST-14_1_13	151
	ARA07C GC_ST-14_1_14	156

5.2.6. Heat flow

Marine heat flow is simply determined from two parameters, i.e., geothermal gradient and thermal conductivity. In order to observe these two parameters, we used two different instrument sets: Miniaturized Temperature Logger (MTL) by ANTARES and the DST Tilt by Star-Oddi for in-situ geothermal gradient (Figure 5.6; Tables 5.3. and 5.4), and TK04 by TeKa for thermal conductivity of retrieved sediment cores (Figure 5.7.; Table 5.5). Because in-situ observation results are preferred rather than laboratory observation ones, thermal conductivity values should be corrected using the empirical relationship by Ratcliffe (1960).

(A) (B)

(C)

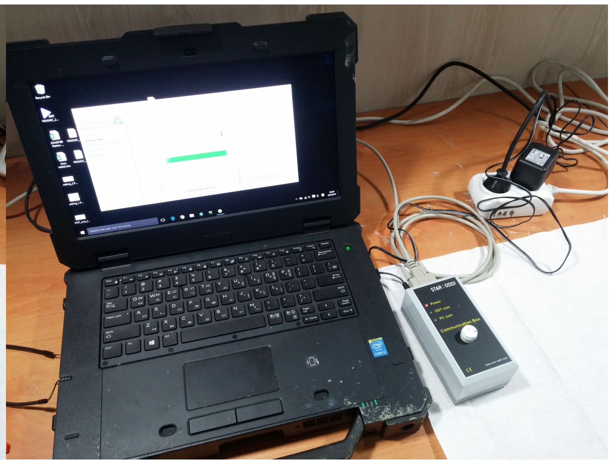

(D)

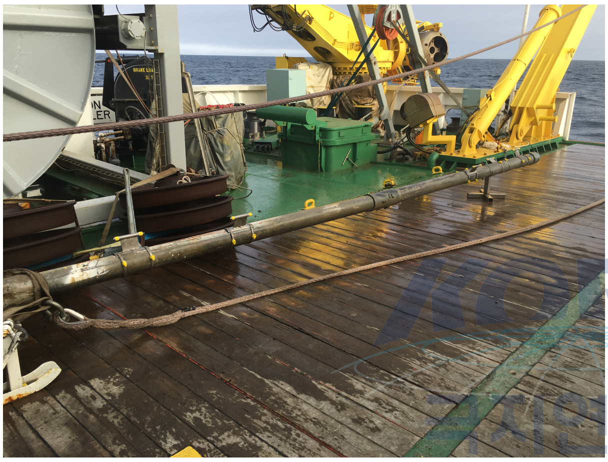

(D)

(F)

Fig 5.6. Photos of the MTL (A) and the DST Tilt (B) with platforms for each (C, D). And photos of gravity core equipped with combination of the two instruments (E, F).

Table 5.3. Specifications of the MTL.

Type	Antares 1854
Length	160 mm
Weight	120 g
Chassis	Stainless steel
Battery	3 VDC type DL1/3N (soldered)
Maximum pressure	60 MPa
Measuring range	-5 to 50°C
Resolution	0.001°C
Accuracy	< ±0.1°C
Maximum operating time per battery	300,000 samples or 1 year standby
Programmable measure intervals	1 sec till 255 min
Starting time	Immediately or programmable with Date and Time up to 30 days in advance
Read-out type	Galvanic coupling (without cable)

Table 5.4. Specifications of the DST Tilt.

Sensors	Tilt (3-D), temperature, pressure (depth)
Size (diameter * length)	15 mm * 46 mm
Weight (in air / in water)	19 g / 12 g
Battery type	4 years for a sampling interval of 10 min
Memory type	Non-volatile EEPROM
Memory capacity / size of one measurement (bytes)	261,564 bytes / temperature-pressure 3bytes, tilt 6 bytes
Data resolution	12 bits
Temperature range	-1 to 40°C
Temperature resolution	0.032°C
Temperature accuracy	±0.1°C
Temperature response time	Time constant (63%) reached in 20 sec
Standard depth/pressure ranges	30, 50, 100, 270, 800, 1500, 2000, 3000 m
Depth/pressure resolution	0.03% of selected range
Depth/pressure accuracy	±0.4% of selected range for 30-270 m ±0.6% of selected range for 800-3000 m
Depth/pressure response time	immediate
Tilt resolution	0.2°
Tilt accuracy	±3°
Tilt range	360°

(A) (B)

Figure 5.7. (A) Thermal conductivity measurement system, TK04 with a needle probe. (B) a needle probe is inserted into the whole-round core along with core's horizontal plane at right angle with the two splitting lines on a liner.

In this expedition, we, for the first time, adopted the MTL and the DST Tilt with the gravity corer, instead of the heat probe (KHF-601), which had been used previously in the ARA04C and ARA05C expedition (Jin et al., 2015; Jin and Dallimore, 2016). The reason for this was that the combination of the MTL and the DST Tilt offer the benefit of time efficiency for setup before the first measurement and maintenance in between measurements: the MTL and the DST Tilt can measure temperature and tilt, respectively, and record the readings into an internal storage. Therefore, the only preparation before the measurement needed is attaching them to the corer with a command of ‘run’ using a non-contact special platform for each (Figure 5.7). Time- and effort-consuming processes such as connecting between thermistors and the logger as well as wrapping all connection lines were not necessary any more. Several MTLs up to seven are placed onto the core barrel with intervals using the MTL supporters, and one DST Tilt with inserted into a housing was attached above the core weight.

We could list up to three drawbacks with using combination of the brand new abovementioned instruments with a gravity corer as opposed to the previously used Ewing-type heat probe: a) the main drawback was that we could not monitor the measurement status during the measurement. The previous heat probe contained an acoustic modem enable broadcasting the status of the logger via a certain frequency receivable with hull-mounted EA600. Practically, such drawback does not matter with ARAON because the EA600 malfunctions in the passive mode hearing acoustic ping due to unknown problems. b) another drawback is losing the chance to measure in-situ thermal conductivity. The heat probe provides the function to generate heat within the sediments, thus we can calculate in-situ thermal conductivity using heat dissipation curve with time if heat is generated with adequate timing, after penetration below the seafloor. The probe had trouble detecting the exact timing of penetration due to inappropriate threshold for internal acceleration sensor. c) The other drawback was restriction of the MTLs’ location on the barrel. Location to attach the MTLs on the core barrel should avoid an interval around a joint of two 3 m-long barrels by at least 1 m, in which the barrel and ship’s stern are rubbed during deployment/recovery of the gravity core. Thus, the MTLs may locate the uppermost and lowermost 2 m-interval in the case of using two 3 m-long barrels (Figure 5.6). Such distribution is not good to detect sinusoidal temperature profile resulted from annual temperature change in the bottom water even though there is.

Thermal conductivity of retrieved cores is measured by the TK04 with a needle probe (Figure 5.7; Table 5.5). Cores were left at least 10 hours in the laboratory before the measurement after on-deck to make them thermally equilibrated with laboratory temperature of ~18°C. To expedite the whole processes with cores, pore fluid is extracted from cores during equilibration time (See Section 5.2.2). Pore fluid extraction can modulate water contents, the most important parameter to control the laboratory thermal conductivity values, but unfortunately we have no choice to change an order of core processing. Rather, horizons for thermal conductivity measurement are chosen to avoid ones for pore fluid extraction by at least 5 cm. The measurement was done at interval of ~20-40 cm. Observed thermal conductivity values are averaged with a harmonic mean method, adequate for horizontally layered sediments, into one representative value for a station.

Table 5.5. Specification of TK04.

Model - High Precision Thermal Conductivity Meter TK04	
Measuring principle	Transient line source (needle probe method)
Standard	ASTM D5334-08
Measuring range	0.1 – 10 W/m/K (probe dependent)
Accuracy	±2% (probe dependent)
Reproducibility	±1.5%
Heater current precision	±0.01%
Duration of 1 measurement	60, 80, 240 s (probe dependent)
Automatic repetitions	Up to 99 (unattended)
Sample size	No upper limit, minimum size probe dependent
Sample temperature	-25 to 50°C, 70°C, 125°C (probe dependent)
Power supply	220, 240V AC (50 Hz); 100/120V AC (60Hz)
Power Consumption	~40W
Size	W 471 * H 160 * D 391 mm
Weight	11.2 kg (measuring unit)
Interface	Serial port (com port) or usb port (usb-to-serial converter included)
Stand VLQ needle probe	
Probe type	Needle probe / lab
Dimension	L 70 mm * Ø 2 mm
Measuring range	0.1-10 W/m/K
Accuracy	±2%
Duration of 1 measurement	80 s
Minimum sample size	(approx.) L 85 mm * Ø 40 mm

5.2.7. Shear strength

The shear strength of material represents the internal resistance per unit area that material can offer to resist failure along any plane inside itself. We used the hand vane tester, FTD 20/5 CN-S by Seiken Inc. with a rectangular vane (Figure 5.8; Table 5.6). Two types proved to be suitable for most of sediments in Okhotsk Sea (e.g., Yamshita et al., 2011). We chose a type of the hand vane tester in consideration of the measuring range and a trend of readings with depth.

After splitting whole-round core, measurements were done on the archive half of the split core. Measuring interval was 10 cm for all core sections. As the vane is rotated, maximum torque gage increases. The gage can read the maximum torque at the moment of failure generation. The maximum torque was converted to the shear stress of the sediments using a simplified calculation for vane test provided from the manufacturer:

Shear strength [N/m^2]: $\tau = M_{max} / [\, (\pi * D^2 * H) / 2 + (\pi * D^3) / 6]$

where M_{max} for the maximum torque measured by the vane shear tester, D and H for diameter and height of the vane (0.01 and 0.02 m, respectively).

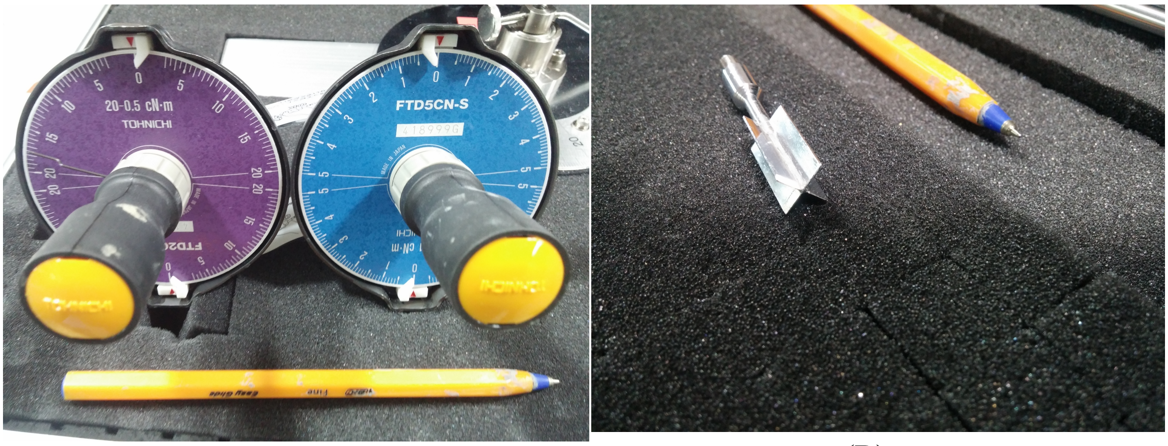

(A) (B)

Figure 5.8. The hand vane testers FTD20/5CN-S consists of two parts, upper gage to measure up to 20/5 cN·m (A) and lower vane with dimension of D 0.01 m and H 0.02 m (B).

Table 5.6. Specification of the hand vane testers.

	Measuring range (cN·m)	Measuring scale (cN·m)	Length	Weight	Maximum shear strength with the vane (N/m^2)
FTD20CN-S	3-20	0.5	152 mm	140 g	8185-54,567
FTD5CN-S	0.5-5	0.1	152 mm	140 g	1364-13,641

5.2.8. ITRAX

The Itrax Corescanner, a product of Cox Analytical System, which was equipped onto the IBRV Araon is a very useful instrument for scientific scanning of split sediment cores, which can provide XRF, X-ray image, optical image, and magnetic susceptibility measurement over a long section up to 1.75 m (Figure 5.9). Its analytical spot/horizon size can be adjustable the centimeter scale down to 0.1 millimeter scale.

During the expedition, optical image and magnetic susceptibility measurements were carried out due to problems in operation. Scanning operation was cued after splitting cores, meaning that operation began in at least 24 hrs after core-on-deck. Optical image was captured with 1 DPI resolution and magnetic susceptibility was measured with 1 cm interval.

Figure 5.9. The Itrax Corescanner (from the homepage of Cox Analytical System).

5.3. Results

5.3.1. Manganese nodule

Manganese nodules, also known as polymetallic nodules, contain precious elements in high contents and are regarded as one of the most important future mineral resources. They can be found throughout the world oceans, but economically feasible deposits show limited distribution: they can be found only in several deep-sea basins such as Clarion-Clipperton Fracture Zone in northeast equatorial Pacific. Manganese nodules are spherical to oblate in shape with concentric internal growth rims. Their size ranges from less than 1 cm in diameter up to 10 cm or more.

The formation of manganese nodules are influenced by various factors including the presence of nuclei, proximity of element sources and sedimentation rates. Among them, the sediment accumulation rate is a critical factor affecting nodule abundance on the seafloor. Areas of low sedimentation rate as deep-sea abyssal plains are favorable for accumulation of nodules. Manganese nodules are thought to form in three ways; hydrogenetically, precipitation directly from sea water, diagenetically, precipitating in sediments on the sea floor, and hydrothermally, precipitating from nearby hydrothermal fluids. Manganese nodules have been reported from dredge samples in 2012 KOPRI Arctic Expedition. To understand the environment and resource potential, we tried to collect manganese nodules using beam trawl and rock dredge (Figure 5.10). Beam trawl is commonly used for collecting biological samples just above the sea floor, but also useful for gathering manganese nodule distributed on the sea floor as well. Rock dredge was undertaken to collect manganese nodules within sea-floor sediments. Both samplings were carried out at St. 1 (75°21.53N, 173°45.71E) over a distance of 1 km in length. After deploying the systems, Araon maintained slow forward speed at around 1 knot. Several pieces of manganese nodules were collected from both instruments. Nodules from beam trawl were 2 to 4 cm long and spherical in shape with rough, brittle surface textures. Those from dredge were smaller from less than 1 cm to 2 cm long with spherical to irregular shape. We will delineate the origin of manganese nodules by optical and geochemical analyses, and find out its environmental meaning in the study area.

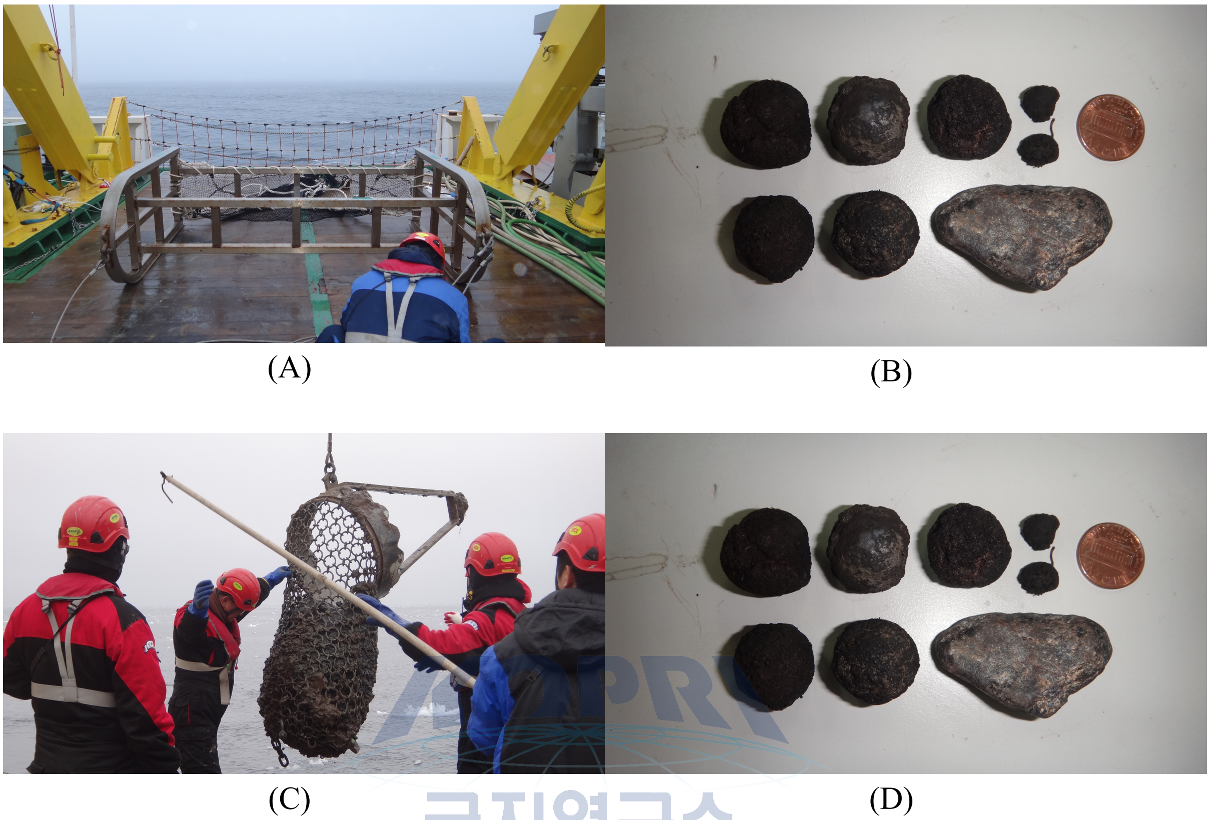

Figure 5.10. Sampling of manganese nodules. A) beam trawl, B) manganese nodule from beam trawl, C) rock dredge, D) manganese nodule from dredge.

5.3.2. Pore fluid chemistry

A total of 91 pore fluid samples (26 samples for 4 box cores and 65 samples from 6 cores) and 34 seawater samples from six cores were collected during the ARA07C Expedition. Samples were analyzed as described in the method section. The data are presented in Figure 5.11, 5.12, and 5.13.

Salinity and chlorinity have the lowest values at the sea surface, and were found to increase with depth until around 200 m at ARA07C Stations 01, 02, 03, and 04, and around 40 m at ARA07C Station 05. At ARA07C Station 07, salinity and chlorinity slightly increased at 10 m and 40 m, respectively, compared with the upper sampling intervals (Figure 5.12). These results may be associated with the mixing of melting water of sea ice and seawater at the upper sampling intervals in all sites. At all the sites, alkalinity in the seawater had a relatively constant value (2.5±0.2 mM; n=33).

Salinity and chlorinity from pore fluids at Sites ARA07C GC02-1, 05, 07, 13, and 14 collected by gravity core show constant values in downcore profile (Figure 5.13). However, chlorinity from pore fluid at Site ARA07C GC03 showed a decreasing trend from 1.06 mbsf (meter below sea floor) to 3.66 mbsf (Figure 5.13), which may be influenced by the freshening water. Gas hydrate was found in situ at the bottom of Site ARA07C GC13 (Figure 5.11). When the freshwater released by hydrate melting was remixed with the remaining reduced volume of pore fluid, freshening occurs, even if the chlorinity of the pore water may have been elevated over that of seawater due to the salt exclusion effect (Hesse, 2003). Recently, chlroinity is enriched in pore fluid where massive gas hydrate was found at the continental margins such as Hydrate Ridge off the coast of Oregon (US), the northern Cascadia margin (Canada) and the Krishna-Godavari Basin (India) (Torres et al., 2011; Kim et al., 2013). Thus, it is expected that salinity and chlorinity in pore fluid should be depleted or enriched at Site ARA07C GC13. However, this behavior was not observed at Site ARA07C GC13.

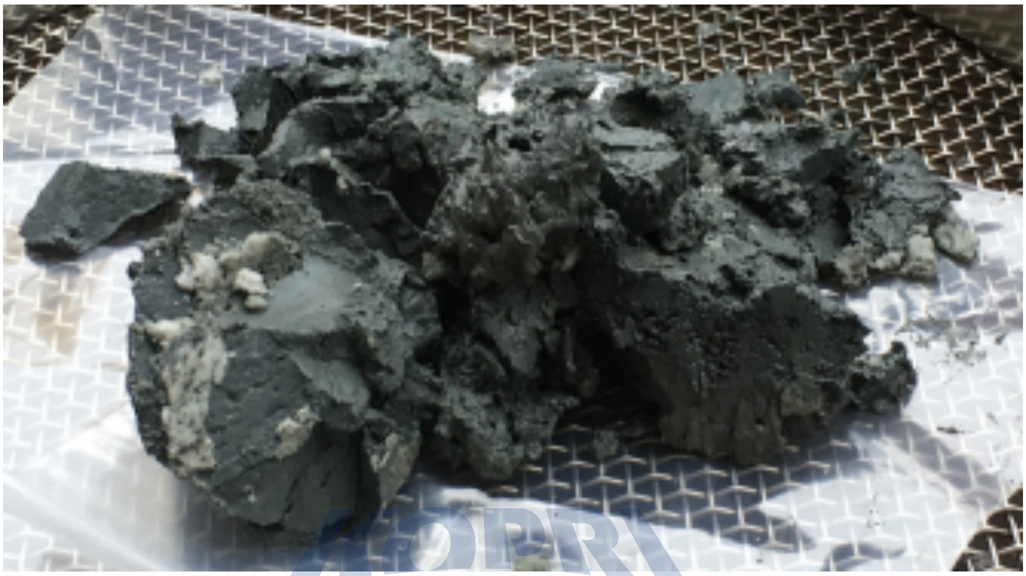

Figure 5.11. Gas hydrate from Site ARA07C GC13.

Figure 5.12. Downcore profile of salinity, Cl^-, and alkalinity of seawater collected from ARA07C A) Station 01 B) Station 02, C) Station 03, D) Station 04, E) Station 05, and F) Station 07.

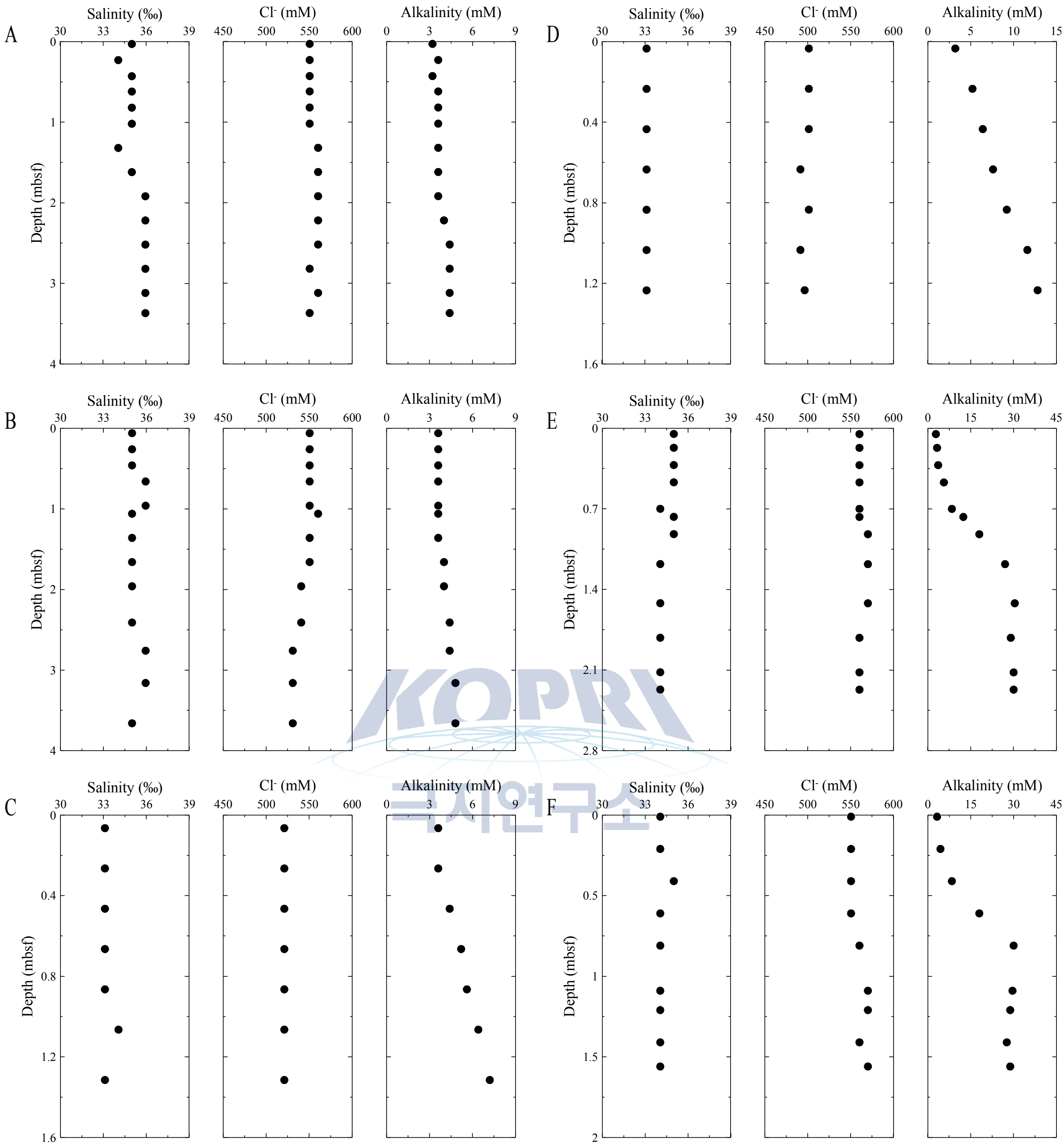

Figure 5.13. Downcore profile of salinity, Cl$^-$, and alkalinity of pore fluid collected from Sites A) ARA07C GC02-1, B) GC03, C) GC05, D) GC07, E) GC13, and F) GC14f

Figure 5.14. Downcore profile of salinity, Cl^-, and alkalinity of pore fluid collected from Sites ARA07C A) BC04, B) BC05, C) BC07 and D) BC13.

Alkalinity of pore fluids from these cores usually increases with depth at all sites. The maximum value was around ~5 mM at Site ARA07C GC02-1 and GC03, around ~8 mM at Site ARA07C GG05, and around ~13 mM at Site ARA07C GC07, while it is around ~30 mM at Sites ARA07C GC13 and 14 (Figure 5.13). The interesting point is that the slope of alkalinity in the downcore profiles is illustrated by three different trends with depth at Sites ARA07C GC13 and 14. The first slope of the alkalinity could be seen from sea surface to ~0.5 mbsf, which slightly increased with depth, and the second slope suddenly increased from ~0. 5 m to 1.5 mbsf in core ARA07C GC13 and 0.8 mbsf at Site ARA07C GC14, respectively. Below these depths at Sites ARA07C GC13 and 14, there was no change in the slope of the alkalinity (Figure 5.13). These results are related to the biogeochemical reactions with the chemical zones in the natural marine sediment column.

Within marine sediments, organic matter decomposes via two main microbial pathways: POCSR and ME, as described by Equations 1 and 2:

$$\text{POCSR: } 2CH_2O + SO_4^{2-} \rightarrow 2HCO_3^- \quad \text{(Eq. 1)}$$
$$\text{ME: } CH_2O \rightarrow 2CO_2 + CH_4 \quad \text{(Eq. 2)}$$

Sulfate (SO_4^{2-}) acts as an electron acceptor in the upper tens of meters, where it fuels both POCSR (Eq. 1) and AOM (Eq. 3).

$$\text{AOM: } CH_4 + SO_4^{2-} \rightarrow HCO_3^- + HS^- + H_2O \quad \text{(Eq. 3)}$$

AOM occurs within the SMTZ, where SO_4^{2-} is depleted and CH_4 concentration starts to increase (Borowski et al., 1996). Unfortunately, SO_4^{2-} concentration of pore fluid was not analyzed onboard during this expedition. However, the depth of SMTZ can be roughly estimated by the downcore profile of alkalinity. Alkalinity in the sediment above and within the SMTZ is produced by organic matter degradation via POCSR and AOM (Eqs. 1 and 3). Sulfate is the main electron acceptor for these reactions; it is supplied to the pore fluids from the overlying bottom seawater, where it has a concentration of ~30 mM. Because of the stoichiometry of the reactions (Eqs. 1, 2, and 3), the slope of alkalinity in the downcore profile should be changed around the SMTZ and the maximum value of alkalinity around the SMTZ have lower values than ~60 mM. The analyzed maximum value of alkalinity from the pore fluids at Site ARA07C GC02-1, 05, 07 were not higher than ~15 mM and its slope at the downcore profile did not significantly change, which indicates that these sites do not reach the SMTZ. On the contrary, the analyzed maximum value of alkalinity from the pore fluids at Sites ARA07C GC13 and GC14 are ~ 30 mM and the slope of the alkalinity downcore profile remarkably changed at ~ 1.5 mbsf at Site ARA07C GC13 and ~0.8 mbsf at Site ARA07C GC14, which was approximately consistent with SMTZ at these sites. Around the SMTZ, salinity, chlorinity, and alkalinity of pore fluids from box cores do not show significant difference with depth but have relatively constant values.

Authigenic carbonates were found from two stations, Sts. 13 and 14 (Figure 5.15; Table 5.7). Sulfate (SO_4^{2-}), major and minor cations, isotope (δD, $\delta^{18}O$, and $\delta^{13}C_{DIC}$), and DOC properties will be determined during the post cruise.

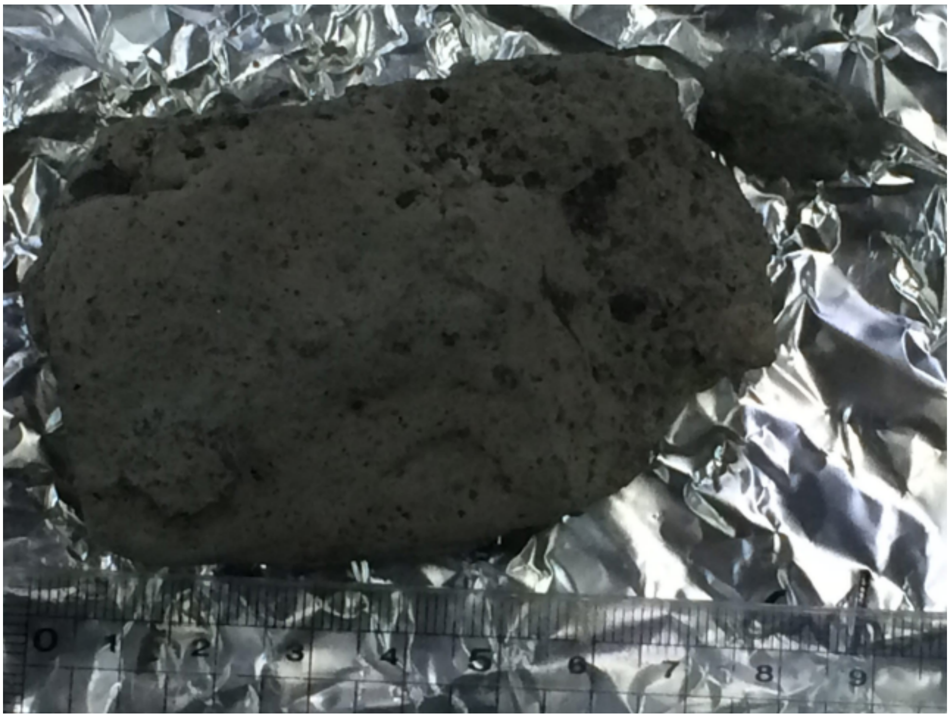

Figure 5.12. Massive authigenic carbonate from Site ARA07C GC13.

Table 5.7. Information of authigenic carbonate from ARA07C Expedition.

Sample No	Site	Depth (mbsf)	Remark
1	GC13	0.42-0.50	-
2		0.72-0.80	-
3		1.16-1.22	massive
4		1.71-1.72	dark black color
5	GC14	0.64-0.71	massive
6		0.91-1.09	plate

5.3.3. Gas chemistry

14 HS samples, 2 VG samples and 3 BG samples were collected from 7 gravity cores during the ARA07C Expedition (Table 5.8). Since the gas chromatograph does not prepare in the vessel, gas compositions in HS, VG, and GH were not determined. During the post cruise, following the procedure described by Pimmel and Claypool (2001), HS will be analyzed by an Agilent Technologies 7890A gas chromatograph with flame ionization (FID) and thermal conductivity detectors (TCD) in KIGAM to analyze for hydrocarbon composition and CO_2. VG and BG samples will be also analyzed by Agilent Technologies 7890A gas chromatograph in KIGAM. In addition, the stable carbon and hydrogen isotopic ratios ($\delta^{13}C_{CH4}$, $\delta^{13}C_{CO2,}$ and δD_{CH4}) of the selected samples of HS, VG and BG gases based on the gas compositions will be

obtained using an isotope ratio gas chromatograph-mass spectrometer (GC-IRMS) at Isotech, Champaign, IL.

To estimate the conversion ratio at which methane can be produced by in-situ carbon dioxide reduction and to understand the organic matter properties in the sediment column, we will carry out isotopic compositions ($\delta^{13}C_{TOC}$), Rock-Eval analysis, and biomarker analyses of organic matter in the sediment during the post cruise.

5.3.4. Biomarkers

Preliminary results of microbial lipid biomarkers in the sediments and authentic carbonates were not available on aboard, thus further analyses will need to be performed in the organic geochemical laboratory at the Hanyang University, Korea. However, we may expect that they significantly show the variability of spatial and vertical microbial lipid properties based on the preliminary biogeochemical observation in the study sites.

Table 5.8. Information of headspace gas (HS) samples in each site from ARA07C Expedition.

Gas Type	Site	Sample No	Depth (mbsf)
HS	GC2	1	3.4
		2	1.9
		3	0.4
	GC 2-1	4	3.45
		5	2.06
		6	0.57
	GC 3	7	3.78
		8	2.36
		9	0.86
	GC 5	10	1. 395
	GC 7	11	1. 365
	GC 13	12	2.37
		13	1.12
	GC 14	14	1.61
VG	GC 13	1	2.02
	GC 14	2	1.25
BG	GC 13	1	2.37
		2	2.37
		3	2.37

5.3.5. Microbial structure and genomic analysis

For the bacterial and archaeal community analysis, total genomic DNA will be extracted and 16S rRNA gene sequences will be amplified using barcoded bacterial and archaeal primers, respectively. Then, sequencing of 16S rDNA amplicons will be carried out using MiSeq (Illumina) and the microbial community and diversity will be analyzed according to the environmental factors. In addition, alpha- and beta- diversity will be calculated and compared to understand the key players in the methane production and oxidization and the factors shaping the microbial community in the methane hydrate-bearing sediments. This will provide the clues to understand the microbial roles in methane flux. To obtain the genomes of the key players, single cell genomic analysis will be performed and the metabolism in methane cycles will be investigated.

5.3.6. Cultivation and microcosm study

For the cultivation of microorganisms, gas in the headspace of serum bottles will be analyzed. In case the concentration of methane increases, the subculture in the fresh medium will be performed. If the isolates are obtained, the identification will be performed using 16S ribosomal gene sequences and the physiological characteristics will be investigated. To investigate the impact of temperature on the production or reduction of methane, gas analysis will be performed and the microbial community change using the next generation sequencing will be analyzed.

5.3.7. Mineralogy

To know the properties of clay and heavy mineral in the Arctic Sea area, total 208 sediments samples were collected at the working core of GC during the ARA07C Expedition (Table 5.9). The sampling interval was every 10-cm and samples were stored about 4 ^{o}C in refrigerator. In addition, Mn nodules were sampled to identify their origin and digenetic process by mineralogical and geochemical tools.

Bulk sediment will be separated into fine and coarse fraction at the laboratory of Gyeongsang National University. XRD will be performed using the fine-sediment fraction to identify clay mineral compositions and to estimate the relative composition of 4 major clay minerals such as illite, chlorite, kaolinite and smectite in the Gyeongsang National University. In addition, EPMA (Electron Probe X-ray microanalyzer) will be used to analyze the chemical compositions and distribution of major elements of heavy minerals.

Table 5.9. Summarized sample information of the mineralogical study.

Core Type	Site Name	Section No.	Sampling No
GC	ARA07C GC_ST-02B	Ⅰ	7
		Ⅱ	15
		Ⅲ	15
	ARA07C GC_ST-03	Ⅰ	11
		Ⅱ	17
		Ⅲ	17
	ARA07C GC_ST-05	-	14
	ARA07C GC_ST-07	-	17
	ARA07C GC_ST-13	Ⅰ	16
		Ⅱ	13
	ARA07C GC_ST-14	-	17

BC	ARA07C BC_ST-02	-	16
	ARA07C BC_ST_07	-	16
	ARA07C BC_ST_13	-	17

5.3.8. Heat flow

During the expedition, we made an attempt to measure geothermal gradient and thermal conductivity at six stations (Sts. 02b, 03, 05, 07, 13 and 14; Figure 5.16; Table 5.10) with water depth range of 44 to ~610 m. Four of them (Sts. 02b, 03, 05 and 07) were located along the longest multi-channel seismic survey line, perpendicular to the East Siberian continental shelf-slope while two of them (Sts. 13 and 14) do in the western slope of the Chukchi Plateau in the Arctic Ocean. The former four stations were chosen to distribute as evenly as possible to make a thermal profile across shelf-slope area. On the other hand, the latter two stations were chosen to know the gas hydrate stability zone because gas hydrate occurred in the core capture below 6 m-long barrel at St. 13.

Annual temperature variation in bottom water should be taken into consideration for data collected above ~300 mbsl because halocline reaches up to 300-400 mbsl (Stein, 2008). In the case of Laptev Sea, an annual temperature change higher than 1°C was observed above 500 mbsl (Dmitrenko et al., 2009), which causes temperature variation of 1/e° K at 2 mbsf with a common value for thermal diffusivity (e.g., Goto and Matsubayashi, 2008).

All data will be processed at KOPRI after the expedition.

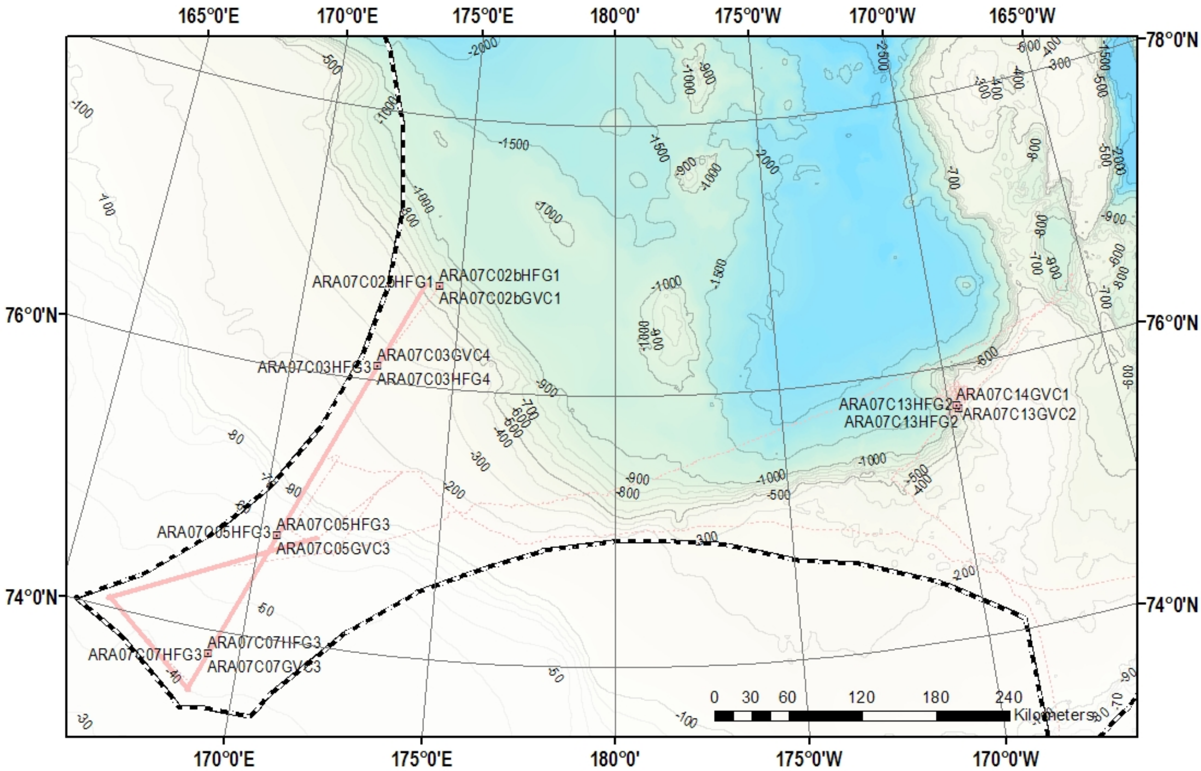

Figure 5.13. Location map of geothermal gradient (HFG) and thermal conductivity (HFT) measurements. Thick line for the multi-channel seismic survey line; dashed line for ship track; blank-white line for the EEZ.

Table 5.10. Station list for geothermal gradient (HFG) and thermal conductivity (HFT) measurements

Expedition	Leg	Station No.	Gear	Working order	St. Full Name	Lat_D	Lat_M	Lon_D	Lon_M	LAT	LON	WD
ARA07	C	st02b	HFG	1	ARA07C02bHFG1	76	44.7789	174	19.2175	76.746315	174.320292	-648
ARA07	C	st02b	HFT		ARA07C02bGVC1	76	44.7789	174	19.2175	76.746315	174.320292	-648
ARA07	C	st03	HFG	3	ARA07C03HFG3	76	6.44509	172	39.2902	76.107418	172.654837	-308
ARA07	C	st03	HFG	4	ARA07C03HFG4	76	6.44509	172	39.2902	76.107418	172.654837	-308
ARA07	C	st03	HFT		ARA07C03GVC4	76	6.44509	172	39.2902	76.107418	172.654837	-308
ARA07	C	st05	HFG	3	ARA07C05HFG3	74	45.53526	170	27.3295	74.758921	170.455492	-60
ARA07	C	st05	HFT		ARA07C05GVC3	74	45.53526	170	27.3295	74.758921	170.455492	-60
ARA07	C	st07	HFG	3	ARA07C07HFG3	73	48.87288	169	11.64789	73.814548	169.194132	-44
ARA07	C	st07	HFT		ARA07C07GVC3	73	48.87288	169	11.64789	73.814548	169.194132	-44
ARA07	C	St13	HFG	2	ARA07C13HFG2	75	40.7708	-169	44.2718	75.679513	-169.73786	-610
ARA07	C	St13	HFT		ARA07C13GVC2	75	40.7708	-169	44.2718	75.679513	-169.73786	-610
ARA07	C	St14	HFG	1	ARA07C14HFG1	75	42.20115	-169	45.55219	75.703353	-169.75920	
ARA07	C	St14	HFT		ARA07C14GVC1	75	42.20115	-169	45.55219	75.703353	-169.75920	

5.3.9. Shear strength

The maximum torque was measured on the all retrieved core from six stations (Sts. 02b, 03, 05, 07, 13 and 14; Figure 5.17; Table 5.9). An increasing trend with depth was identified on a plot of shear strength-depth (Figure 5.17). In terms of proximity from onshore, for the same depth in the plot, the shear strength of sediments from shallow water depths (Sts. 05 and 07) seems to be significantly higher than one of sediments from deeper water depths (Sts. 02B and 03). Results from mound features in the western slope of the Chukchi Plateau (Sts. 13 and 14) showed slightly higher values compared to results from similar water depths in the slope in the East Siberian Sea (Sts. 02b and 03).

As the shear strength at the base was found to have reached up to 30 to >50 kN/m^2 , this has interesting implications: a) the gravity corer with 6 m-long barrel of the Araon may penetrate depth having 30 to 50 kN/m^2, b) hard ground which was not penetrated by the gravity core with 6 m-long barrel located shallower in the shelf than in the slope in the East Siberian Sea, and c) at mound features at Stations 13, where gas hydrate sample was recovered, and 14, where similar characteristics were shown in the SBP profile, such hard ground at 1.7-2.4 m interval possibly consist of gas hydrate/authigenic carbonate.

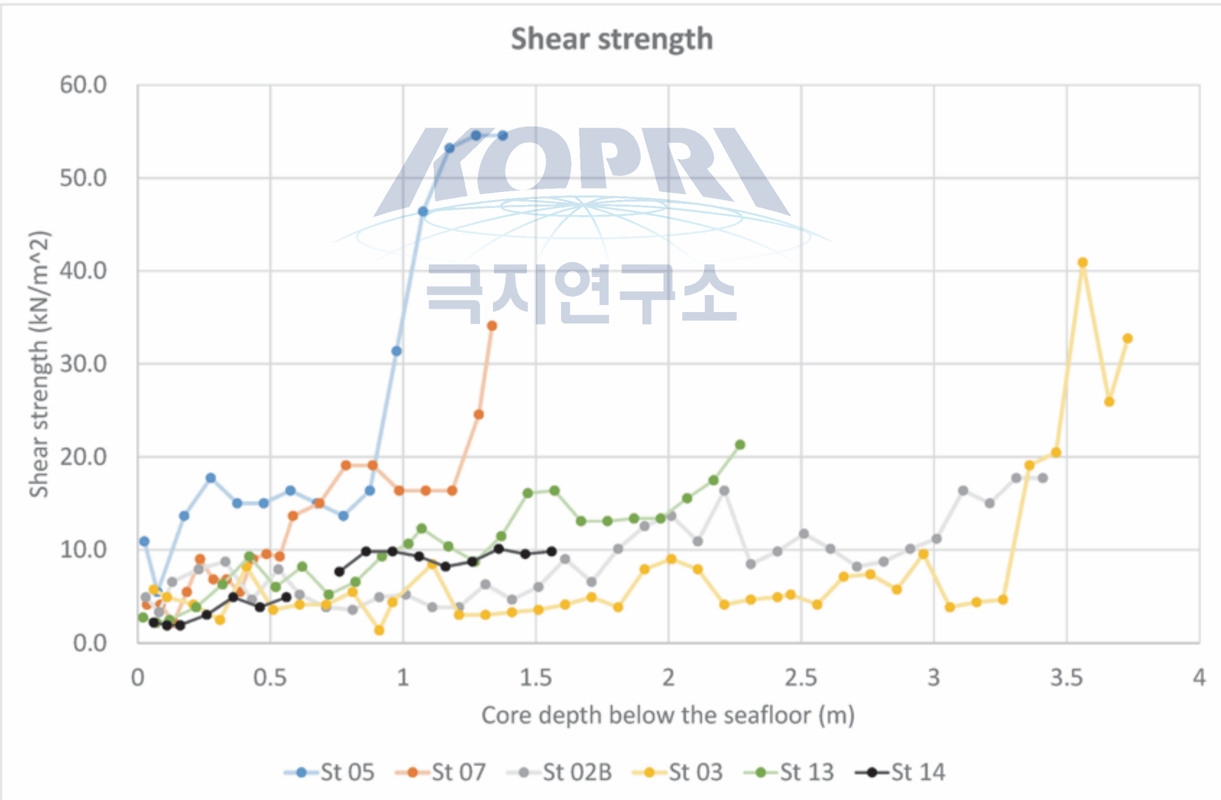

Figure 5.14. Results of shear strength measurement. See Figure 5.16 and Table 5.10 for location.

5.3.10. Magnetic susceptibility

The magnetic susceptibility was measured for all retrieved cores at six stations (Sts. 02b, 03, 050, 07, 13 and 14; Figure 5.18). Results seems to be identified in terms of locality: a) inner shelf stations (Sts. 05 and 07) and b) continental slope stations (Sts. 02 and 03) in the East Siberian Sea, and c) mound features in the western slope of the Chukchi Sea in the Arctic Ocean

(Sts. 13 and 14). One should note that abnormally low values observed in section top and bottom can be artificial ones caused by area average of the probe with 2 cm diameter for readings beyond sediments.

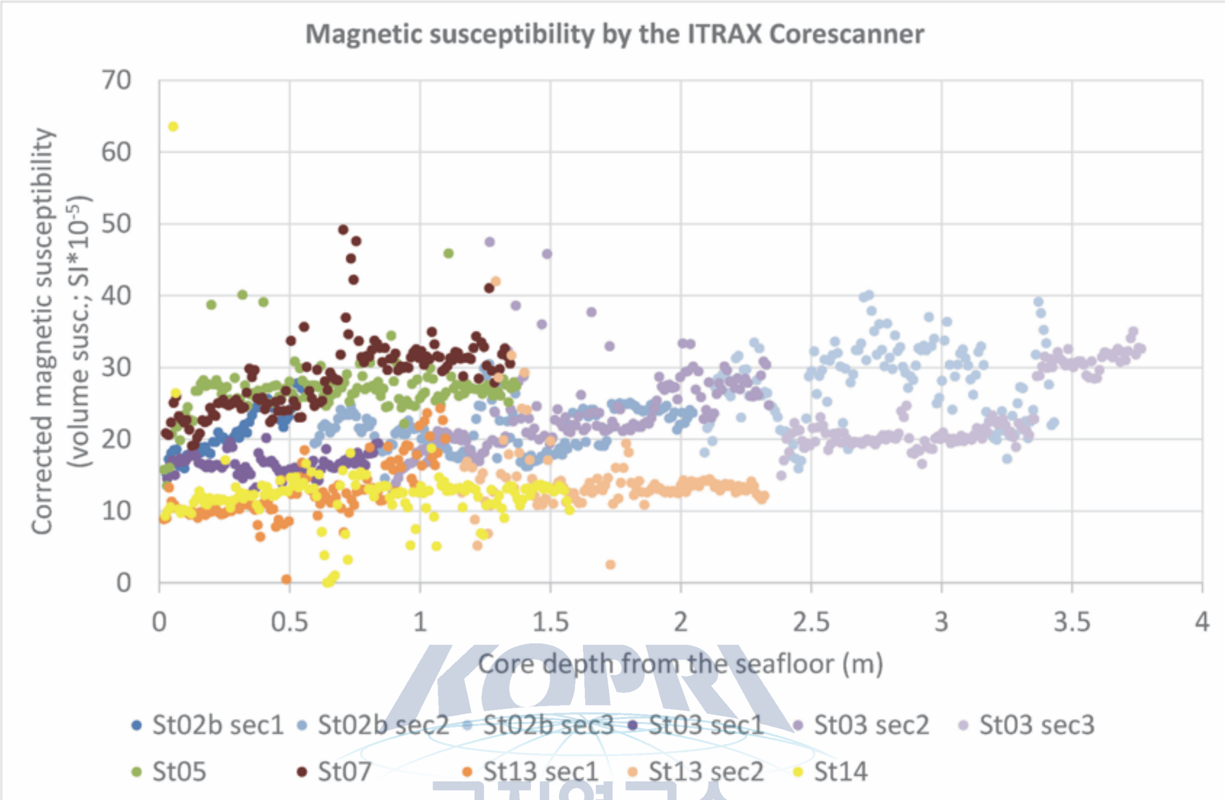

Figure 5.15. Results of magnetic susceptibility measurement. See Figure 5.16 and Table 5.10 for location.

5.4. Summary

We collected seven GCs and eight BCs through the ARA07C Expedition. Using these core samples, we prepared the samples for the fluid and gas chemistry, biogeochemistry, microbiology, mineralogy, and heat flow research during the post cruise study. So far, there are a few preliminary results only. However, we found the gas hydrate and authigenic carbonate at Sites ARA07C GC13 and GC14, where the SMTZ depth is very shallow (< 1.5 mbsf) based on the downcore profile of alkalinity. We believe that the results from the geological, geochemical and biogeochemical data from sediment, seawater, pore fluid and gas, which will be analyzed during the post cruise, can give clues to understand the carbon cycles, biogeochemistry and microorganism within the sediment column in the Arctic Sea area. In addition, results of heat flow and shear strength measurements may play an important role as a ground truth data for thermal and mechanical modeling work. Magnetic susceptibility profile can be used for age correlation.

Reference

Barnes, R.O., Goldberg, E.D., 1976. Methane production and consumption in anoxic marine-sediments. Geology 4, 297-300.

Borowski, W. S., C. K. Paull, W. Ussler III, 1996. Marine pore-water sulfate profiles indicate in situ methane flux from underlying gas hydrate. Geology 24, 655-658,

Canfield, D. E, .Thamdrup, B., 2009. Towards a consistent classification scheme for geochemical environments, or, why we wish the term 'suboxic' would go away. Geobiology 7, 385-392. DOI: 10.1111/j.1472-4669.2009.00214.x.

Collett, T.S., 2009. Geologic and engineering controls on the production of permafrost-associated gas hydrate accumulations. In: Proceedings of the 6th

Dmitrenko IA, Kirillov SA, Ivanov VV, Woodgate RA, Polyakov IV, Koldunov N, Fortier L, Lalande C, Kaleschke L, Bauch D, Hölemann JA, Timokhov LA (2009) Seasonal modification of the Arctic Ocean intermediate water layer off the eastern Laptev Sea continental shelf break. Journal of Geophysical Research: Oceans 114:n/a-n/a. doi:10.1029/2008JC005229

Frey, K., Smith, L.C., 2005. Amplified carbon release from vast West Siberian peatlands by 2100. Geophys. Res. Lett. 32, L09401.

Gieskes, J.M., Gamo, T., Brumsac, H., 1991. Chemical Methods for Interstitial Water Analysis aboard JOIDES Resolution. Ocean Drilling Program Technical Note 15. Ocean Drilling Program, College Station, TX.

Goto S, Matsubayashi O (2008) Inversion of needle-probe data for sediment thermal properties of the eastern flank of the Juan de Fuca Ridge. Journal of Geophysical Research: Solid Earth 113:B08105. doi:10.1029/2007JB005119

Heeschen, K.U., Collier, R.W., de Angelis, M.A., Suess, E., Rehder, G., Linke, P., Klinkhammer, G. P., 2005. Methane sources, distributions, and fluxes from cold vent sites at Hydrate Ridge, Cascadia Margin. Global Biogeochem. Cycles 19, GB2016. http://dx.doi.org/10.1029/2004 GB002266.

Hesse, R., 2003. Pore water anomalies of submarine gas-hydrate zones as tool to assess hydrate abundance and distribution in the subsurface. What have we learned in the past decade? Earth-Sci. Rev. 61 149-179.

Jin YK, Riedel M, Hong JK, Nam SI, Jung JY, Ha SY, Lee JY, Kim Y-G, Yoo J, Kim HS, Kim G, Conway K, Standen G, Ulmi M, Schreker M (2015) Overview of field operations during a 2013 research expedition to the southern Beaufort Sea on the RV Araon. In: Geological Survey of Canada, Open File, p 181

Jin YK, Dallimore SR (2016) Canada-Korea-USA Beaufort Sea Geoscience Research ARA05C Marine Research Expedition Program: Summary of 2014 Activities. In. Geological Survey of Canada, Natural Resources Canada

Kim, J.-H., Torres, M. E., Hong, W.-L., Choi, J., Riedel, M., Bahk, J.-J., Kim, S.-H, 2013. Pore fluid chemistry from the second gas hydrate drilling expedition in the Ulleung Basin (UBGH2): source, mechanisms and consequences of fluid freshening in the central part of the Ulleung Basin, East Sea. *Mar. Petrol. Geol., 47,* 99-112, doi:10.1016/j.marpetgeo.2012.12.011.

Paull C, Dallimore SR, Collett T, Jin YK, Mienert J, Mangelsdor K, Riedel M (2011) Methane release and geolgic processes associated with warming permafrost and gas hydrate deposits beneath the Beaufort Sea Shelf and upper Slope. In:

Pimmel, A., Claypool, G., 2001. Introduction to Shipboard Organic Geochemistry on the JOIDES Resolution. Ocean Drilling Program Technical Note 30, College Station, TX.

Ratcliffe EH (1960) The thermal conductivities of ocean sediments. Journal of Geophysical Research 65:1535-1541. doi:10.1029/JZ065i005p01535
Regnier, P., Dale, A. W., Arndt, S., LaRowe, D. E., Mogollon, J., Van Cappellen, P., 2011. Quantitative analysis of anaerobic oxidation of methane (AOM) in marine sediments: a modeling perspective. Earth Sci. Rev. 106, 105–130.
Reeburgh, W. S., 2007. Oceanic methane biogeochemistry. Chem. Rev. 107, 486-513
Romanovskii NN, Hubberten H-W (2001) Results of permafrost modelling of the lowlands and shelf of the Laptev Sea Region, Russia. Permafrost and Periglacial Processes 12:191-202. doi:10.1002/ppp.387
Ruediger S (2008) Arctic Ocean Sediments: Processes, Proxies, and Paleoenvironment. Elsevier
Ruppel C (2014) Permafrost-Associated Gas Hydrate: Is It Really Approximately 1 % of the Global System? Journal of Chemical & Engineering Data. doi:10.1021/je500770m
Shakhova, N.I., Semiletov, I., Leifer, I., Salyuk, A., Rekant, P., Kosmach, D., 2010. Geochemical and geophysical evidence of methane release over the East Siberian Arctic Shelf. J. Geophys. Res. 115, 14. http://dx.doi.org/10.1029/2009JC005602. C08007.
Torres, M.E., Kim, J.-H., Choi, J., Ryu, B.-J., Bahk, J.-J., Riedel, M., Collett, T. S., Hong, W.-L., Kastner, M., 2011. Occurrence of high salinity fluids associated with massive nearseafloor gas hydrate deposits, paper presented at the 7th International Conference on Gas Hydrates (ICGH2011), Edinburgh, United Kingdom.
Yamashita S, Moriwaki S, Hachikubo A, Minami H, Shoji H, Kawaguchi T, Kataoka S (2011) Strength change of seabed soils due to the vaporazation of dissolved gas in the pore water. In:International Symposium on Deformation Characteristics of Geomaterials, September 1-3

Chapter 6. Water Column Study

Y.-S. Choi, Y.S. Kwon, N.W. Heo, and Y.M. Lee

6.1. Introduction

The Arctic Ocean has warmed over the past few decades (Polyakov et al., 2007, Solomon et al., 2007, Steele et al., 2008). This area is currently experiencing rapid environmental change due to natural and anthropogenic factors that include warming and other physical changes, as well as biology and ecosystem structure changes (Bates and Mathis, 2009). In particular, change in extent and thickness of Arctic sea ice is recognized as a key indicator of Arctic climate change (Shimada et al., 2006).

Methane (CH_4) is the most abundant hydrocarbon in the atmosphere, where it plays a much more effective role as the greenhouse gas than carbon dioxide (CO_2). However, not much attention is paid to CH_4 as its global concentration is currently less than 2% of CO_2 in the troposphere. The ocean is thought to be a relatively small source of methane for the atmospheric budget, and the source process of oceanic methane includes the decomposition of methane clathrate hydrates. It is estimated that more than 10% of the methane hydrate of the world is buried below the Arctic Ocean basin and that the global atmospheric methane will be ten times the current level if one tenth of the methane buried below the Arctic Ocean is emitted into the atmosphere. The Arctic Ocean is presently experiencing rapid environmental change due to natural and anthropogenic factors including warming, sea-ice loss, and other physical changes that include biological and ecosystem structural changes. These environmental changes in the Arctic Ocean are expected to contribute to the instability of the gas hydrate layer of the seawater and sediments, which many researchers to capture the emission of CH_4 gases from seafloor.

During this cruise from Barrow, Alaska to Nome, Alaska through the East Siberian Sea (ARA07C, 25 Aug 2016 – 10 Sep 2016), we conducted CH_4 analysis in situ at sea in order to understand how much or how fast the methane in the Arctic Ocean passes through the water column to go out the atmosphere.

In addition, in relation to the global carbon cycle and the balance of carbon dioxide (CO_2) sinks and sources, changes in the Arctic environment and feedback could have a profound impact on the marine carbon cycle. CO_2 is one of the major components in understanding global warming and climate change underway at present. Atmospheric CO_2 is absorbed by the ocean or emitted from the ocean to the atmosphere via physical and biological processes. The Arctic Ocean has a great potential for uptake of atmospheric CO_2 because of high biological production and low temperature. According to Bate and Mathis (2009), the Arctic Ocean accounts for 5 to 14% of the total ocean CO_2 uptake. However, knowledge about the distribution of CO_2, air-sea CO_2 fluxes and the carbon cycle in the Arctic Ocean is uncertain due to relatively few observations and rapid changes in climate. Although the Arctic Ocean takes up atmospheric CO_2, other greenhouse gases, such as nitrous oxide (N_2O) and CH_4 , can be released into the atmosphere through nitrification, denitrification, and decay of detritus and thawing Arctic permafrost, which becomes a positive feedback to climate warming. It is unclear yet whether the decrease in radiative forcing from CO_2 uptake is offset by other greenhouse gases or not.

To improve our understanding of biogeochemical cycles of inorganic carbon between the ocean and the atmosphere in the Arctic Ocean, we also conducted measurements of dissolved inorganic carbon (DIC), total alkalinity (TA), partial pressure of CO_2 (pCO_2), pH of seawater, and nutrients throughout the study area.

We conducted a 16-day Arctic expedition from August 25 to September 10, 2016 using the Korea ice breaker RV Araon to investigate the spatial distribution of water mass in the East Siberian Sea (Figure 6.1). Specific details on the observations at the stations is listed in Table 6.1.

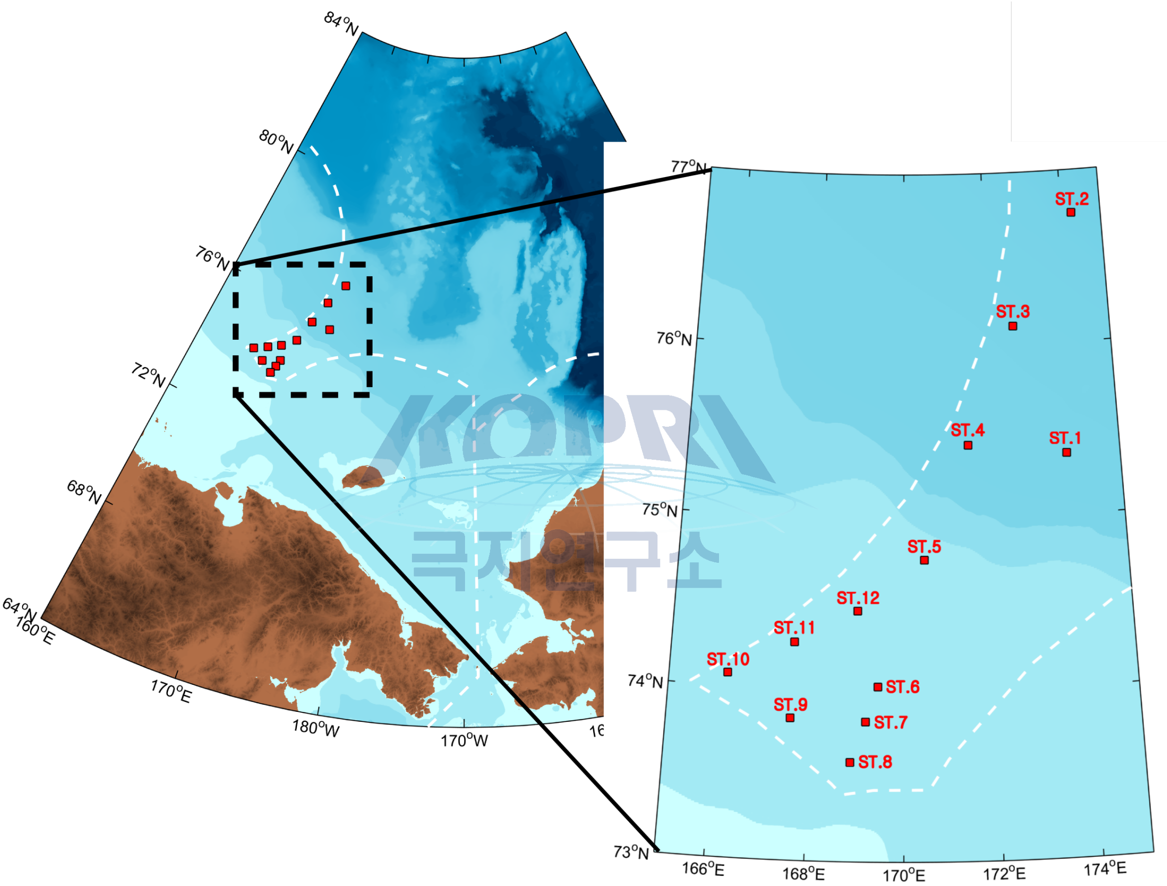

Figure 6.1. A station map of ARA07C Arctic cruise with color-mapped bathymetry. Red squares are CTD stations. White dash line denotes Russian EEZ and US EEZ lines.

Table 6.1. A list of CTD stations for ARA07C 2016 Arctic Ocean cruise.

Station	Start Time (UTC)		Latitude	Longitude	Depth
	YY-MM-DD	hh:mm	Deg. Min.	Deg. Min.	(m)
ST.1	2016-08-29	17:11	75°21.377'N	173°45.832'E	195
ST.2	2016-09-02	17:44	76°44.856'N	174°15.659'E	640
ST.3	2016-09-03	04:22	76°06.445'N	172°39.290'E	308
ST.4	2016-09-03	16:07	75°25.384'N	171°29.590'E	162
ST.5	2016-09-03	22:23	74°45.535'N	170°27.329'E	60
ST.6	2016-09-04	05:22	74°01.154'N	169°26.895'E	45
ST.7	2016-09-04	08:27	73°48.873'N	169°11.648'E	44
ST.8	2016-09-04	12:21	73°34.739'N	168°52.991'E	40
ST.9	2016-09-04	14:58	73°49.713'N	167°36.717'E	44
ST.10	2016-09-04	17:40	74°04.581'N	166°14.883'E	45
ST.11	2016-09-04	20:09	74°16.304'N	167°38.672'E	48
ST.12	2016-09-04	22:35	74°27.606'N	168°59.844'E	54

6.2. Methods

6.2.1. CTD casting

The CTD installed on the RV Araon was used for profiling and identifying vertical variation of temperature and salinity. Along the transects of hydrographic stations, hydro-casts of CTD (SBE 911*plus* CTD)/Rosette system with additional sensors (e.g., in situ data on phytoplankton concentrations (fluorometer), optical clarity (transmissometer), dissolved oxygen, altimeter and methane gas) were conducted to measure the vertical profiles of conductivity, temperature, depth, and other biochemical parameters (Figure 6.2a). During the CTD up-casting, 24 position rosette with 10-L Niskin bottles was used to obtain water samples from discrete depths for biological and geochemical analysis.

6.2.2. Ocean current measurement

A 300 kHz RDI lowered Acoustic Doppler Current Profiler (LADCP) was mounted on the CTD/Rosette frame to measure a full-depth profile of current velocities (Figure 6.2b). Using the conventional "shear method" for processing (e.g., Fischer and Visbeck, 1993), overlapping profiles of vertical shear of horizontal velocity were averaged and gridded to form a full-depth shear profile. The bin size was chosen as 5 m and the number of bins was 20.

6.2.3. Seawater sampling

Seawater sampling was carried out at 16 stations using a CTD/rosette sampler holding 24-10L Niskin bottles (OceanTest Equipment Inc., FL, USA) during Korea research ice breaker RV Araon cruise (ARA07C, August 25 – September 10, 2016).

(A) (B)

Figure 6.2. Hydrographic observation equipment: (a) SBE911plus CTD profiler and rosette water sampler, (b) 300kHz RDI lowered ADC

6.2.4. Measurements of the greenhouse gases (CH_4, CO_2, and N_2O)

Seawater sampling was carried out at 13 stations over the East Siberian Sea during the expedition. Seawater samples for CH_4, CO_2 and N_2O measurements were obtained from the Niskin bottles in the CTD/rosette system using the 200 mL glass jars. 50 mL of ultrapure (99.9999 %) nitrogen gas was subsequently injected into the glass jars with an airtight syringe to make the headspace. The glass jars were then put in the water bath (20°C) for equilibrium between the water and the headspace. After about 1 hour, the measurements of these samples were carried out using a gas chromatograph equipped with a flame ionization detector (FID; for CO_2 and CH_4 measurements) and an electron capture detector (ECD; for N_2O measurements). 40 mL of the headspace gas was drawn from the glass jars using the airtight syringe, and then injected into the instrument.

During the cruise, underway measurements of CO_2, CH_4 and N_2O were also carried out along the cruise track using the same instrument to estimate the rate of air-sea gas exchange. Seawater was pumped into the equilibrator from 5 - 6 m below the surface ocean and the headspace gas in the equilibrator was drawn into the gas chromatographic system (Figure 6.3). And the four standards were also analyzed for instrumental calibration at every sample analysis.

Figure 6.3. Gas chromatograph system for the measurement of the greenhouse gases including CH_4, CO_2, and N_2O.

6.2.5. Underway measurements of pCO_2

The flux of CO_2 across the sea surface is directly proportional to the difference in the fugacity of CO_2 between the atmosphere and the seawater. The fugacity is obtained by correcting the partial pressure of CO_2 (pCO_2) for non-ideality of the gas with respect to molecular interactions between CO_2 and other gases in the air, thus making pCO_2 an important parameter to measure (Pierrot et al., 2009). To investigate the air-sea exchange rate of CO_2, pCO_2 was monitored in real time using an automated flowing pCO_2 measuring system (Model 8050, General Oceanics Inc., USA) (Figure 6.4). The system is compact and operated by directing seawater flow through a chamber (the equilibrator) where the CO_2 contained in the water equilibrates with the gas present in the chamber (the headspace gas). To determine the CO_2 in the headspace gas, it was pumped through a non-dispersive infrared analyzer (LI-COR), which measured its CO_2 mole fraction. Instantaneously, and then returned to the equilibrator thus forming a closed loop. Periodically, atmospheric air was also pumped through the analyzer and its CO_2 mole fraction was measured. The analyzer was calibrated with four CO_2 standard gases at regular intervals.

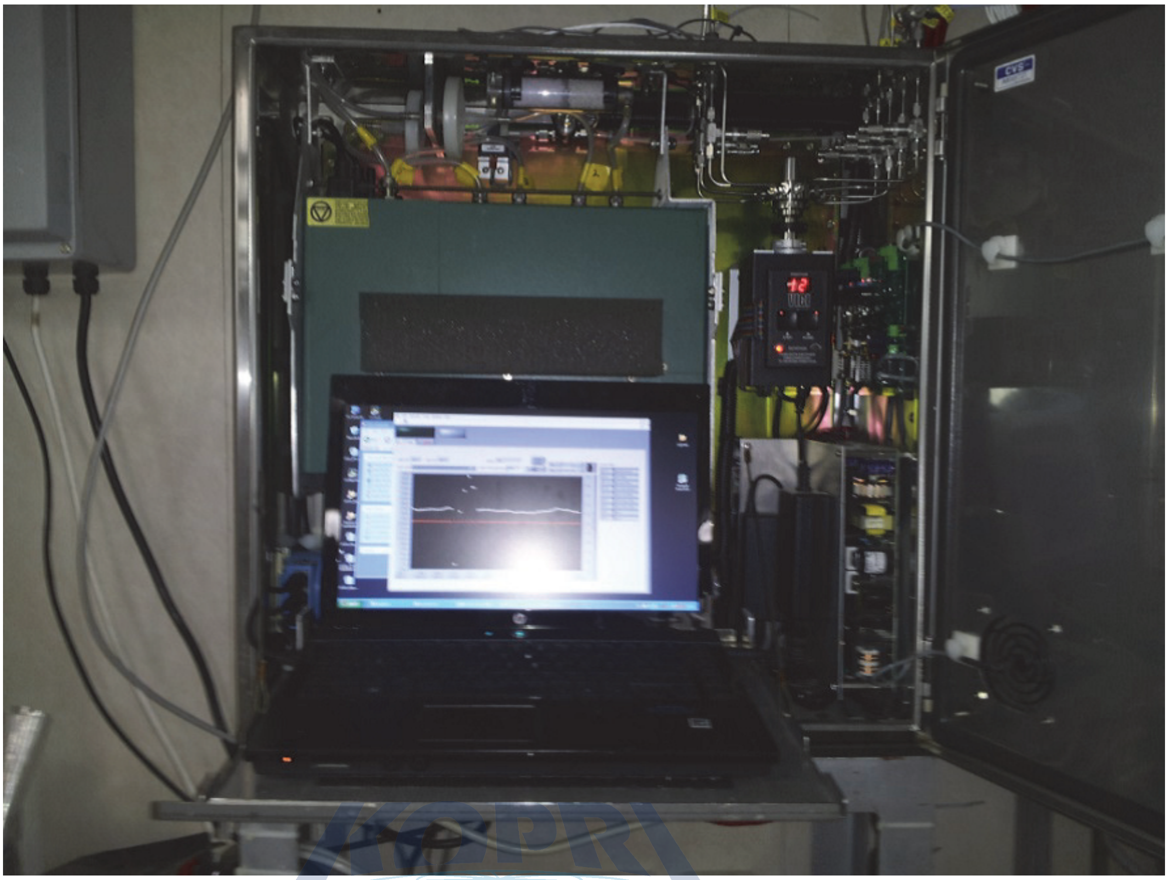

Figure 6.4. Automated system for of underway measurement pCO_2 (Li-COR).

6.2.6. Water column study on DIC, pH, and Nutrients

Upon obtaining the samples for GH gases from Niskin, seawater samples for DIC and TA measurements were drawn into pre-cleaned 500 ml borosilicate bottles. DIC and TA samples were subsequently poisoned with 200 µl of $HgCl_2$ to halt biological activity, sealed, and returned to KOPRI for analysis. DIC and TA samples will be analyzed using a VINDTA (Versatile INstrument for the Determination of Total Alkalinity) system.

Subsequently, seawater samples for pH measurements were drawn from the Niskin bottles into pre-cleaned 150 ml polyethylene bottles. The samples were delivered to the Analytical Chemistry Lab in R/V Araon, after which the pH of seawater was measured on board using a pH measurement system (Figure 6.5). Also, samples for nutrients (NH_4^+, NO_2^-, NO_3^-, PO_4^{3-}, SiO_4^{2-}) were collected from the Niskin rosette into 50 ml conical tubes and immediately stored in a freezer at −24°C prior to chemical analyses. The samples will be analyzed with standard colorimetric methods using a Quatro Auto Analyzer in the Korea Polar Research Institute.

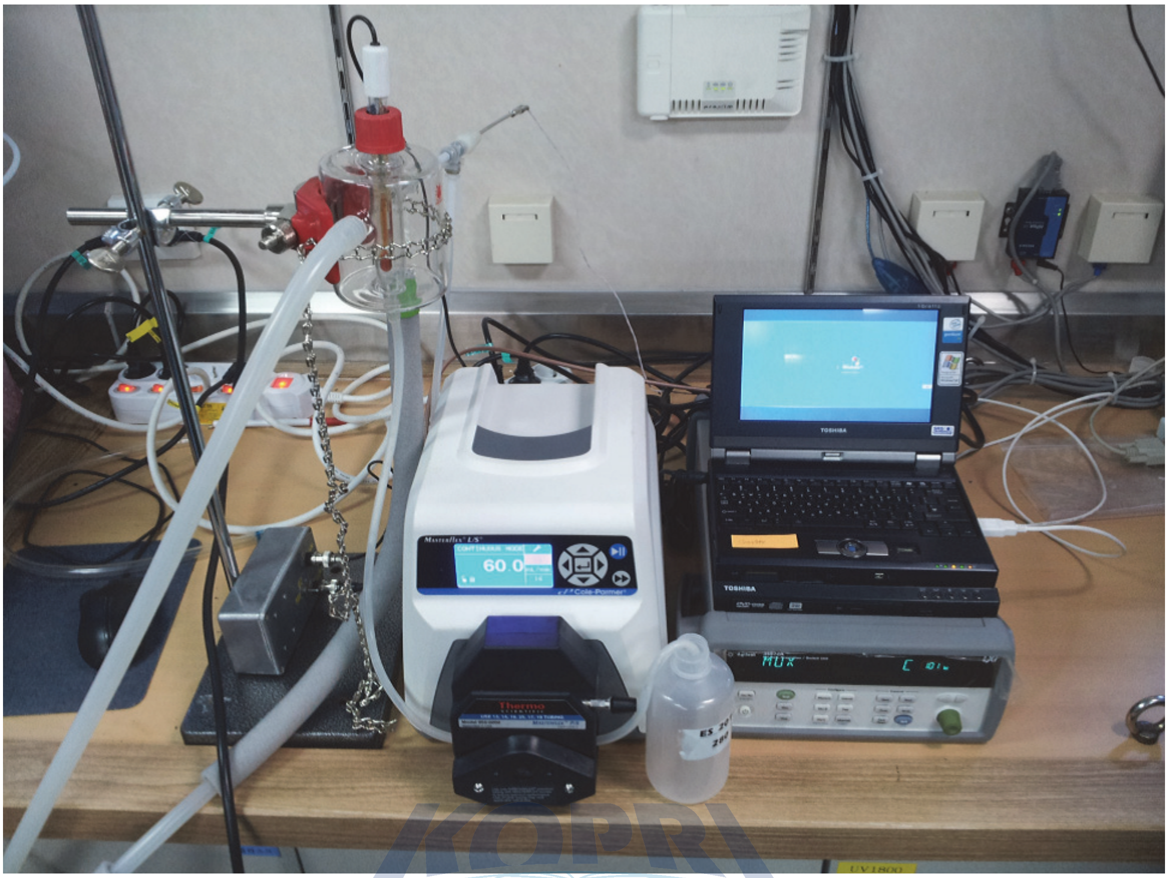

Figure 6.5. The pH meter for seawater samples.

6.2.7. Collection and processing of samples

At each station, five liter of seawater samples were collected using Niskin bottles according to the depth profile of the water column. (Table 6.2.). 1L of collected seawater was filtered on GF/F filter for chlorophyll concentration and preserved at -80°C. Four liters of seawater were filtered through 3.0-μm cellulose acetate membranes and then the filtrate was filtered again through 0.2-μm polyethersulfone membranes. The membranes were stored at –80°C. For nutrient analysis (nitrate, ammonium, phosphate, and silicate), about 40 ml of seawater was frozen at -20°C. For the cultivation of methangenic or methanotrophic archaea and sulfate-reducing bacteria, 0.6 ml of the sample with 20% glycerol was preserved at -80°C. To isolate the methane cycle-related bacteria and archaea, 2 ml of seawaters collected from 40m and 55m depth of the station 5, which the concentration of methane was high compared to other sites were inoculated in the MM medium and incubated at 4°C.

Table 6.2. List of seawater samples collected in East Siberia Sea

Station	Sample No.	Latitude	Longitude
St01	ARA07C-CTD01-0m	75.3563 N	173.7641 E
	ARA07C-CTD01-10m		
	ARA07C-CTD01-30m		
	ARA07C-CTD01-45m		
	ARA07C-CTD01-80m		
	ARA07C-CTD01-120m		
	ARA07C-CTD01-190m		
St02	ARA07C-CTD-St02-0m	76.7476 N	174.2610 E
	ARA07C-CTD-St02-35m		
	ARA07C-CTD-St02-50m		
	ARA07C-CTD-St02-100m		
	ARA07C-CTD-St02-170m		
	ARA07C-CTD-St02-350m		
	ARA07C-CTD-St02-632m		
St03	ARA07C-CTD-St03-0m	76.1074 N	172.6549 E
	ARA07C-CTD-St03-20m		
	ARA07C-CTD-St03-40m		
	ARA07C-CTD-St03-145m		
	ARA07C-CTD-St03-200m		
	ARA07C-CTD-St03-300m		
St04	ARA07C-CTD-St04-0m	75.4232 N	75.4232 N
	ARA07C-CTD-St04-30m		
	ARA07C-CTD-St04-70m		
	ARA07C-CTD-St04-110m		
	ARA07C-CTD-St04-157m		
St05	ARA07C-CTD-St05-0m	74.7441 N	170.4551 E
	ARA07C-CTD-St05-15m		
	ARA07C-CTD-St05-30m		
	ARA07C-CTD-St05-40m		
	ARA07C-CTD-St05-50m		
	ARA07C-CTD-St05-2-40m		
	ARA07C-CTD-St05-2-55m		
St07	ARA07C-CTD-St07-0m	73.8151 N	169.1941 E
	ARA07C-CTD-St07-10m		
	ARA07C-CTD-St07-20m		
	ARA07C-CTD-St07-25m		
	ARA07C-CTD-St07-30m		

	ARA07C-CTD-St07-35m		
	ARA07C-CTD-St07-40m		
St08	ARA07C-CTD-St08-0m	73°34.739'N	168°52.991'E
	ARA07C-CTD-St08-20m		
	ARA07C-CTD-St08-30m		
	ARA07C-CTD-St08-35m		
UW-01	ARA07C-UW-01	75, 14.66452'N	171, 58.85258'W
UW-02	ARA07C-UW-02	72.25.47155'N	168. 27.69542'W

6.3. Results

The samples for DIC/TA and nutrients will be analyzed after all samples are returned to the Korea Polar Research Institute. For the results of greenhouse gases, pCO2, and pH, a variety of calculations and calibration are required to produce an accurate data set. We therefore report here only preliminary results which are not calibrated and not accurate.

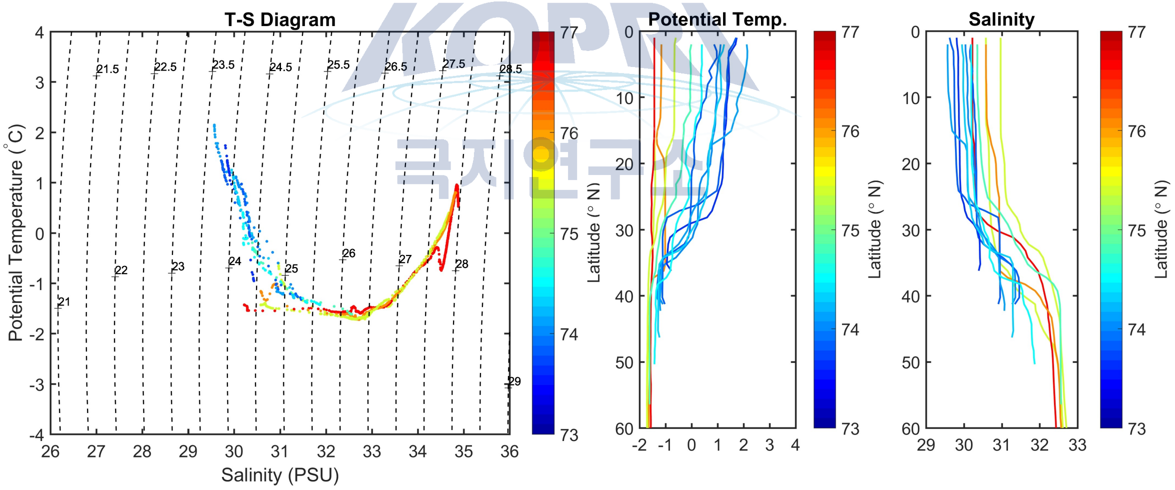

(A) (B)

Figure 6.6. (a) Potential temperature (T)-Salinity (S) diagram from ship-based CTD stations with casted latitude in color, (b) Vertical Profile of potential temperature (left) and salinity (right) at different CTD stations with casted latitude in color.

6.3.1. T-S diagram and vertical profile

During the expedition, 12 CTD stations were selected. Using deep downcasting data at each CTD station, we plotted the potential temperature (T)–salinity (S) diagram (Figure 6.6a). It shows that the study area is occupied by three distinct water masses: (1) Pacific summer water (PSW); (2) Pacific winter water (PWW); and (3) Atlantic water (AW); PSW is relatively warm, fresh water mass presenting temperature maximum layer at about 30~50m depth (Figure 6.6b).

PWW, a layer of relatively fresh (i.e., buoyant), cold water, lies immediately above the warm AW that is the water mass with the highest temperature and highest salinity.

6.3.2. Methane distribution

Methane at the surface seawater along the cruise is shown in Figure 6.7. Mean concentration was about 5 nM which is slightly higher than the value observed in the typical open ocean (~3 nM). There were three maximums of CH_4 in the cruise. However, the first two peaks are suspected to be outliers since R/V Araon past through sea ice areas and its pumping system of seawater to the equilibrator should be turned off. The third one is likely to indicate high methane area where we found out that there were some methane gas plumes on the seafloor (by Multi-beam expedition) and the methane concentrations in water column also were extremely high (see Figure 6.8.).

As shown in Figure 6.8, CH4 concentrations at stations 1 to 4 were in a typical range (about 4 nM in average) while an abrupt increase could be observed at station 5. Methane is especially high at the bottom and still remains relatively high at the surface. It is expected that the methane emitted from the seafloor would be diluted by lateral current of seawater or oxidized to carbon dioxide by microbes in the water column before reaching the surface.

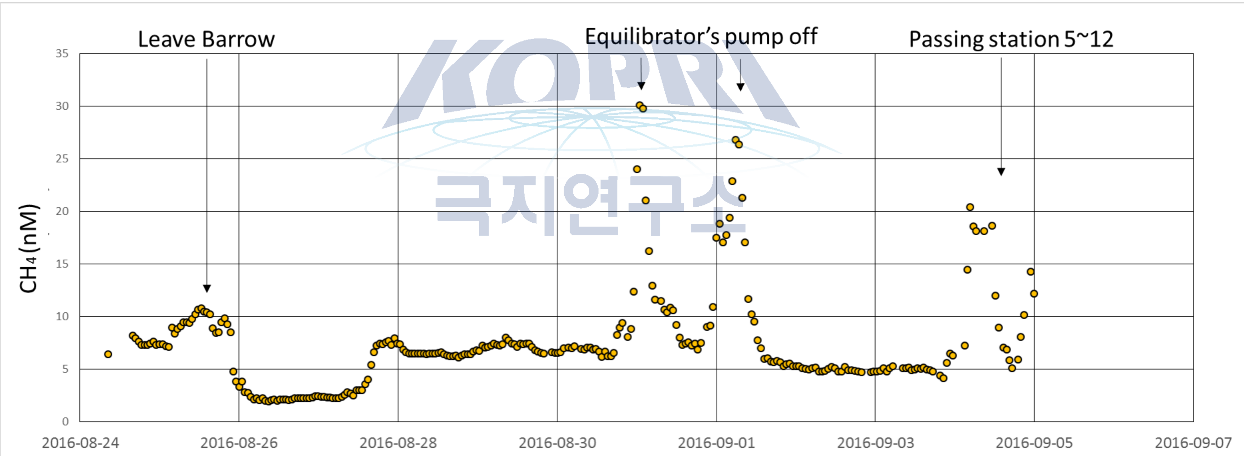

Figure 6.7. The variation of CH_4 in the surface ocean through the ship track during this cruise.

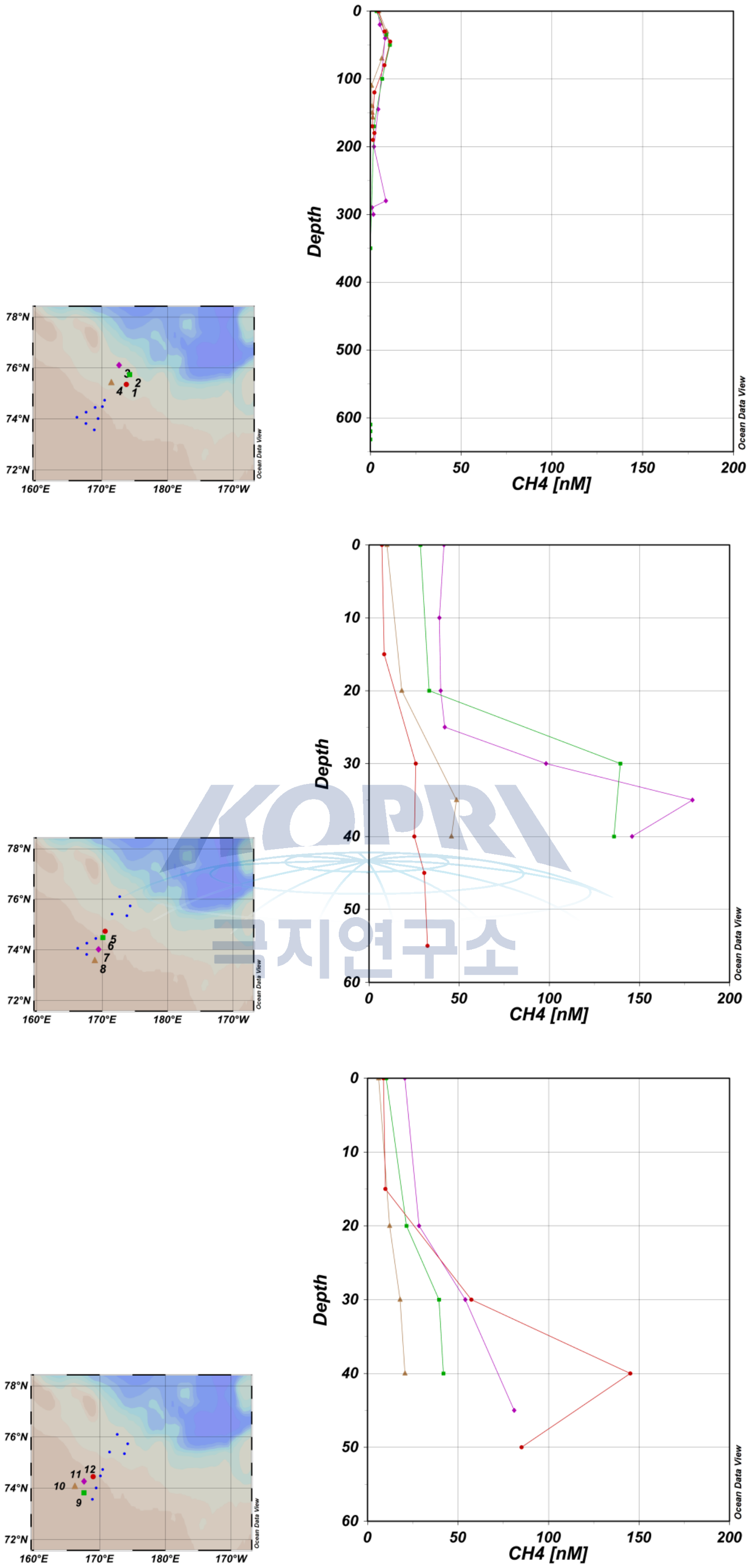

Figure 6.8. The vertical distribution of CH_4 at each station.

6.3.3. pH

The sea water pH at each station is shown in Figure 6.9. pH values are important property of seawater for understanding the chemical and biological environment of the area and these results will be used in calibrating and examining the DIC processes occurring in the water columns.

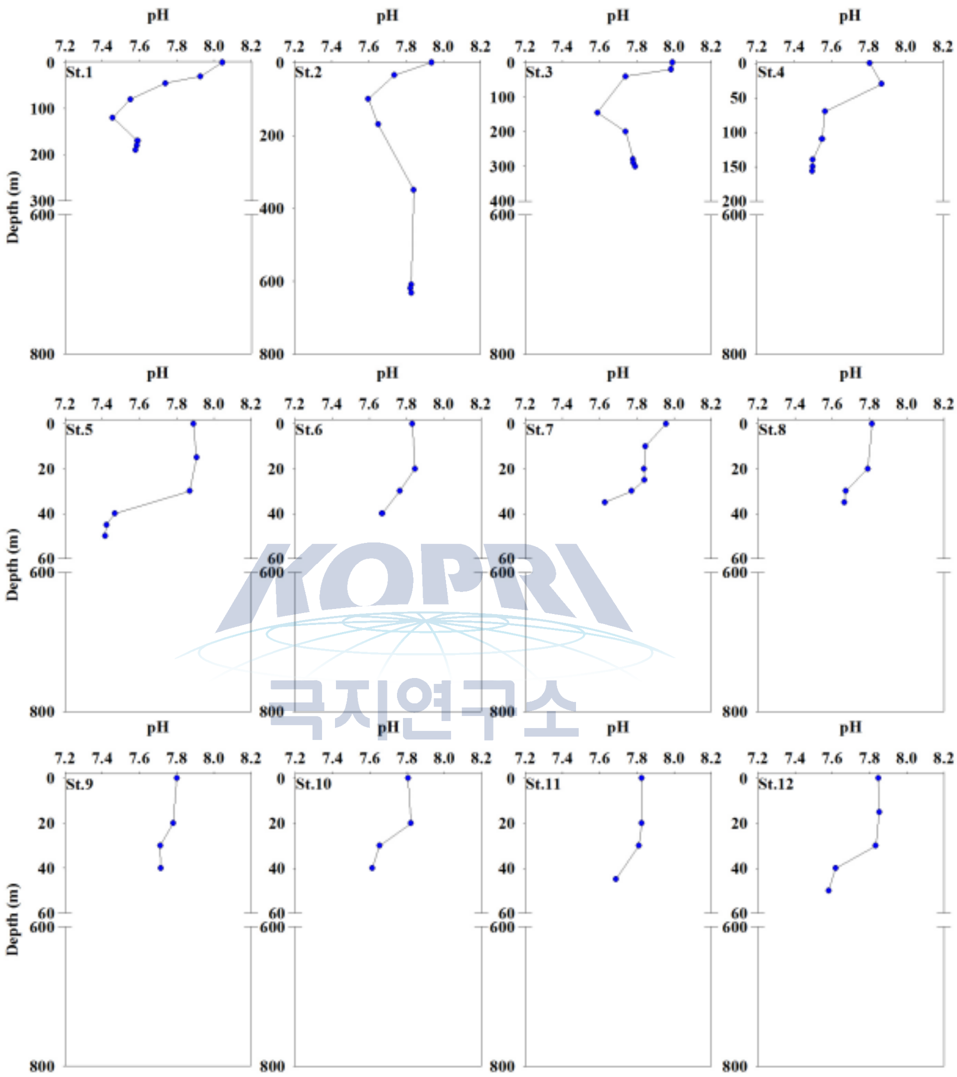

Figure 6.9. pH of seawater at each station.

6.3.4. Microbial structure

For the bacterial and archaeal community analysis, total genomic DNA will be extracted and 16S rRNA gene sequences will be amplified using barcoded bacterial and archaeal primers, respectively. Then, sequencing of 16S rDNA amplicons will be carried out using MiSeq (Illumina) and the microbial community and diversity will be analyzed according to the environmental factors. In addition, alpha- and beta- diversity will be calculated and compared to understand the key players in the methane production and oxidization and the factors shaping the microbial community within the water column which will provide the clues to understand the microbial roles in methane flux.

6.3.5. Cultivation

For the cultivation of microorganisms, the gas in the headspace of serum bottles will be analyzed and in case the concentration of methane is increased the subculture in the fresh medium will be performed. If the isolates are obtained, the identification will be performed using 16S ribosomal gene sequences and the physiological characteristics will be investigated.

6.4. Summary

We surveyed dissolved CH_4 concentrations at the surface seawater as well as in water columns. This expedition will give an insight in determining the emission rate from the sea floor to the water column and eventually to the atmosphere in the Arctic Ocean driven by the current change in the Arctic. Large CH_4 concentrations were encountered at the stations where gas ebullition flares were detected by the echo sounder and the multi-beam survey. Preliminary estimate shows that the surface concentrations rose up to ~20 nM in the gas flare areas and that deep water near the seafloor contains up to 180 nM of CH_4. These observations unveil that the methane release at the seafloor is actively occurring in the Arctic. It is urgent that we pay attention to the large scale of methane release at the seafloor of the Arctic Ocean, which will eventually contribute to the atmospheric CH_4 source and to global climate change.

Other chemical properties than CH_4 which are related to the carbon cycle in the water column were measured. These measurements include dissolved inorganic carbon, total alkalinity, pH, and pCO_2 which are key parameters to understand the chemical conversion of dissolved CH_4 via microbial processes, called methanotroph and methanogenesis. Some of these parameters were not yet analyzed onboard and thus underway.

References

Shimada, K., T. Kamoshida, M. Itoh, S. Nishino, E. Carmack, F. McLaughlin, S. Zimmermann, and A. Proshutinsky, 2006. Pacific Ocean flow: Influence on catastrophic reduction of sea ice cover in the Arctic Ocean. *Geophysical Research Letters*, 33, doi:1029/2005 GL 025624.

Solomon, S., D. Qin, M. Manning, R.B. Alley, T. Berntsen, et al., 2007. Technical Summary. In: *Climate Change 2007: The Physical Science Basis. Contribution of Working Group I to the Fourth Assessment Report of the Intergovernmental Panel on Climate Change*. (Eds.) S. Solomon, D. Qin, M. Manning, Z. Chen, M. Marquis, et al., Cambridge, UK/New York, Cambridge University Press.

Steele, M., W. Ermold, and J. Zhang, 2008. Arctic Ocean surface warming trends over the past 100 years. *Geophysical Research Letters*, 35, L02614, doi:10.1029/2007GL031651.

Pierrot, D., Neill, C., Sullivan, K., Castle, R., Wanninkhof, R., Luger, H., Johannessen, T., Olsen, A., Feely, R. A., Cosca, C. E., 2009. Recommendations for autonomous underway pCO2 measuring systems and data-reduction routines. Deep-Sea Res., 56:512–522.

Chapter 7. Atmospheric Observations

K.-h. Jin, L. Peng, and Z. Xie

7.1. Introduction

The Arctic Ocean has dramatically opened during the summer melting seasons of recent decades with the reduction of sea ice due to global warming at a rate that is unprecedented over at least the past thousand years (Kinnard et al., 2011). The reduction of the ice-covered surface changes the energy balance, leading to the warming of the polar lower atmosphere (Serreze et al., 2011) and also influencing the atmospheric profile. All of these facts taken together highlight the need for continuous, on-site observations of atmospheric parameters in the Arctic Ocean. However, as the polar weather is cold and harsh even during the summertime, autonomous platforms measuring atmospheric properties (e.g., air temperature, humidity, pressure, wind, etc.) often suffer from malfunction as a result of freezing. As such, without in-person management performed on a regular basis, maintenance of autonomous platforms remains difficult. Alternatively, ship-based observations of the Arctic atmosphere can provide invaluable records along the cruise track. In 2016 summer, the Korean ice-breaking research vessel (IBRV) *Araon* voyaged along the East Siberian Sea from August 24 to September 10. Various atmospheric properties were observed during the cruise. In this report, we overview the instruments aboard IBRV *Araon* and deliver some results from the observations.

7.2. Materials and Methods

Atmospheric observations on IBRV *Araon* included basic meteorological parameters (e.g., air temperature, humidity, pressure and wind), radiative fluxes (e.g., net shortwave and longwave radiations), greenhouse gases (e.g., carbon dioxide, methane and water vapor). This year, radiosonde platform were carried out twice daily (00 and 12 UTC) to observe atmospheric vertical profile along the cruise track. Among the observations, 00 and 12 UTCs data were transmitted to real-time radiosonde data network of the World Meteorological Organization via the Global Telecommunication System (GTS) with the aid of the Korea Meteorological Administration (KMA). Because all the observations were almost continuous during the cruise, valuable observational data could be acquired along the cruise track. However, it was challenging to maintain the best performance of the instruments due to harsh weather condition in the Arctic Ocean. The overview of atmospheric observations is summarized in Figure 7.1. A wave-scanned cavity ring-down spectroscopy (CRDS) analyzer (Figure 7.2) in the shelter on 02Deck, which was tube-connected with the CRDS intake at the bottom. Thus, the air samples could travel through the tube (3/8 inch) to reach the CRDS analyzer.

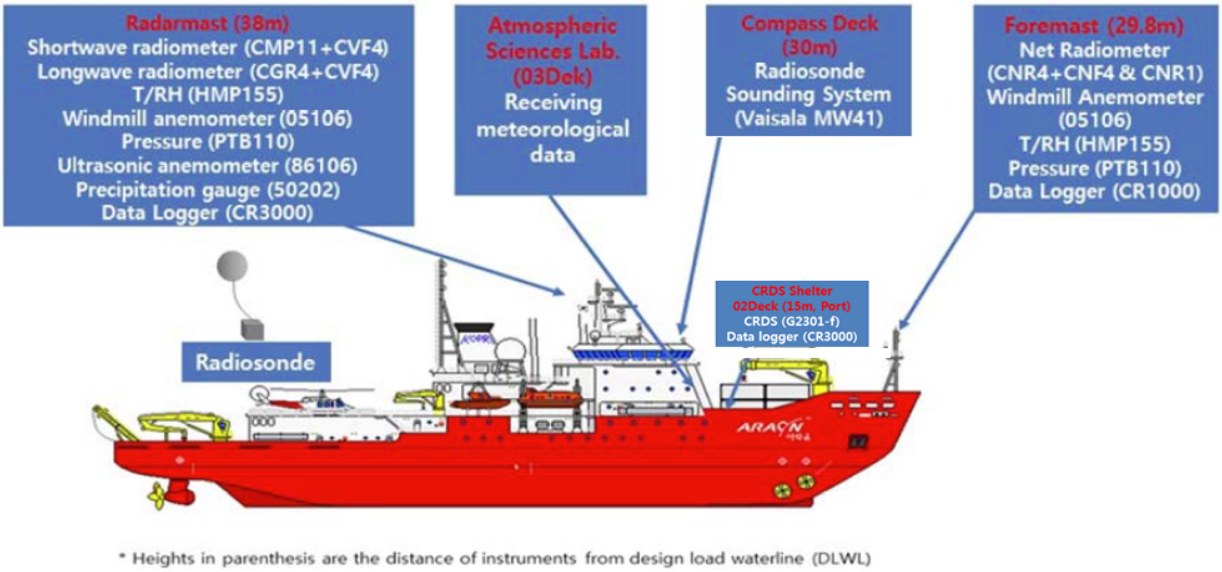

Figure 7.1. Overview of atmospheric observations on IBRV *Araon*.

Figure 7.2. Cavity ring-down spectroscopy (CRDS) analyzer in the 02Deck shelter.

7.3. Observed Results

7.3.1. Surface meteorological variables

Figure 7.3. shows the air temperature and relative humidity measured by HMP155 and the air pressure measured by PTB110 and the wind speed measured by windmill anemometer at the radarmast and solar radiation measured by CNR4 at the foremast. Air temperature during the cruise ranged from -2.8 to 11.2 ℃ with average of 0.8 ℃. Relative humidity was in the range 27 to 99 %. Air pressure ranged from 980 to 1031 hPa with average 1018 hPa. Downwelling shortwave radiations shows an apparent diurnal cycle associated with the diurnal variation of solar zenith angle. The sunny day peak value reached almost 532 W/m2 on 00 UTC August 25. The daytime peak values were generally low because the weather was mostly cloudy during period of the cruise. Maximum wind speed of 25 m/s was recorded on August 28. But overall wind speed was 7.8 m/s with standard deviation of 4.5 m/s. Noting that wind speed shown here is apparent, not true, true wind speed will be calculated considering ship's course and speed after the cruise.

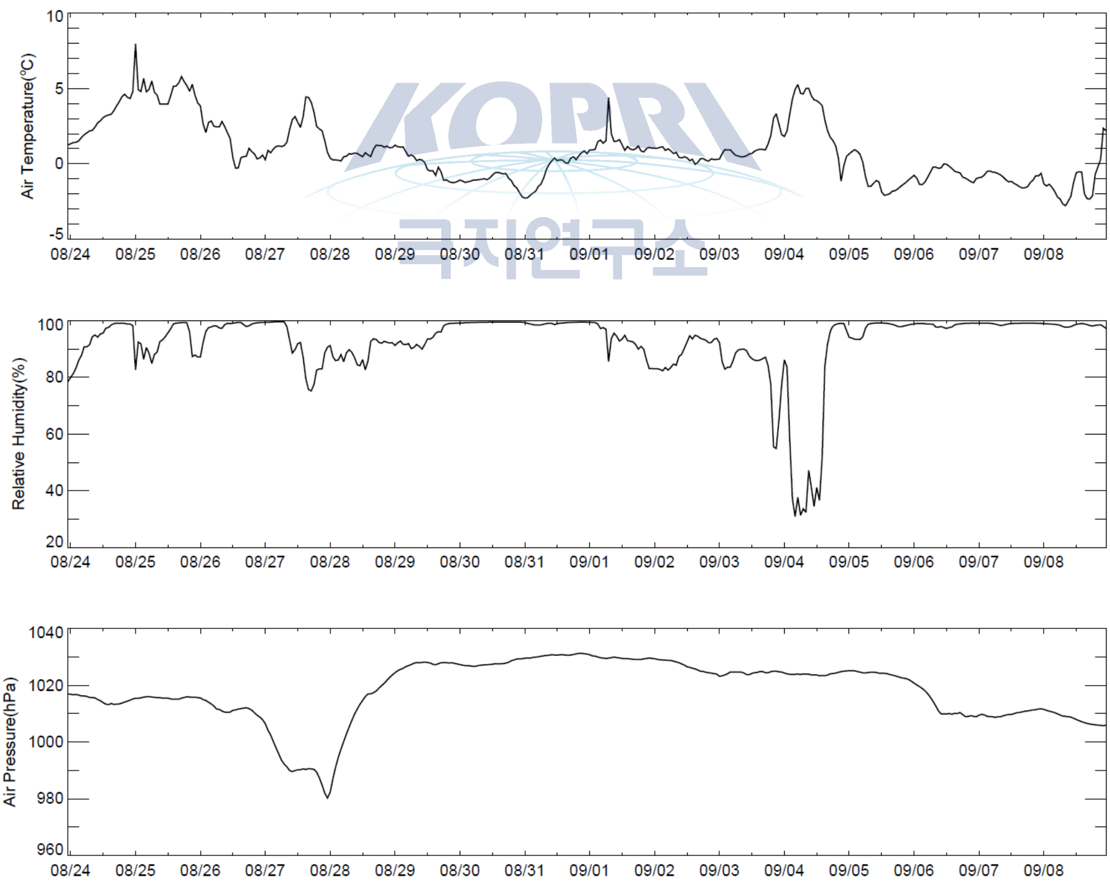

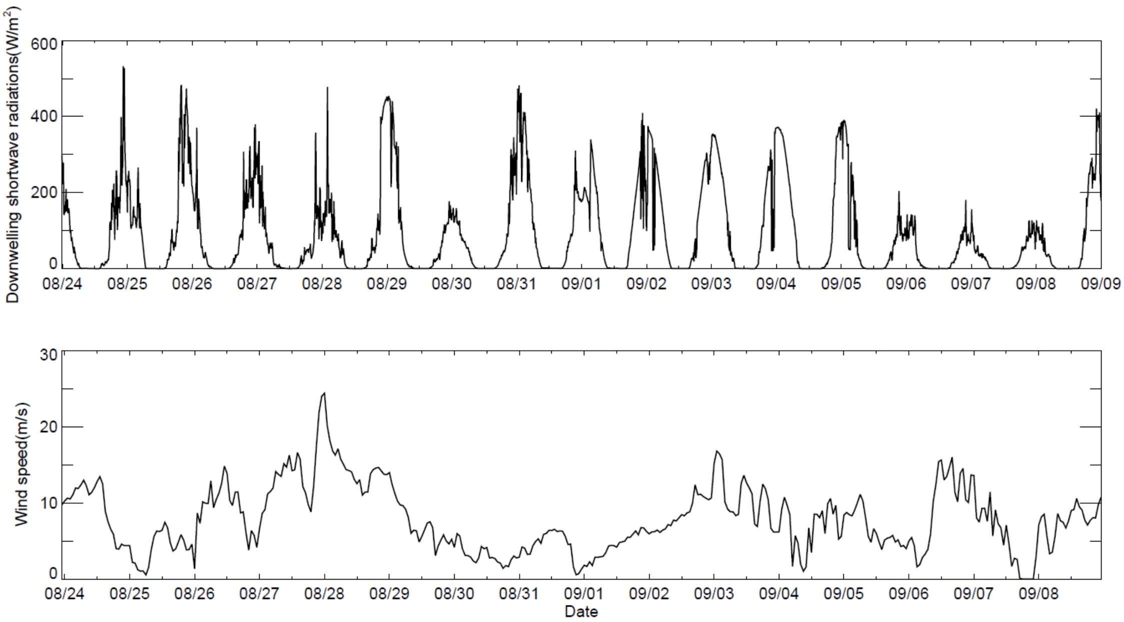

Figure 7.3. Meteorological variables during cruise.

7.3.2. Carbon dioxide, methane, and water vapor

During the ARA07C cruise, the CRDS was operated in high precision mode (CO_2-CH_4-H_2O) in the CRDS shelter (Figure 7.4). Average CO_2 concentration during the cruise was 394.8 ppm. CH_4 concentration measured by CRDS ranged from 1.90 ppm to 2.19 ppm and an average during cruise is 1.95 ppm. H_2O ranged from 4.7 mmol/mol to 12.3 mmol/mol with an average of 6.5 mmol/mol, respectively (Figure 7.5).

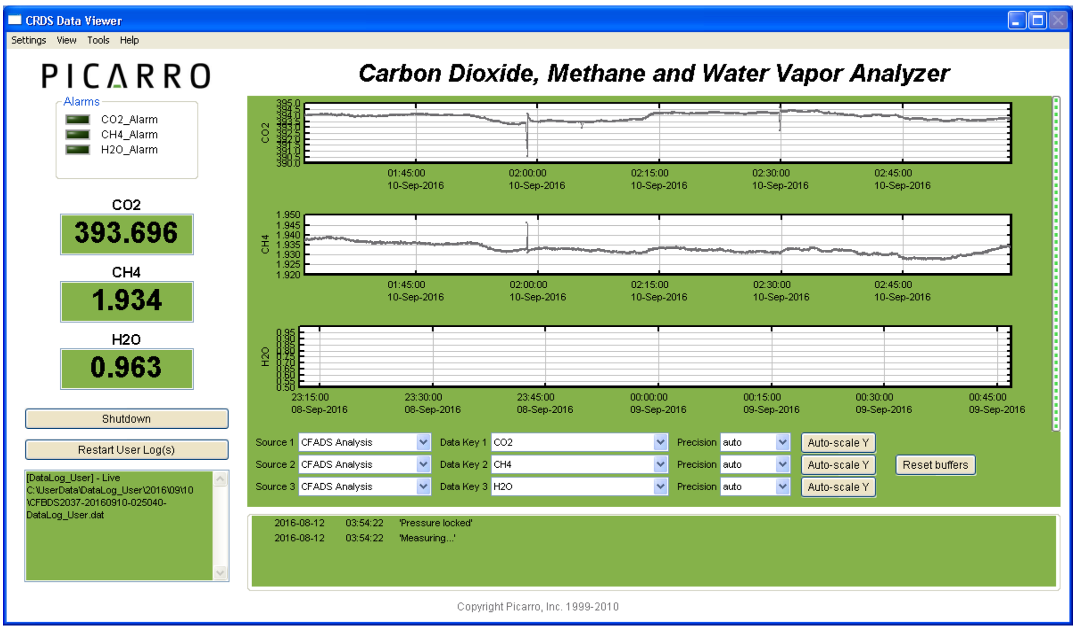

Figure 7.4. Real time variation of CO_2, CH_4 and H_2O mode.

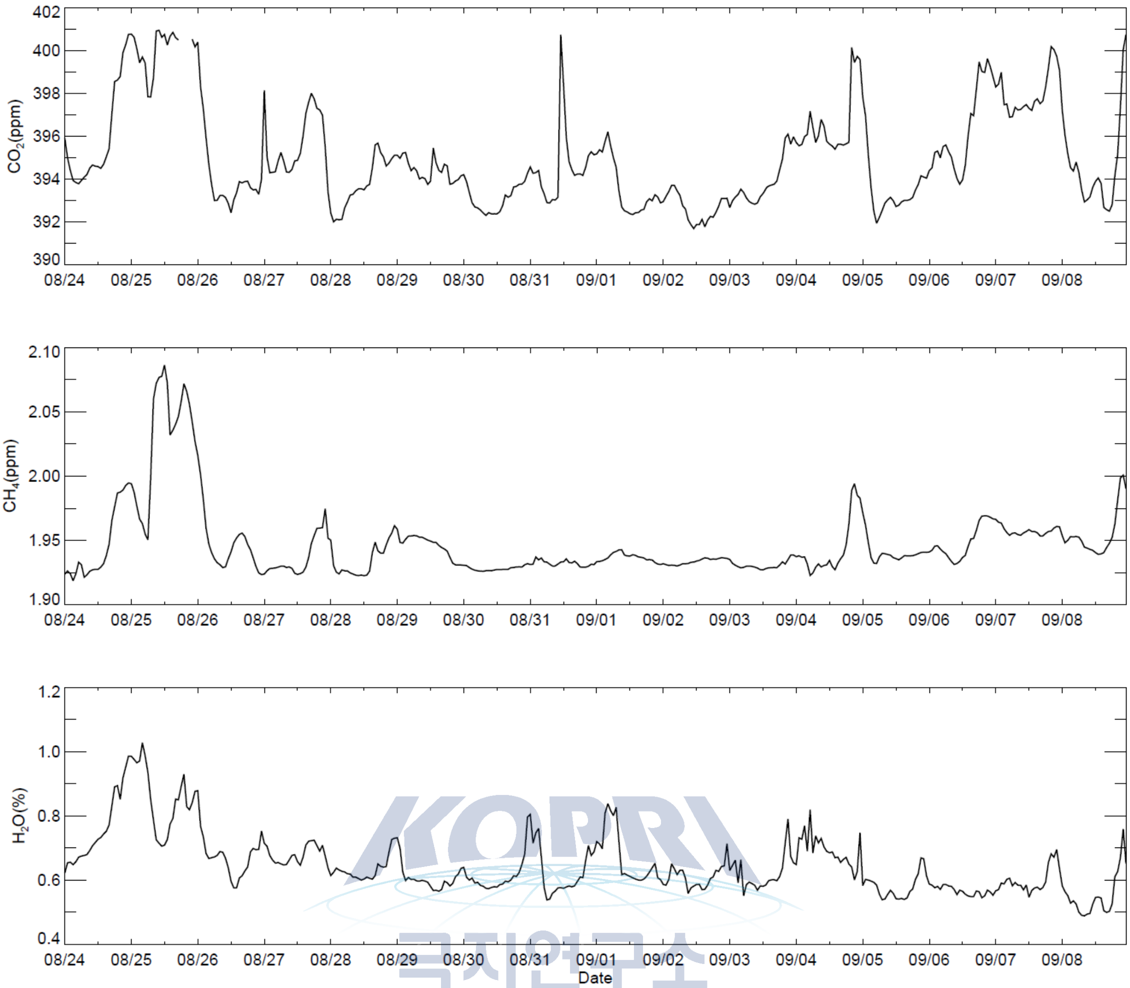

Figure 7.5. CO_2, CH_4, H_2O concentration variation during the cruise.

7.3.3. Radiosonde profiles

During the 2016 Arctic cruise, the radiosonde ballon was regularly launched to measure the atmospheric profile of temperature, humidity, and wind. These data are crucial for understanding the thermodynamic properties in the Arctic summer atmosphere and also precious because they cover sparsely observed region. Basically the radiosonde observations were carried out at 00 and 12 UTC for all periods, but 03, 06, 09, 15, 18, 21 UTCs were added for intensive observing periods. The log of radiosonde observations is summarized in Table 7.1. For ARA07C, a total of 49 launches were attempted, among which 19 launches did not reach the 100 hPa level and two were completely failed due to the break of unwinder under the very windy environment. The average time taken from the launch to the end of sound is ~4000 s (1hr 10min) and the average ascending height is ~20 km above sea level. Fig 7.6 shows two radiosonde sounding result on different days.

Table 7.1. Log of radiosonde observations during ARA07C.

No.	Date	Time (UTC)	Start time	Duration (seconds)	Height (km)	Pressure (hPa)	Remarks
1	2016-08-26	12	10:56	2723	13.5	156.0	
			12:06	3022	16.4	100.1	Failed.
2	2016-08-27	00	22:58	3129	17.1	91.3	
3	2016-08-27	12	10:56	1676	9.3	297.2	Failed.
			11:48	1284	6.9	412.0	Failed.
4	2016-08-28	00					Failed. Unwinder was broken after launching.
5	2016-08-28	12	10:59	1699	9.0	298.4	Failed.
			12:14	2191	10.9	225.4	Failed.
6	2016-08-29	00	23:01	5705	31.4	10.2	
7	2016-08-29	12	10:55	5174	26.7	20.5	
8	2016-08-30	00	22:57	3686	20.1	56.8	
9	2016-08-30	12	11:00	4107	20.2	51.6	
10	2016-08-31	00	23:00	2089	11.5	213.1	Failed.
			00:04	2096	10.6	244.1	Failed.
11	2016-08-31	12	11:00	3541	19.0	67.1	
12	2016-09-01	00	22:57	6513	34.9	6.0	
13	2016-09-01	06	04:59	4693	23.3	34.3	
14	2016-09-01	12	11:00	5583	29.2	14.0	
15	2016-09-01	18	17:00	4231	20.9	49.6	
16	2016-09-02	00	23:00	2993	13.9	147.0	
			00:18	3790	20.6	52.4	
17	2016-09-02	06	05:03	5879	24.8	27.2	
18	2016-09-02	12	11:00	3765	19.7	60.2	
19	2016-09-02	18	17:00	3485	15.3	117.0	
20	2016-09-03	00	23:00	1858	9.6	285.4	Failed.
			00:05	1528	8.1	358.6	Failed.
21	2016-09-03	06	05:00	5337	26.8	19.9	
22	2016-09-03	12	11:00	4656	25.1	26.0	
23	2016-09-03	18	17:00	6082	32.7	8.0	
24	2016-09-04	00	22:59	6705	34.5	6.1	
25	2016-09-04	03	02:01	3475	17.2	87.8	
26	2016-09-04	06	05:00	5999	29.2	13.7	
27	2016-09-04	09	08:00	6783	33.4	7.3	
28	2016-09-04	12	11:00	6524	34.7	6.1	
29	2016-09-04	15	14:01	4251	22.0	41.7	
30	2016-09-04	18	17:00	6372	35.0	5.7	
31	2016-09-04	21	20:00	4274	20.0	56.6	
32	2016-09-05	00	23:00	3400	15.3	116.0	Failed.
33	2016-09-05	03	02:00	2632	12.3	184.2	Failed.
34	2016-09-05	06	05:00	4108	19.1	64.4	
35	2016-09-05	09	07:59	2385	11.9	193.8	Failed.
36	2016-09-05	12	11:00	5687	28.1	16.0	
37	2016-09-05	15	14:01	1620	8.1	349.3	Failed.
38	2016-09-05	18	17:00	4022	18.3	72.0	
39	2016-09-05	21	20:00	3618	16.7	92.4	
40	2016-09-06	00	22:50	3060	14.2	134.8	Failed.
41	2016-09-06	06	05:03	3000	13.1	158.2	Failed.
42	2016-09-06	12	11:00	2844	14.1	135.4	Failed.
43	2016-09-06	18	17:00	3229	15.4	110.2	Failed.
44	2016-09-07	00	22:59	3206	15.8	103.6	Failed.
45	2016-09-07	06					Failed. Unwinder was broken after launching.
46	2016-09-07	12	11:00	3834	19.1	62.4	
47	2016-09-08	00	23:00	3567	19.1	63.4	
48	2016-09-08	12	11:00	6850	36.5	4.5	
49	2016-09-09	00	23:01	2440	12.3	177.7	Failed.

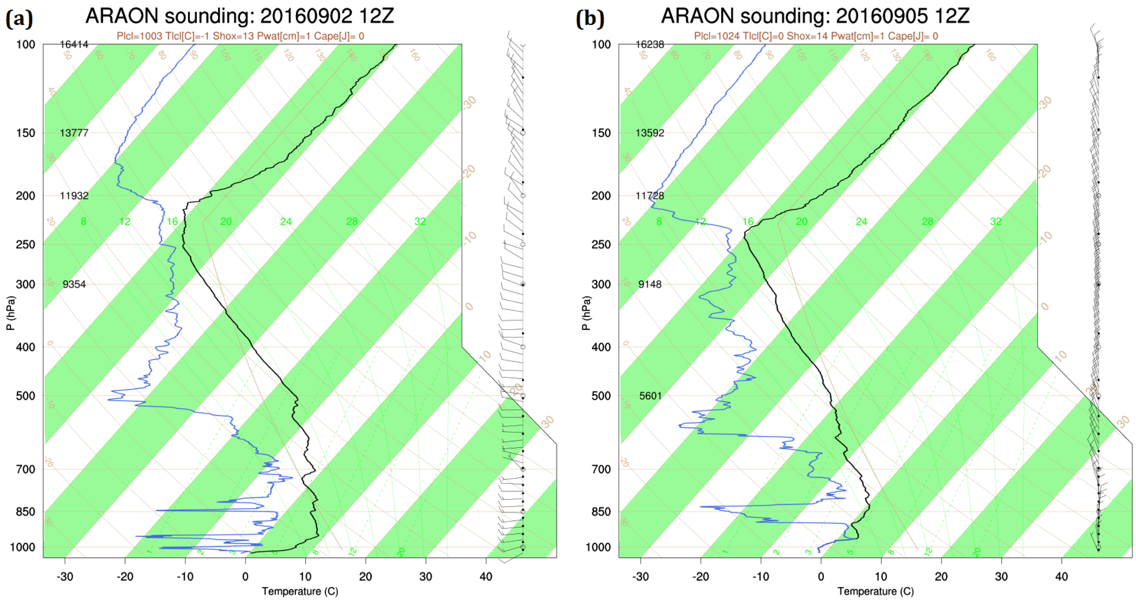

Figure 7.6. The skew T-log p diagrams for two radiosonde observations.

7.4. Summary

Various atmospheric properties were observed during ARA07C cruise of IBRV Araon. Atmospheric environmental variables were observed by multiple instruments aboard Araon including air temperature, air pressure, wind speed and direction, humidity, water vapor, carbon dioxide and methane, radiation and radiosonde profile.

Although lots of data are needed strict QC, this report showed basic time series of most data measured during the cruise after simple QC by removing the apparently unphysical values.

Chapter 8. On-Board Test of the Arctic Safe Voyage Planning System under Development in KRISO

K.J. Kang, S.K. Yeo, and S.W. Choi

8.1. Introduction

The purpose of this project was to develop the Arctic safe voyage planning system including the following sub topics:

- ✓ Development of the sea ice prediction system with accurate and high-resolution in Arctic sea.
- ✓ Development of the transit model including the prediction and evaluation of safe speed and DB construction
- ✓ Development of the voyage planning technology in NSR for the safe navigation
- ✓ Construction of co-work system between arctic nations and international technology standardization through the establishment of safe navigation guideline and leading action

There are several expected results from this research project. The final result of this research project will be commercialized as the safe voyage planning system for vessels operating in NSR. Also, the guidelines of the ship building and safe navigation for vessels operating in NSR will be one of the achievements from this research project. These expected results will contribute to the promotion of navigation in NSR.

For the confirmation of validation and improvement of the system under developing process, an on-board test was carried out on the 2nd Araon voyage test from 23rd August to 10th September 2016.

8.2. System Description

The safe voyage path planning system consists of a client program installed on the vessel and main control server on KRISO, which includes the optimum path planning module made by KAIST team, the Arctic sea environment data from KIOST, Araon's performance data base, and system integrated by KRISO and Dong-gang mtech as shown in Figure 8.1 and 8.2.

The standard procedure of the system is as following:

1. To send Start, destination point and way-point from operating vessel to KRISO server.
2. KRISO server queries the defined Arctic sea environment data from KIOST for finding the optimal path.
3. The optimum path planning module in KRISO server finds out the optimal path based on the Arctic environment data and ship's performance data etc.
4. KRISO server sends the optimal path and the Arctic sea environment data to the operating vessel.

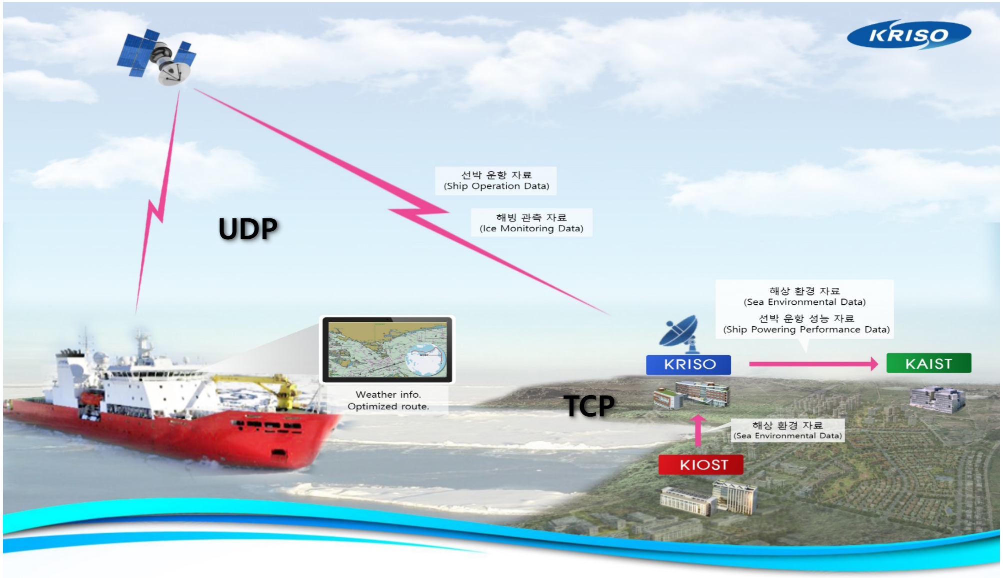

Figure 8.1. The safe voyage path planning system.

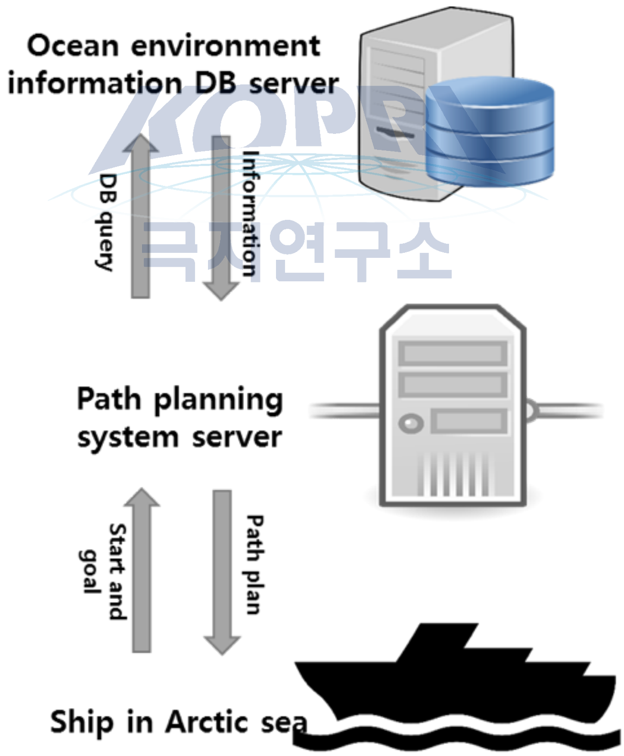

Figure 8.2. The standard procedure.

8.3. The Activity on Voyage of 2016 2nd Arctic Sea Explore on Araon

The main purpose of our team boarding on the Araon was to set up and test the safe voyage planning system. Also, to get the feedback from navigation officer and chief engineer by interview was the one of our team's goals.

8.3.1. To set up the system

In order to set up the system, our team brought the 1 client PC and 1 monitor to test the system. In our primary strategy, we wanted to use Inmarsat as a data transmission method. However, there was the problem of cost of transmission to keep connection between sending the initial data from client and receiving the result data from KRISO server. So we modified the client program to data transmission as file transmission without using continuous connection between the client program and the KRISO server. In the present program, the user inputs the start, destination and waypoint, the program creates the input file and sends it to KRISO server. After several minutes, the user can check the state of KRISO server by FTP server. If there is a result file in KRISO FTP server, the user can download the result file and load the result file onto the safe voyage planning client program.

8.3.2. To test the system

In order to test the safe voyage planning system, we used the real voyage plan. The 1st and 3rd test uses the voyage plan from Barrow to 1st research way point. The result of 1st test was inappropriate as shown in Figure 8.3.

In this figure, the path-planning algorithm cannot pass through the pack ice region. In this situation, KAIST path planning module could not consider the pack ice and level ice, so if ice thickness is thicker than ice breaking capability, the path planning module decide that the vessel cannot go through that region even though the region is pack ice region, not the level ice region. So we modified the path-planning algorithm to make our algorithm more similar to the real path planning by considering sea ice concentration to figure out which region is pack ice or level ice region.

In 2nd test, we used the path from last research point to Nome and the modified the path-planning algorithm. The result from 2nd test is acceptable as Figure 8.4.

3rd test also had an appropriate result in compare with 1st test result as Figure 8.5.

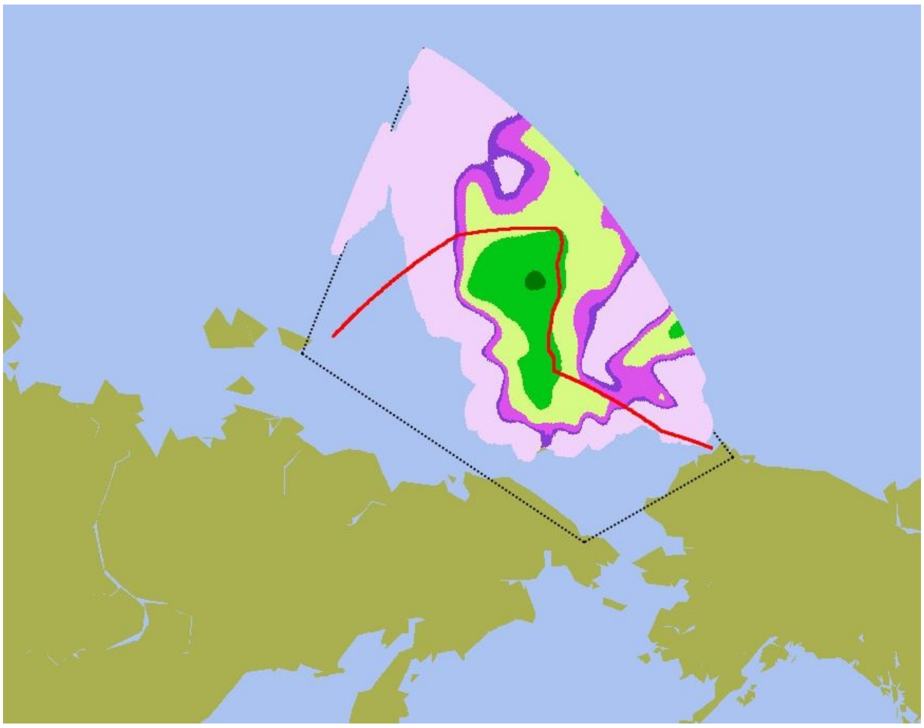

Figure 8.3. The 1st test result: path from barrow to 1st research point.

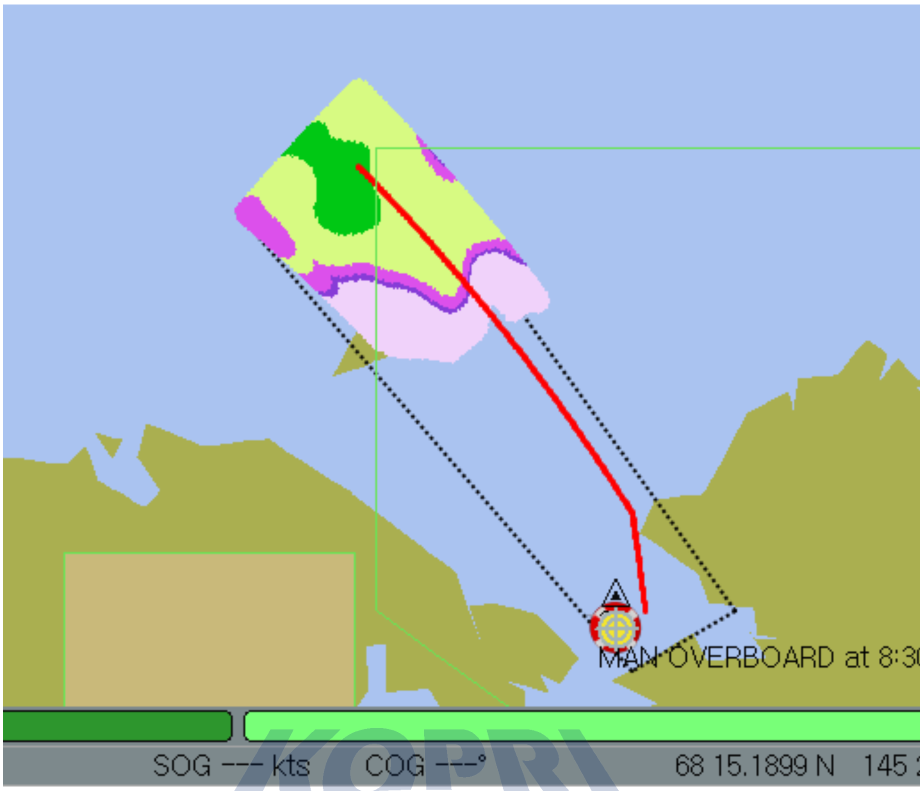

Figure 8.4. 2nd test result: path from last research point to Nome

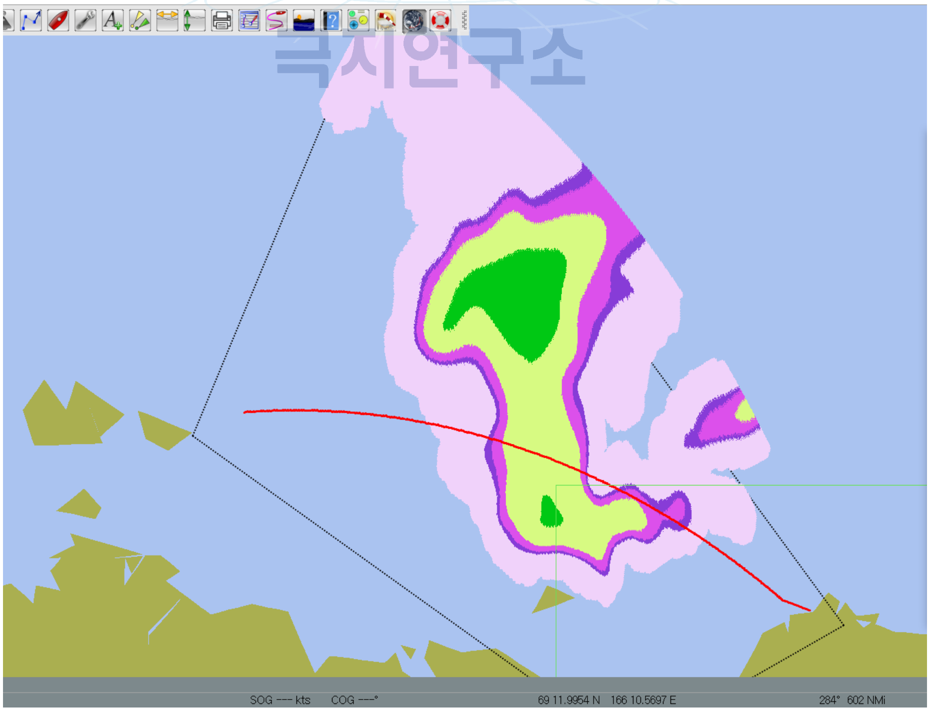

Figure 8.5. 3rd test result: path from Barrow to 1st research point

8.3.3. The interview with Araon crew

In order to get feedback of our system, we had a meeting with Araon crew twice. The 1st meeting with navigation officers was on 5th, September, 2016. The 1st, 2nd, 3rd navigation officer attended the meeting. As a summary of 1st meeting, since the polar code shall enter into force from 1st January 2017, the vessel navigating the Arctic sea should be prepare the voyage planning. In this vein, the Arctic safe voyage planning system will be helpful for the vessel which operating in the Arctic sea. As there is much interest in the reliability of Arctic sea environment data and path, it is important that the Arctic safe voyage planning system provide the user with various types of accurate information to utilize it as effectively as possible.

The 2nd meeting was on 7th, September, 2016. This meeting was for knowing detailed information on the Araon's propulsion system. The main generator load-test table shows the fuel consumption according to the engine load, where the maximum efficiency can be obtained around 80% load. For continuous ice breaking situations, the real ship speed and power data have not been collected since general voyages in polar regions are usually done in the summer.

8.4. Conclusion

During the voyage of Araon, our team gets the comparable results, especially by feedback from Araon crew. Through the feedback, we could find the way how to improve the Arctic safe voyage planning system. In order to achieve this improvement, the sustainable effort should be required in modification of the system to be more accurate and more similar to the real system.

Appendix 1. Participants

No	Organization	Name	Contact	Works in the expedition
1	KOPRI	Young Keun JIN	ykjin@kopri.re.kr	Chief scientist
2	KOPRI	Moon Young CHOE	mychoi@kopri.re.kr	Geophysics
3	KOPRI	Seung Goo KANG	ksg9322@kopri.re.kr	Multi-channel seismic
4	KOPRI	Young Gyun KIM	ygkim@kopri.re.kr	Heat flow
5	KOPRI	Dong Seob SHIN	dsshin@kopri.re.kr	Technical & support
6	KOPRI	Yung Mi LEE	ymlee@kopri.re.kr	Micro-biology
7	KOPRI	Min Kyu LEE	kyu0807@kopri.re.kr	Multi-channel seismic
8	KOPRI	Hyoung Jun KIM	Jun7100@kopri.re.kr	Multi-beam & SBP
9	KOPRI	Yeonjin CHOI	yjchoi@kopri.re.kr	Multi-channel seismic
10	KOPRI	Inhyuk SEO	disgur6091@kopri.re.kr	Multi-channel seismic
11	KOPRI	Imgyo LEE	Imgyo.lee@kopri.re.kr	Multi-beam & SBP
12	KOPRI	Heungsoo MOON	jepy@kopri.re.kr	Sediment core
13	KOPRI	Young Shin KWON	kwonys@kopri.re.kr	Ocean chemistry
14	KOPRI	Nakwon HEO	haizen@kopri.re.kr	CTD
15	KOPRI	Young-Suk CHOI	yschoi@kopri.re.kr	CTD
16	KOPRI	Kwang Ho JIN	khjin@kopri.re.kr	Atmosphere
17	KIOST	Chan Min YOO	cmyoo@kiost.ac.kr	Geophysics
18	IORAS	Boris Baranov	bbaranov@ocean.ru	Geophysics
19	Nanjing Univ.	Zelin Xie	zelin_xie@163.com	Atmosphere
20	Alaska Fairbanks Univ.	Liran Peng	lpeng2@alaska.edu	Atmosphere
21	Hanyang Univ.	Dong Hun LEE	thomaslee0118@gmail.com	Marine organic geochemistry
22	Gyeonsang Univ.	Buyeong LEE	a901009@naver.com	Mineralogyrkd
23	KIGAM	Moo Hee KANG	karl@kigam.re.kr	Sparker survey
24	KIGAM	Ji Hoon KIM	save@kigam.re.kr	Geochemistry
25	KIGAM	Joung Gyu CHOI	jgchoi@kigam.re.kr	Sparker survey

26	KIGAM	Sujin CHAE	sujin@marineaid.co.kr	Sparker survey
27	KRISO	Kuk Jin KANG	kjkang@kriso.re.kr	
28	KAIST	Seung Kyun YEO	adonisysk@kaist.ac.kr	
29	DongKand M-Tech	Sungwoo CHOI	choisw@dkmtech.com	
30	Arts Council Korea	Nam Joong KIM	lpolarbear@hanmail.net	Writer
31	FESCO	Mikhail STRIZHNEV		Ice pilot
32	FESCO	Leonid TUYNO	lttuyno@outlook.com	Ice pilot
33	-	Jong Ik KIM		Ship’s doctor

Appendix 2. List of Stations and Line Survey

Station / Waypoint	STN No.	Work order	*Gear	Date (UTC)	TIME (UTC) Start		Bottom touch		End		Latitude	Longitude	Depth (m)	Gyro	Remark
					hh	mm	hh	mm	hh	mm					
SBPWP01				2016-08-27	20	27					75.3670	174.2089	202	237	Mn Survey Start
SBPWP02			MB/SBP	2016-08-27	21	10					75.3563	173.7641	200	270	Mn Site
SBPWP03				2016-08-27					21	47	75.3483	173.3730	184	235	Mn Survey End
			MB/SBP	2016-08-27	23	0									Multibeam Line Survey Start
				2016-08-28					2	17					Multibeam Line Survey End
SPSWP00				2016-08-28	9	12					75.4217	171.9024	165	195	Spaker Ready
SPSWP01				2016-08-28	10	44			18	36	75.3487	171.7707	161	208	SPS Line.1 Start
SPSWP02				2016-08-28	18	47			7	29	74.8189	170.814	61	196	SPSLine.1 End, SPS Line.2 Start
SPSWP03			SPS	2016-08-29	7	46					74.6920	172.1189	171	24	SPS Line.2 End, SPS Line.3 Start
SPSWP04				2016-08-29					15	50	75.1948	173.1213	200		SPS Line.3 End, SPS Line.4 Start Sparker End
ARA07C01CTD1		1	CTD	2016-08-29	17	6	16	59	17	41	75.3563	173.7641	195	306	CTD
ARA07C01BXC2		2	BC	2016-08-29	17	54	18	3	18	13					
ARA07C01BTRs3					18	48	18	56			75.3589	173.7620	198	168	Beamtroll Start
ARA07C01BTR3	ST. 01	3	Beam Trawl	2016-08-29	19	24					75.3523	173.7672	194	168	
ARA07C01BTRe3					19	41			19	58	75.3479	173.7707	167	197	Beamtroll End
ARA07C01DRDs4		4	Dredge	2016-08-29	22	49	23	13			75.3586	173.7687	190	207	Dredge Start
ARA07C01DRDe4									23	57	75.3525	173.7567	187	207	Dredge End
MCSWP01				2016-08-30	8	32					75.0177	172.452	133.5	223	MCS Ready
MCSWP02				2016-08-30	13	9					74.7949	171.6135	63	248	MCS Line 01 Start
MCSWP03			MCS	2016-08-31	9	2					74.0810	166.3038	48	123	MCS Line 02 Start
MCSWP04				2016-08-31	20	27					73.5416	168.8365	107	4.6	MCS Line 03 Start
MCSWP05				2016-09-02					14	14	76.7522	173.8677	530	24	MCS Line 03 End

ARA07C02aCTD1	ST. 02a	1	CTD	2016-09-02	17	44	18	3	18	33	76.7476	174.2610	648	243	
ARA07C02aBXC2		2	BC	2016-09-02	18	54	19	20	19	40					
ARA07C02aGVC3		3	GC	2016-09-02	20	50	21	8	21	29					
ARA07C02bGVC1 ARA07C02bHFG1	ST. 02b	1	GC/HF	2016-09-02	22	56	23	12	23	55	76.7463	174.3203			
ARA07C03CTD1	ST. 03	1	CTD	2016-09-03	4	22			4	53	76.1074	172.6548	308	245	
ARA07C03BXC2		2	BC	2016-09-03	5	0	5	22	5	33					
ARA07C03GVC3 ARA07C03HFG3		3	GC/HF	2016-09-03	5	48	6	16	7	1					
ARA07C03GVC4 ARA07C03HFG4		4	GC/HF	2016-09-03	8	47	8	57	9	33					
ARA07C04CTD1	ST. 04	1	CTD	2016-09-03	16	7	16	17	16		75.4231	171.4932	162	252	
ARA07C04BXC2		2	BC	2016-09-03	16	42	16	48	16	55					
ARA07C05CTD1	ST. 05	1	CTD	2016-09-03	22	23			22	38	74.7589	170.4555	60	0.9	
ARA07C05BXC2		2	BC	2016-09-03	22	52	22	58	23	3					
ARA07C05GVC3 ARA07C05HFG3		3	GC/HF	2016-09-03~4	23	50	0	6	0	42					
ARA07C05CTD4		4	CTD	2016-09-04	0	54			1	6					
ARA07C06CTD1	ST. 06	1	CTD	2016-09-04	5	22			5	33	74.0192	169.4482	45	246	
ARA07C06BXC1		2	BC	2016-09-04	5	45	5	52	5	56					
ARA07C07CTD1	ST. 07	1	CTD	2016-09-04	8	27			8	39	73.8145	169.1941	44	178	gas flare
ARA07C07BXC2		2	BC	2016-09-04	8	50	8	54	9	1					
ARA07C07GVC3 ARA07C07HFG3		3	GC	2016-09-04	10	4	10	10	10	31					
ARA07C08CTD1	ST. 08	1	CTD	2016-09-04	12	21			12	31	73.5790	168.8832	40	215	
ARA07C09CTD1	ST. 09	1	CTD	2016-09-04	14	58			15	8	73.8286	167.6120	44	285	
ARA07C10CTD1	ST. 10	1	CTD	2016-09-04	17	40	17	43	17	49	74.0763	166.2480	45	282	
ARA07C11CTD1	ST. 11	1	CTD	2016-09-04	20	9			20	18	74.2717	167.6445	48	50	
ARA07C12CTD1	ST. 12	1	CTD	2016-09-04	22	35			22	50	74.4601	168.9974	54	48	
			MB/SBP	2016-09-06	9	21					76.3609	-165.5360	831	17	MBS Line 01A Start
				2016-09-06					10	16	76.4790	-165.4193	781	207	MBS Line 01A End
				2016-09-06	17	13					75.6214	-169.9269	835	96	MBS Line 01B Start
				2016-09-06					19	14	75.7879	-169.1859	304	262	MBS Line 01B End
				2016-09-06	19	14					75.7873	-169.1905	304	237	MBS Line 02 Start
				2016-09-06					20	51	75.6309	-170.0026	951	246	MBS Line 02 End
				2016-09-06	21	2					75.6473	-170.0693	1053	33	MBS Line 03 Start
				2016-09-06					22	43	75.8041	-169.1893	311	7.5	MBS Line 03 End
				2016-09-06	22	47					75.8043	-169.2185	314	261	MBS Line 04 Start
				2016-09-07	0	18					75.6995	-170.0328	1006	17	MBS Line 05 Start
				2016-09-07					1	16	75.8100	-170.2926	1141	15	MBS Line 05 End

				2016-09-07	1	22					75.8164	-170.2509	1045	164	MBS Line 06 Start
				2016-09-07					2	30	75.7065	-169.9375	865	126	MBS Line 06 End
				2016-09-07	2	42					75.7217	-169.8620	769	405	MBS Line 07 Start
				2016-09-07					3	35	75.8471	-170.1007	700	350	MBS Line 07 End
				2016-09-07	3	45					75.8424	-170.0083	646	124	MBS Line 08 Start
				2016-09-07					4	26	75.7454	-169.7595	615	143	MBS Line 08 End
				2016-09-07	4	35					75.7565	-169.6891	482	344	MBS Line 09 Start
				2016-09-07					5	17	75.8581	-169.9322	599	5.59	MBS Line 09 End
				2016-09-07	5	23					75.8597	-169.8960	583	159	MBS Line 10 Start
				2016-09-07					6	6	75.7531	-169.6165	413	118	MBS Line 10 End
				2016-09-07	6	12					75.7625	-169.5790	378	336	MBS Line 11 Start
				2016-09-07					6	57	75.8656	-169.8514	561	344	MBS Line 11 End
				2016-09-07	7	3					75.8691	-169.8058	528	156	MBS Line 12 Start
				2016-09-07					7	46	75.7693	-169.5322	351	144	MBS Line 12 End
				2016-09-07	7	52					75.7751	-169.4947	341	334	MBS Line 13 Start
				2016-09-07					8	36	75.8759	-169.7463	473	29	MBS Line 13 End
				2016-09-07	8	41					75.8800	-169.7105	455	103	MBS Line 14 Start
				2016-09-07					9	27	75.7740	-169.4372	321	137	MBS Line 14 End
				2016-09-07	9	34					75.7740	-169.4372	321	137	MBS Line 15 Start
				2016-09-07					10	21	75.8831	-169.6509	432	338	MBS Line 15 End
				2016-09-07	10	27					75.8878	-169.6017	425	145	MBS Line 16 Start
				2016-09-07					11	17	75.7933	-169.3698	316	81	MBS Line 16 End
				2016-09-07	11	23					75.8015	-169.3422	314	329	MBS Line 17 Start
				2016-09-07	11	39					75.8426	-169.4347	359	70	MBS Line 18 Start
ARA07C13BXC 1	ST. 13	1	BC	2016-09-07	18	43	18	49	19	3	75.6794	-169.7360	609	165	
ARA07C13GVC 2 ARA07C13HFG 2		2	GC/HF	2016-09-07	19	32	19	48	20	28	75.6795	-169.7379	610		Gas Hydrae
ARA07C14GVC 1 ARA07C14HFG 1	ST. 14	1	GC/HF	2016-09-07	21	58	22	21	23	8	75.7034	-169.7592			
ARA07C15MR Nr1	ST. 15 MS01	1	Mooring	2016-09-08	3	36					75.2444	-171.9809	504	41	
			MB	2016-09-08	5	49					75.2475	-172.0015	498	254	MS Survey

Appendix 3. Sea Ice Map

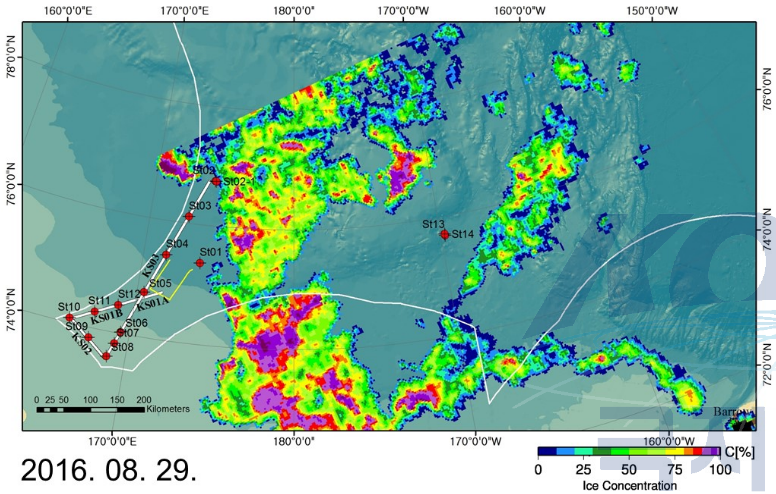

2016. 08. 29.

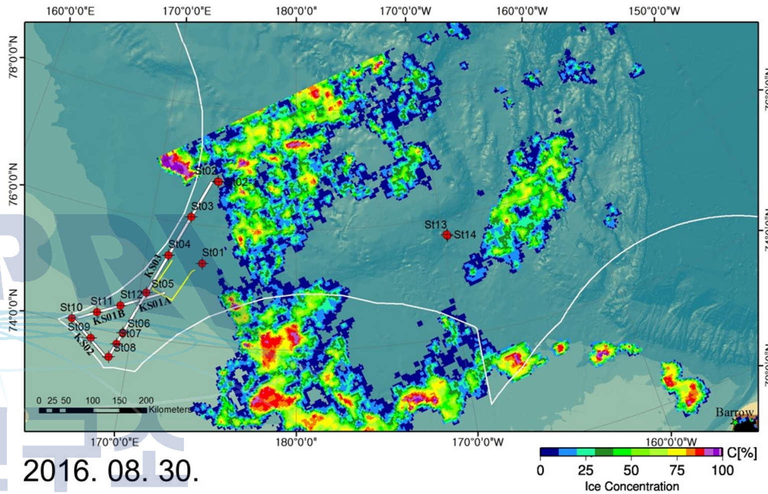

2016. 08. 30.

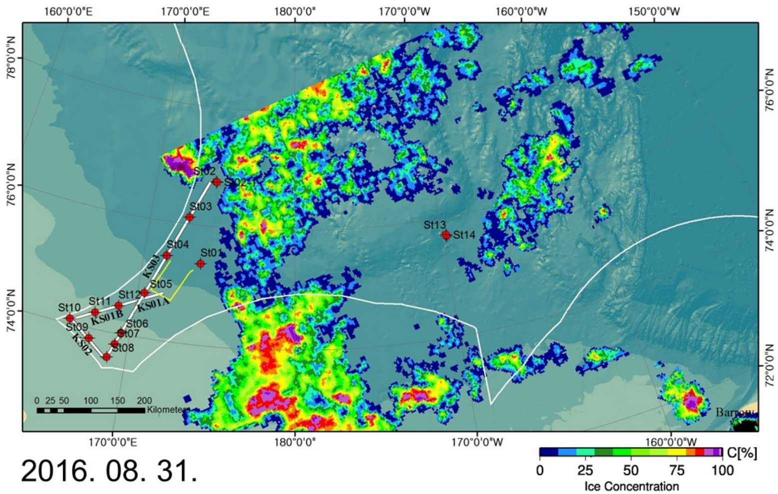

2016. 08. 31.

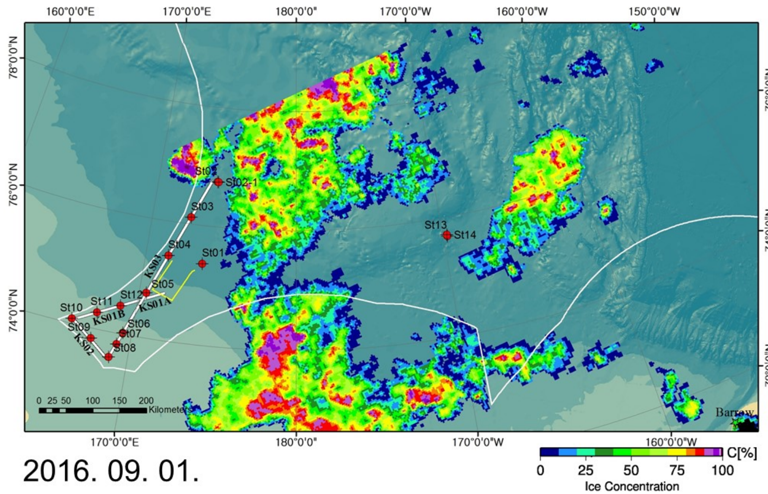

2016. 09. 01.

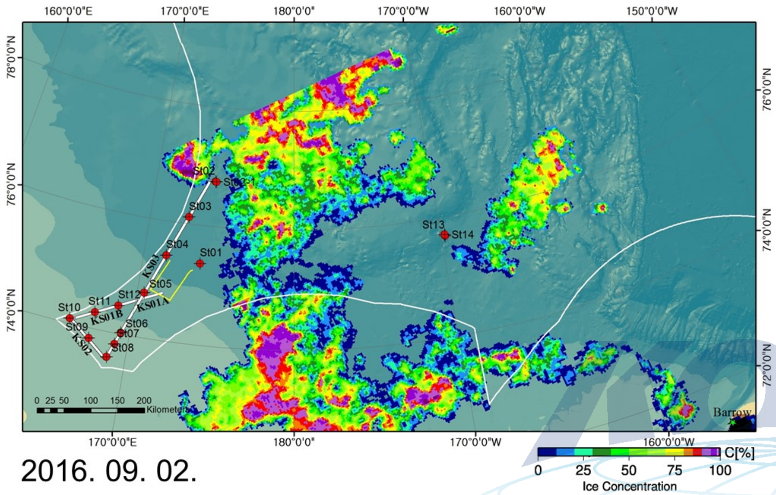

2016. 09. 02.

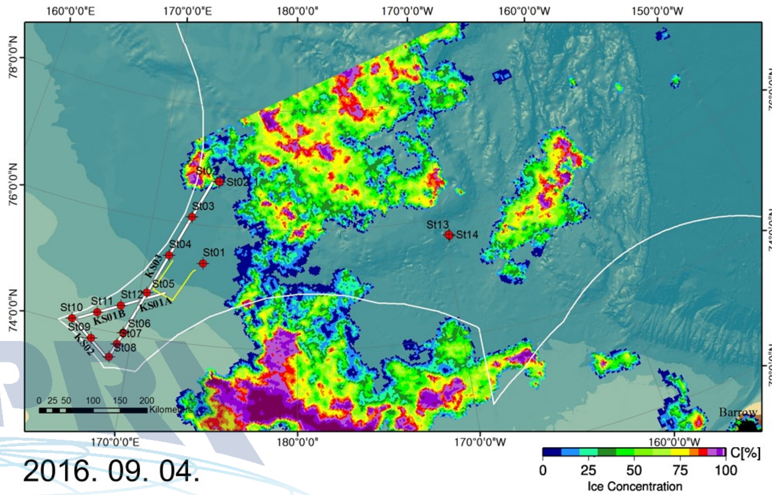

2016. 09. 04.

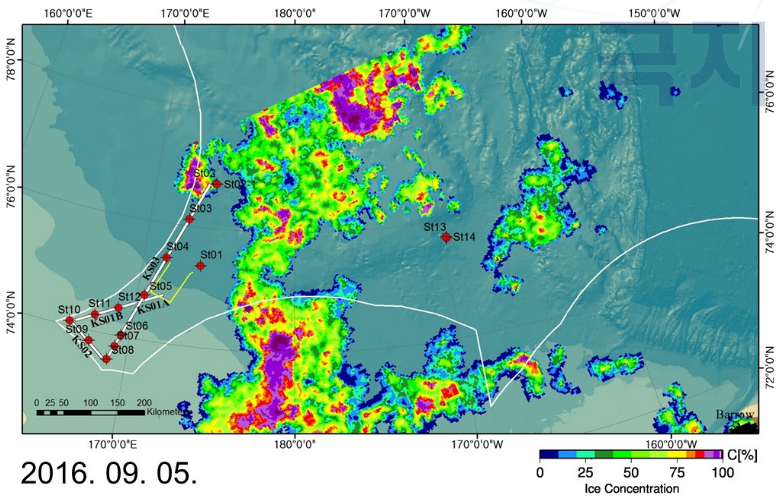

2016. 09. 05.

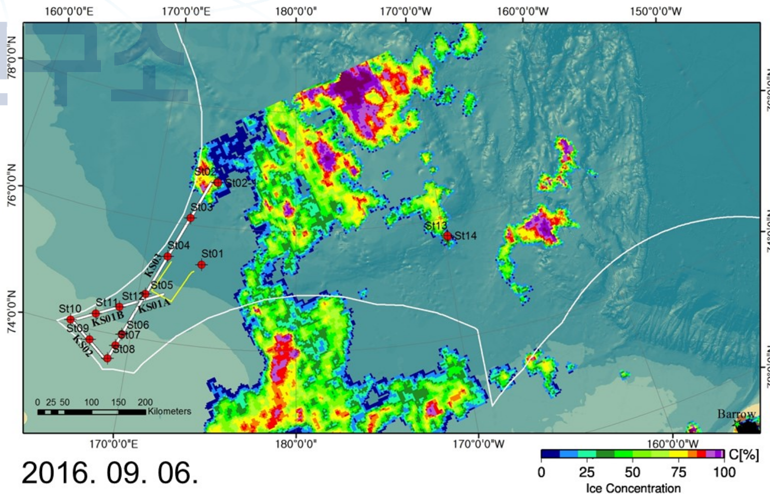

2016. 09. 06.

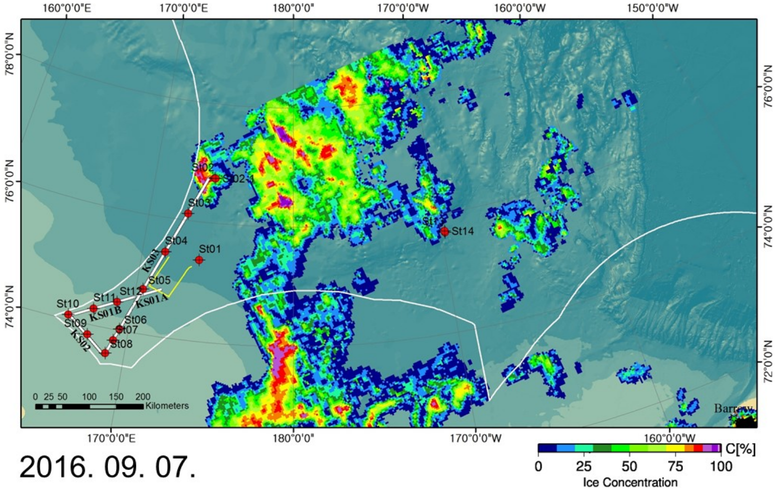

2016. 09. 07.

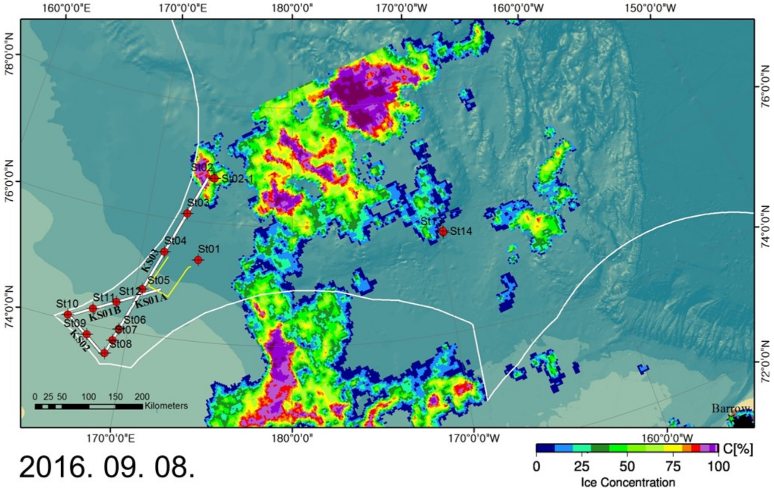

2016. 09. 08.

Appendix 4. Group Photo